Dissertations, Master's Theses and Master's Reports

2018

COLD START ANALYSIS AND MODELING OF A DIRECT-INJECTION GASOLINE ENGINE

Yash Borghate

Michigan Technological University, yvborgha@mtu.edu

www.manaraa.com

COLD START ANALYSIS AND MODELING OF A DIRECT-INJECTION
GASOLINE ENGINE

By

Yash Borghate

A THESIS

Submitted in partial fulfillment of the requirements for the degree of

MASTER OF SCIENCE

In Mechanical Engineering

MICHIGAN TECHNOLOGICAL UNIVERSITY

2018

© 2018 Yash Borghate

This thesis has been approved in partial fulfillment of the requirements for the Degree of MASTER OF SCIENCE in Mechanical Engineering.

Department of Mechanical Engineering-Engineering Mechanics

Thesis Advisor: *Dr. Jeffrey D. Naber*

Committee Member: *Dr. Mahdi Shahbakhti*

Committee Member: *Garlan Huberts*

Department Chair: *Dr. William W. Predebon*

Table of Contents

List of Figures

ix

List of Tables

List of Abbreviations

SOI	Start of first injection in Compression Stroke
EOI	End of second injection in Expansion Stroke
SR	Split ratio
AFR	Air Fuel Ratio
FAR	Fuel Air Ratio
MFB	Mass Fraction Burn
IMEP	Indicated Mean Effective Pressure
HCR	Hydrogen to Carbon Ratio
OCR	Oxygen to Carbon Ratio
MW	Molecular Weight
BTDC	Before Top Dead Center
ATDC	After Top Dead Center
CA10	Location of 10% Mass Burned
CA50	Location of 50% Mass Burned
CA90	Location of 90% Mass Burned
DI	Direct Injection
TWC	Three Way Catalyst
MAP	Manifold Air Pressure
RPM	Rotations Per Minute
RGF	Residual Gas Fraction
IVO	Intake Valve Closing
EVC	Exhaust Valve Closing
RMSE	Root Mean Square Error

List of Symbols

T	Temperature
T_m	Body Temperature
T_g	Gas Temperature
COV_{IMEP}	Coefficient of Variance of IMEP
SD_{IMEP}	Standard Deviation of IMEP
n_{poly}	Polytropic coefficient
γ	Specific Heat Ratio
P	Pressure
V	Volume
θ	Crank Angle
Q_{ch}	Fuel Chemical Heat Release
$PolyC$	Polytropic Coefficient of Compression
$PolyE$	Polytropic Coefficient of Expansion
W	Work Done
V_d	Displaced Volume
R	Reaction coefficient for one mole of C
m	Mass
$\dot{m}$	Mass Flow Rate
n	Number of Moles
y	Mole Fraction
x	Mass Fraction
$\dot{m}_{g(k)}$	Mass Flow Rate of Exhaust Gas
C_p	Specific Heat at Constant Pressure
Ai	Inner Surface Area

Ao	Outer Surface Area
h_{sa}	Convective heat transfer coefficient between surface and air
h_{gs}	Convective Heat Transfer Coefficient between gas and surface
K	Thermal Conductivity
A_{cross}	Cross-section Area
x	Length
h_{fg}	Latent Heat of Vaporization
t	Time
R^2	R-squared
R_{shunt}	Shunt Resistance
R_{sen}	Sensitivity Resistor Value
X_{scale}	Scaling Factor
V_{bias}	Bias Voltage
V_{offset}	Offset Voltage

List of Subscripts

in	Inlet
out	Outlet
$manifold$	Exhaust Manifold
$turbo$	Turbocharger
cat	Catalyst
atm	Ambient
$cond$	Condensation
$evap$	Evaporation
$partial\_burn$	Partial Burn
spk	Spark

Acknowledgement

I would like to thank a lot of people who helped, supported and guided me during my entire time of research at Michigan Tech. Firstly, I would like to thank Dr. Jeffrey Naber for agreeing to be my advisor and giving me an opportunity to pursue my master's research work under his guidance. I'm thankful for all his continuous support and guidance throughout my research work.

Secondly, I would like to thank Dr. Mahdi Shahbakhti, who acted as my co-advisor, for sharing his experience and guidance in the field of this research work. His previous work in cold start testing provided a guideline for this cold start research.

Thirdly, I would like to extend my appreciation to Mr. Garlan Huberts from Ford Motor Co. for his continuous support for the work I've done and for letting me carry out the research work at Ford facility during the summer. Also, I would like to thank Darren Nester who mentored me during my work at Ford facility. I would also like to extend my appreciation to Michael Czekala, Chad Archer and Qiuping Qu for their help and guidance.

I would also like to thank my friends Amir Khameneian, Xin Wang and Kaushik Prabhu who helped me throughout my entire research work and during the engine performance tests and Paul Dice for the experimental setup and test cell.

Last but not least, I would like to thank my parents Dr. Vijay Borghate and Sunita Borghate and other loved ones for their continuous support which kept me motivated during this work.

- Yash

Abstract

In this thesis, two different works related to cold start of a direct-injection (DI) gasoline engine are shown. First, effect of split injection is studied on engine exhaust temperature and hydrocarbon emissions for cold start conditions. Instead of single injection, two injections are done, one injection during the intake stroke and one injection during the compression stroke. Split injection is known to reduce jet wall wetting, thus reducing the hydrocarbon emissions from engine itself. Further, split injection reduces engine cycle-by-cycle variability with respect to the single injection case.

Correlations between start of injection for the injection in the intake stroke (SOI), end of injection for the injection in the compression stroke (EOI) and Split Ratio (SR) with Exhaust Temperature (T_{exh}) and engine hydrocarbon emissions are proposed with the help of design of experiments (DOE). These correlations could be used for controlling exhaust temperature during cold start.

Second, because of repetitive marshalling of a vehicle, i.e. cold start the engine on the vehicle and drive it a few feet and then turn it off, spark plugs are observed to get fouled. A spark plug is considered to be fouled when the insulator nose becomes coated with a foreign substance including oil, fuel or carbon. This enables the ignition coil voltage to follow along the insulator nose and ground out rather than bridging gap and firing normally.

A tool to measure quasi real-time spark plug fouling is proposed in this work, which uses in-cylinder ion data to measure offset voltage which is then used to calculate spark plug shunt resistance. Based on the spark plug shunt resistance, fouling level of the plug can be calculated, and the condition of the plug can be determined.

Chapter 1

Introduction

1.1 Motivation

Split Injection Correlation and Exhaust Thermal Model

Internal Combustion (IC) Engines are one of the major consumers of fossil fuel. This also leads to increase in emissions from these vehicles [1]. Recently, there have been technological advances in the field of Electric Vehicles (EV), however, there is still production cost of the battery associated with the vehicle which makes it expensive. Low range of operation and large time in recharging batteries may cause reluctance to switch to EV's. Also, there aren't enough charge stations for the EV's in the remote locations of the country favoring internal combustion cars. Therefore, automotive manufacturers cannot fully depend on the electric vehicle, resulting in large fraction of vehicles to be still powered by IC engines in the following years. Therefore, it becomes important to continue research in IC engines to make it more efficient and less harmful to the environment.

Cold start emissions of an IC engine are a major problem. The three main pollutants in a gasoline engine are Carbon Monoxide (*CO*), Nitrogen Oxides (*NOx*) and hydrocarbon emissions (*HC*) [2]. It is well known that emissions during cold start is significantly higher than when the engine is warmed up [3][4]. More than 90% of the allowable HC emissions are emitted during cold start [5][6] which can be seen from Figure 1.

Modern gasoline stoichiometric engines use a three-way catalytic converter which results in large reduction in all these emissions. The efficiency of the catalyst depends on the

1

temperature of its substrate. A typical catalyst is known to function efficiently for temperatures above 350-400°C known as its light-off temperature. Therefore, for a cold start condition where all the engine's and catalyst's temperatures are at room temperature, it becomes important to reach catalyst's light-off temperature as quickly as possible so that the conversion of toxic gases is to non-toxic gases is maximum.
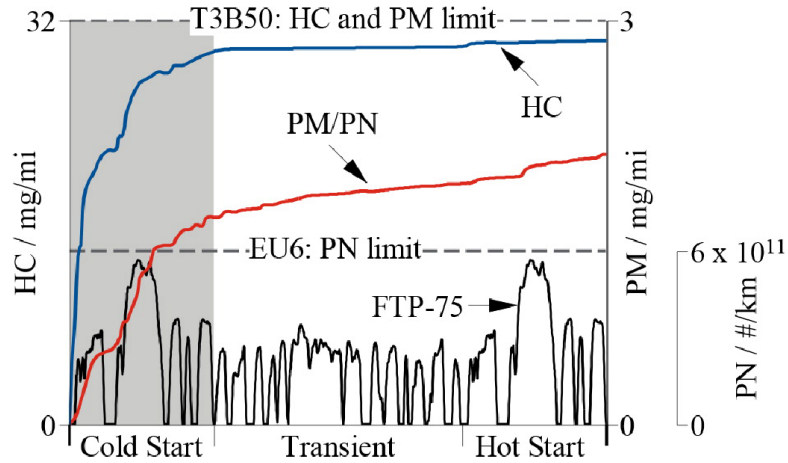
Figure 1: Cumulative tailpipe HC and PM/PN emissions over the FTP-75 cycles for GDI engines [6]

Exhaust temperature from each cylinder is measured via thermocouple and temperature of exhaust gas going inside the catalyst is and the substrate temperature is measured via thermocouples installed on the catalyst. To determine the light off temperature of the catalyst, it is important to model the catalyst temperature. To model the catalyst temperature, it is necessary to also model all the components downstream from the engine exhaust gas including exhaust manifold, turbocharger, and the connecting pipes between the components.

Spark Plug Diagnostic Tool

2

IC engines are required to meet stringent emissions standards enforced by EPA. A lot of research is going on decreasing emissions, without affecting the performance and fuel economy of the engines. To meet the emissions demands, a closed loop combustion controls is required to study the combustion. Many sensing devices are used to analyze combustion including pressure sensors, optical sensors, and ion sensors. This thesis focusses on two different studies, one done using ion sensor and other done using in-cylinder pressure sensor.

Ion sensors are used to detect knock, partial burn, detect misfire, to determine air fuel ratio, to determine flame speed, late burns, diffusion flame, etc. Ion current can be sensed either via stand-alone ion sensor or via spark plug of the engine. The method of ion sensing using the spark plug is explained in Chapter 8.

Spark plugs in an Internal Combustion engine are known to get fouled over time. Fouled plugs deteriorate combustion stability during idling, acceleration and sometimes under heavy fouling engine startup failure. Deposition of carbon particles, ferrocene deposits, MMT deposits, or liquid fuel on the tip of the electrodes of plug decreases the shunt resistance of the plugs. Ignition energy source leaks through the deposits thus preventing the center electrode to reach the voltage required to generate the spark. This leads to misfires in the engine and results in poor combustion stability.

It has been observed that because of repetitive marshalling of newly assembled vehicles, i.e. cold start the engine and move the vehicle a few feet and shut the engine off, spark plugs tend to get fouled. This process takes 15 – 20 seconds and doesn't allow the spark plug temperature to reach high enough to evaporate the fuel deposits on the electrodes. Cold temperature during marshalling plays an important role in plug fouling as the engine component's temperature too low for adequate evaporation of the fuel. Therefore, it is important to maintain the plugs clean for a better product delivery to the customer. One

of the technique to clean the spark plug is to take the vehicles on a drive and drive it enough to that the temperature of the plugs is hot enough to burn off the deposits on the electrodes. But, this technique is time consuming and requires work force. Calibrators are continuously developing 'Alt Cal' which is the alternate calibration for the engine to be used until before supplying the vehicle to the customer. Hence, it is important for the calibrators to understand and study plug fouling and what are the calibration parameters which plays an important role in plug fouling.

1.2 Research Scope

Split Injection Correlation and Exhaust Thermal Model

For the cold start split injection work, this thesis focuses on developing correlations between the *SOI, EOI, SR* and *SA* with engine exhaust temperature and combustion parameters including *CA50*, burn duration, ignition delay, etc. The correlations are developed using test data and performing regression analysis on it and fitting a curve on the data. A thermal model of exhaust system is proposed which includes exhaust manifold, turbocharger and catalyst. Exhaust manifold and turbocharger are modeled as lumped models and are used to estimate the outlet temperature for both exhaust manifold and turbocharger. Here, turbocharger is considered as a thermal body for cold start as the work produced by turbocharger during cold start is negligible. Catalyst is considered to have a axial thermal gradient. Two catalyst thermal models are proposed showing two different techniques for calculating heat transfer of re-vaporization of condensed water in catalyst.

Spark Plug Diagnostic Tool

4

This work focusses on developing a tool which would measure the spark plug fouling quasi real-time which can be used to study plug fouling and develop alternate calibration. The tool would use in-cylinder ion data from each cylinder of the engine and would output the plug shunt resistance or each spark plug as an indication for the fouling of the plug. This tool would only work for spark plug as an ion sensing probe. New alternate calibrations are being developed continuously and this tool would help calibrators to understand and study spark plug fouling. This tool will also help save Calibrators time of removing, observing, and reinstalling the plugs every time they check for plug fouling manually. The algorithm will have to be modified to make it use for standalone ion sensor. Plug resistance can only be calculated when the spark plug is used as the ion probe – V_{offset} used in equation (60) cannot be measured for the plug otherwise.

1.3 Overview of Thesis

The content of the thesis in different chapters is as follows.

In Chapter 2, background study and previous work done on cold start of a spark ignited engines is discussed. Discussion is mainly about the challenges in cold start and the strategies applied to overcome those challenges. A brief study of modeling of exhaust downstream components to estimate the catalyst light-off time is also shown.

In Chapter 3, information about the experimentation is shown. The geometry of engine, the fuel used for testing, the software used and the instrumentations on the engine like thermocouples is discussed in this chapter.

In Chapter 4, information about all the equations used for modeling the exhaust thermal model and different techniques used in modeling is discussed. Also, two different techniques in calculating the combustion parameters is shown in this chapter.

5

Chapter 5 gives the correlation of split injection parameters with the combustion parameters (like CA50, burn duration, etc.) and the exhaust thermal model. This chapter also includes the comparison between the estimated exhaust temperatures and the measured exhaust temperatures.

Chapter 6, the summary and conclusion of the work done so far and suggestions for future work is mentioned.

In Chapter 7, a literature review of work done previously regarding plug fouling analysis and solutions to prevent plug fouling is shown. Different ways to measure plug fouling and factors leading to plug fouling is mentioned. A brief study of ion current measurements is also shown. It also demonstrates basic information about the ion signal recorded using spark plug as ion probe.

In Chapter 8, information about the engine used for the tests and the instruments used to log and analyze data is shown. The ion measuring technique is explained in this chapter. Also, the software used for computation is mentioned.

Chapter 9 describes algorithm used to calculate the spark plug fouling. A schematic of the algorithm is also shown in this chapter which facilitates the understanding of data recording and analysis.

Chapter 10 provides a guide to use the GUI running on the algorithm mentioned in Chapter 4. It also shows how to study and interpret the resulting graphs to determine the fouling on the spark plug. Also, different levels of fouling cases are shown in this chapter.

6

Finally, in Chapter 11, the conclusion of the work is mentioned and suggestions for modification if the tool is to be used in high performance engine with number of cylinders more than 8.

Chapter 2

2.1 Cold Start Background and Literature Review

Cold start is starting the engine is cold, relative to the normal operating temperature. The transient nature of component temperature, engine speed and MAP (Figure 2) during cold start leads to cyclic variations [7]. This may lead to combustion instability and poor emissions.
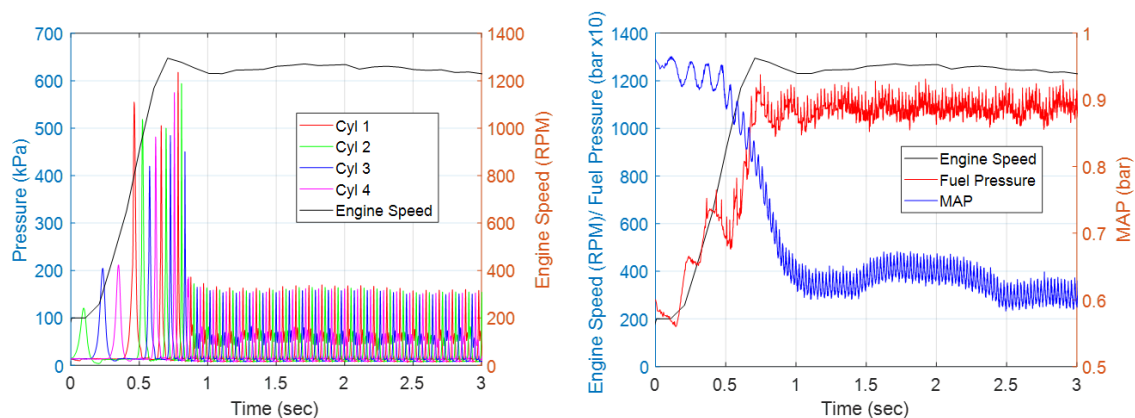
Figure 2: (Left) Engine Speed and In-Cylinder Pressure Data during Cold Start; (Right) Engine Speed, MAP and FRP during Cold Start; plotted from data sent by Ford Motor Co.

There are primarily three major pollutants from spark ignition engines which are *CO*, *HC* and NO_x [4]. It is known that more than 90% of the total tailpipe *HC* emissions are emitted during first few cycles of cold start[2][5][6]. Hence the engine operation control strategies emphasis greatly on reducing the bulk of *HC* emissions during the cold start. This can be done by reducing the emissions in the engine itself and/or by reaching the catalyst light-off temperature as quickly as possible. The importance of catalyst temperature/ gas temperature inside the catalyst during cold start can be seen in Figure 3 which shows the effect of catalyst temperature on HC conversion efficiency of the catalyst.
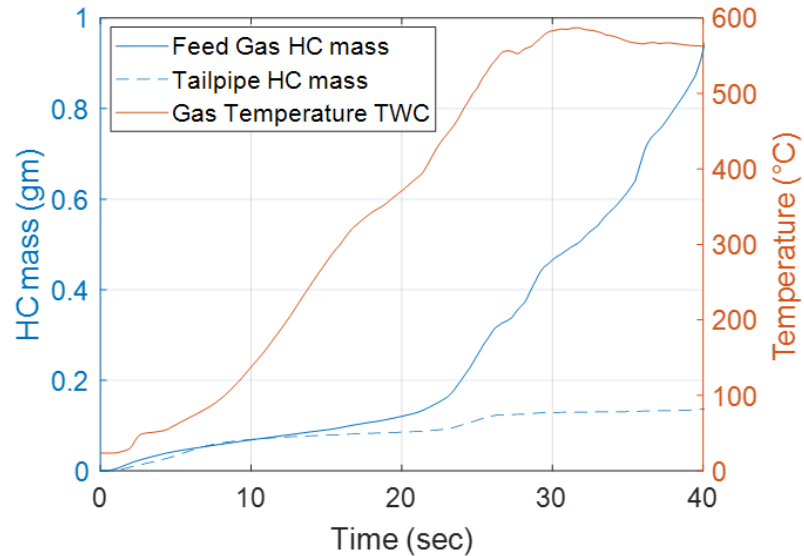
Figure 3: Cumulative HC mass and Exhaust Gas Temperature measured after first brick of Catalyst during Cold Start; plotted from data sent by Ford Motor Co.

The factors contributing to the emissions, combustion stability and catalyst temperature are shown in Figure 4. The blocks in blue are the independent control parameters, the blocks in yellow are the intermediate parameters and the blocks in green are the resulting parameters of our interest. The circles with same number are the connection between the blocks from which it is coming out and going in. The independent parameters (blocks in blue) includes controlling parameters like throttle angle, cam positions, fuel rail pressure, spark timing and split injection parameters including *SOI*, *EOI* and injection fuel split mass and parameters affected by ambient conditions like wall temperature and inlet air temperature. The parameters in the yellow blocks, which are affected by the parameters in blue blocks and will affect the parameters in the green blocks can be seen from the causality diagram. For example, air mass inside the engine depends on the manifold air pressure (*MAP*), engine speed and cam position. The *MAP* value depends on the throttle position.

9
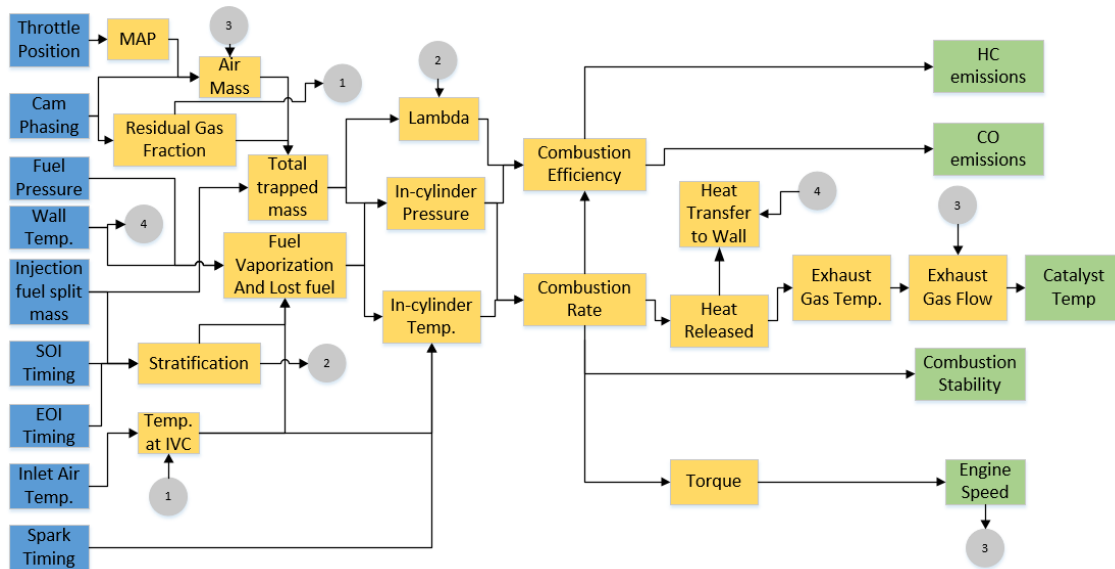
Figure 4: Causality Diagram for a gasoline engine Emissions, Combustion Stability and Catalyst Temperature

Several reasons account for the bulk emissions of *HC* during the cold-start. The main reasons are discussed in the following discussion.

Cold Engine Walls

Operating wall temperature of the engine is usually 90°C in warmed up engine. Cold walls during cold start makes stable combustion difficult due to heat loss to the engine walls. If the heat transferred to the walls exceeds the heat generated by combustion, this would result in poor mixing quality and possibly a lean mixture resulting in a difficulty to ignite. Cold walls and reduced charged temperature also lead to higher fuel impingement on the walls which results in higher engine out *HC* emissions.

Catalyst Light-Off not Achieved

Although a Three-Way Catalyst (*TWC*) is used to reduce the emissions form the engine, the catalytic reaction is highly temperature dependent. At temperatures below light off

temperature (<350°C), a significant amount of emissions escapes the catalyst without getting converted until the light-off temperature is reached (Figure 5). The temperature at which the conversion rate is 50% is known as the light-off temperature. For the graph shown in Figure 5, light-off temperature can be seen when the first brick temperature is 350°C.
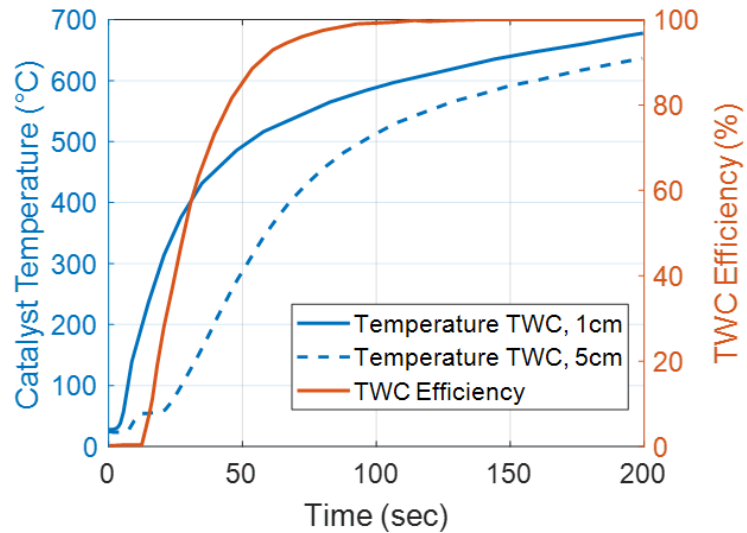
Figure 5: Catalyst temperatures at 1cm and 5cm downstream of Catalyst face with Catalyst Efficiency, generated from data in [8]

Low Fuel Rail Pressure

Because of the relatively low engine speed (<300 RPM), it is difficult for the fuel pump to build pressure during cold start. Low fuel pressure results in larger fuel droplet size which reduces fuel air mixing and vaporization. This reduces the combustion efficiency which in turn increases *HC* emissions.

Cam Phasing Inoperative

11

Similar to fuel rail pressure, it is difficult to build engine oil pressure to phase the cam locations. Cams are typically left in default positions when the engine is last turned off. These positions are generally not the optimum positions which leads to inefficient control of trapped mass inside the cylinder leading to higher amount of injected fuel for combustion resulting in increased *HC* emissions. [38]

Open Loop Oxygen Sensor Control

The oxygen sensor installed in the downstream of the exhaust system is used determine if the air fuel mixture is rich or lean. This is used as a feedback signal to control the amount of fuel and air to make the engine run at stoichiometric condition. The oxygen sensor only works above a certain temperature [9]. The oxygen sensor is turned on as soon as the exhaust is not condensing. During cold start, because of the low operating temperature of the oxygen sensor, the oxygen sensor control is in open loop which affects the efficient control of *AFR*[10].

With the above cold start limitations, it becomes important to reach the catalyst light-off as early as possible and to keep the combustion stability under limit which would control *HC* emissions. Choi et al [11], did experiments to determine relation between spark timing and *HC* emissions. He concluded that exhaust temperature increases with retard in spark timing. He also concluded that engine out *HC* increased when spark was extremely retarded ATDC because of aggravated combustion stability. Figure 6 shows how the average temperature of the exhaust gas and catalyst bed temperature (left) and catalyst temperature profile with different spark timings. It can be seen that the exhaust temperaure increases as the spark retards.
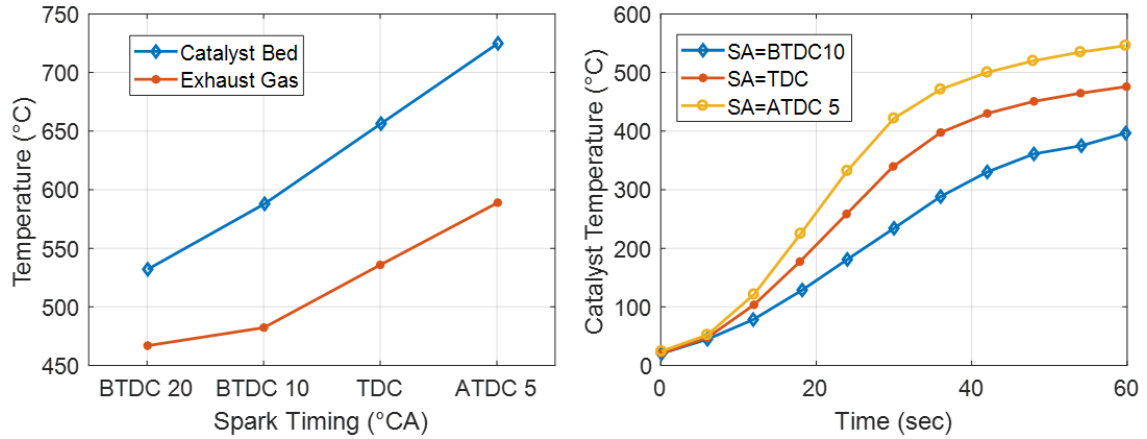
Figure 6: Effect of Spark Timing on Exhaust Gas Temperature; (left) Exhaust Gas Temperature and Catalyst Bed Temperature with Spark Timing; (right) Catalyst Temperature Profile with Spark Timing, created from data in [11]

Cedrone and Chen [12], performed study to see if valve timing can be used to improve the catalyst warm up time. They concluded that exhaust temperature can be increased by using valve timing to change the residual gas fraction with overlap. Although, the drawback of using high valve overlap or increasing residual gas fraction is the large COV_{IMEP}. The COV_{IMEP} rapidly increases beyond residual gas fraction of 30% (Figure 7). They stated that combustion retard with spark retard is a better option than combustion retard with increasing residual gas fraction as spark retard will produce higher exhaust gas enthalpy flow as suppression of exhaust temperature due to dilution is absent. The left graph in Figure 7 shows exhaust thermal energy flow in Watts with cam overlap.

13
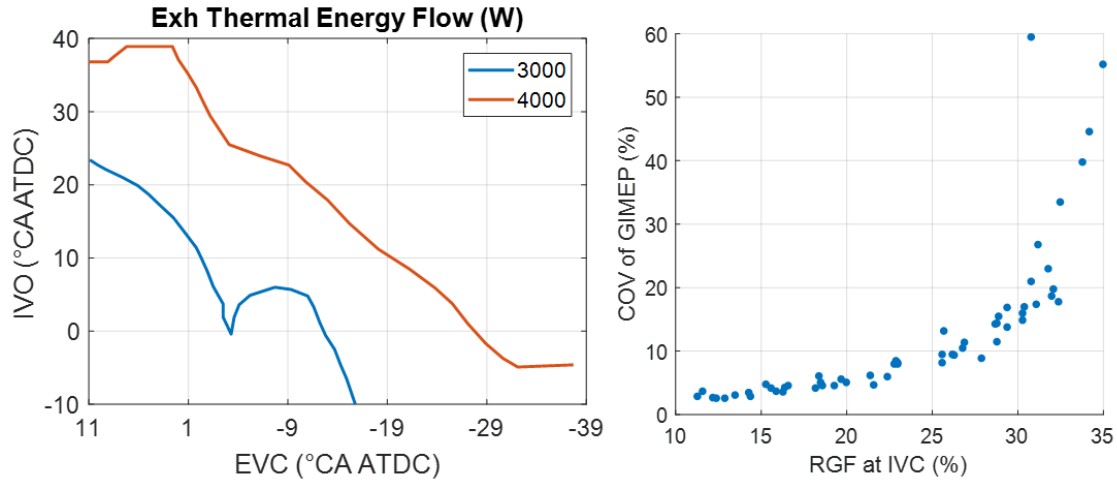
Figure 7: (Left) Exhaust Thermal Energy Flow with Cam Overlap; (Right) COV(GIMEP) with Residual Gas Fraction, generated from data in [12]

James A. Eng [5] stated five major reasons for HC emissions as shown below.

1) Storage of fuel in combustion chamber crevices
2) Absorption of fuel into deposits and oil layers
3) Liquid fuel within the cylinder too rich to burn
4) Quenching of combustion chamber surfaces
5) Partial burns

James with his 0-D ring pack crevice flow model and experimentation to determine the effect of ignition timing on *HC* emissions with lean and rich mixture and concluded that there is a sweet spot for *CA50* for lowest crevice *HC* emissions for rich as well as lean conditions (Figure 8). The HC emission is higher for *CA50* advanced or retarded than the sweet spot. He also determined that the temperature at *EVO* increases with retard in *CA50*.

14
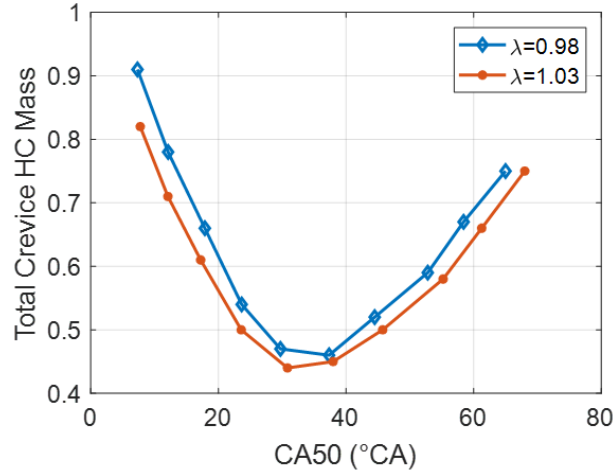
Figure 8: Total Crevice HC Mass for Rich and Lean Condition vs CA50; plot generated from data in [5]

Lee et al. [13] with their experiments concluded that injection timing is the key parameter to improve combustion stability for a direct injection SI engine for cold start idling. Figure 9 shows a comparison of combustion stability at two different ambient temperatures during cold start for a GDI engine. The ignition timing was optimized for lowest possible COV_{IMEP}. Engine performance at higher ambient temperature (24 °C) shows better idle COV_{IMEP} compared to the range of injection timings at lower ambient temperature (20 °C).
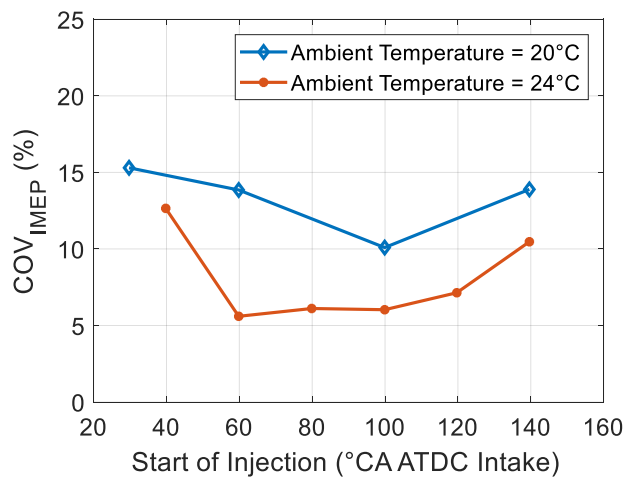
Figure 9: Injection Timing and Temperature Effects on DI Cold Start Combustion Stability; plot generated from data in [13]

15

A common practice to improve the combustion stability during cold start is doing split injection. One injection is done in the intake stroke and the second injection is done in the compression stroke. Xiangdong Chen et al. [14], from his experimentation on a GDI engine concluded that Standard Deviation of Net IMEP reduces when single injection is switched to split injection for cold start (engine and ambient temperature at about 20°C). Figure 10 shows combustion stability comparison between single injection and split injection. The engine speed and load were 1350 rpm and 1.5 bar *NMEP*. The split ratio for the fuel he used was 80:20 meaning 80% was injected in the first cycle and 20% was injected in the second injection. The timing for the end of second injection was -8 to 8 Crank Angle Degree (CAD) relative to spark.
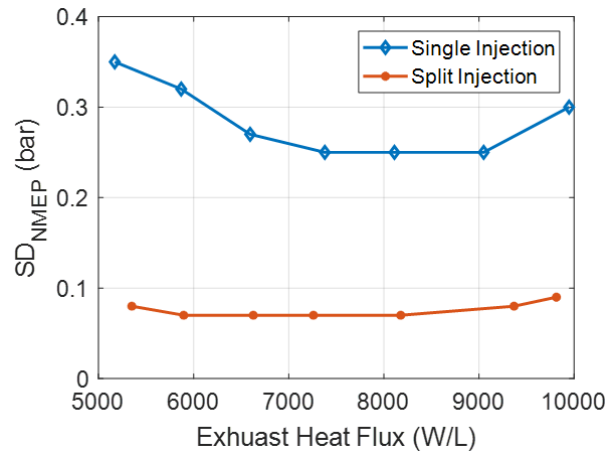
Figure 10: Comparison of single injection and split injections on combustion stability

Another study done by Q. Fan et al [15], performed a study to find the optimum injection timing of split injection and fuel split ratio. He concluded that extremely early or late first injection is timing is unfavorable. The second injection should be at least 90 CAD BTDC for cranking speed of 400 RPM and excess ratio of 1. Misfire occurs if the second injection timing is advanced than 90 CAD BTDC for this condition. The timing of second injection has more effect on combustion than the first injection and, also the amount of 2nd fuel injection should be higher for better combustion stability. First injection at 120 CAD ATDC

16

(intake), second injection at 60 CAD BTDC (spark) and split ratio of 0.5 is proposed for 400 RPM for stable first cycle combustion.

Costa et al [16], compared the effect of single injection and split injection a GDI engine for a fixed engine speed, first injection and spark timing. The results are showed in Table 1. Cyclic variability increases as the second injection timing approaches TDC.

Table 1: Performance comparison for single and split injection at 2000 RPM and 7.7 bar IMEP; from data in [16]

RPM	SOI1 (°BTDC)	SOI2 (°BTDC)	SA (°BTDC)	IMEP (bar)	COV_{IMEP} (%)	Pmax (bar)
2000	300	-	15	7.8	3.0	42.6
2000	300	80	15	7.6	4.6	30.1
2000	300	100	15	7.7	3.7	33.8
2000	300	140	15	7.7	2.3	41.5
2000	300	200	15	7.7	2.6	41.6

The advantages of split injection are the increase in the cylinder pressure and reduces NO_x and *HC* values as shown in Figure 11.
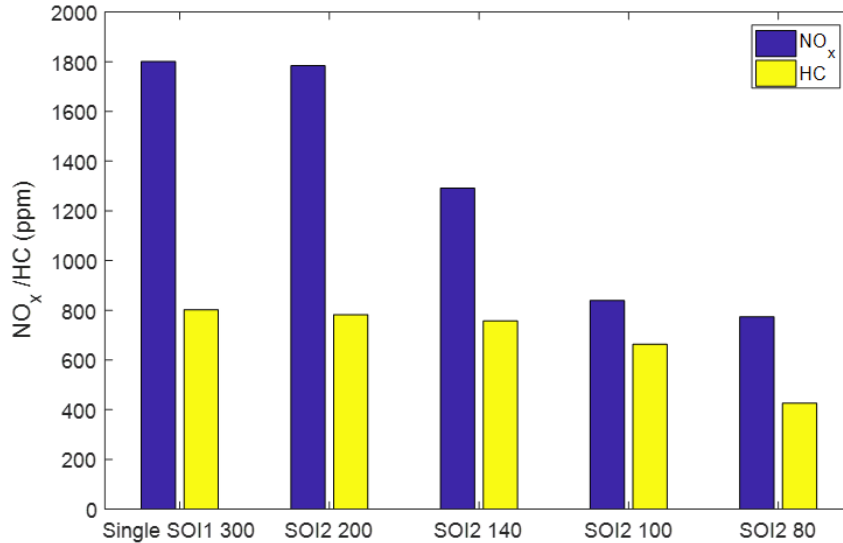
Figure 11: Emissions comparison of Single and Split Injection; plotted from data in [16]

Ritchie et al. [17] performed a study on split injection with gasoline, ethanol and DMF on a direct injection spark ignition engine. Using gasoline, with fuel injection ratio of 2:1 (SOI1:SOI2), increase of IMEP by 1.2% was found when SOI2 timings were between 240 and 90 CAD BTDC at WOT. He concluded that *CO*, *HC* and NO_X emissions are better in split injection strategy than in single injection. This is found when *SOI2* timings are early (*SOI2*>180 CAD BTDC) with fuel injection ratio of 2:1.

Cedrone and Chen [18] in another paper concluded that the exhaust sensible enthalpy is mainly determined by combustion phasing. When ignition timing is changed from 7 CAD BTDC to 17 CAD BTDC, the *CA50* location shifts from 36 to 84 CAD ATDC (Figure 12) and the exhaust gas temperature varies linearly from 525K to 750K. The variation is linear as the NMEP is held constant at 2 bar.
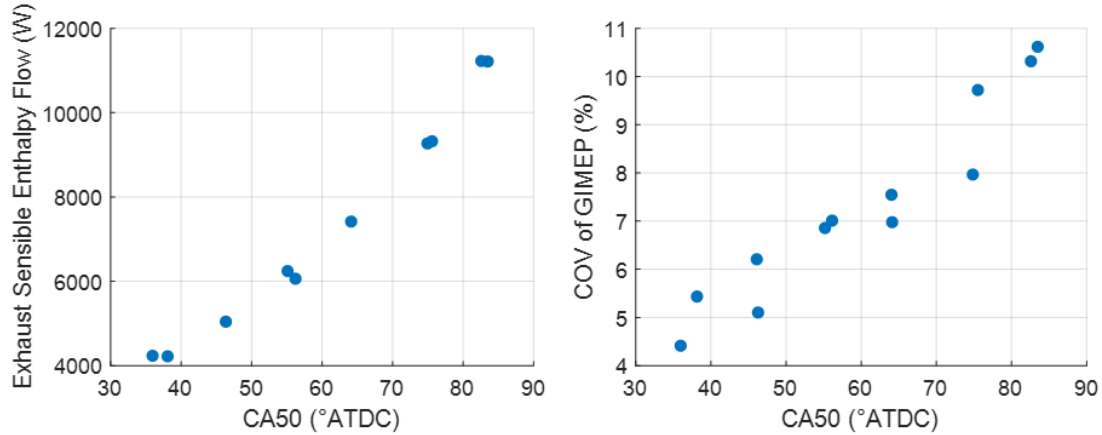
Figure 12: Effect of CA50 on Exhaust Sensible Enthalpy Flow and COV of GIMEP; plotted from data in [18]

At constant IMEP the exhaust chemical enthalpy increases with retard in ignition because higher air charge is required for to compensate for decreasing conversion efficiency. They also studied the effect of second injection on CA50 values, COV_{IMEP} and exhaust temperature. A split of 70:30 by fuel volume was used keeping the first injection timing fixed at 60 CAD ATDC-intake. The engine was made to run at stoichiometric conditions for the experiments. From Figure 13 it can be seen, as the second injection timing is retarded, the *CA50* also retards for given timing of ignition till a certain crank angle (290 CAD ATDC-intake) after which the *CA50* starts advancing. As the *CA50* location retards, the COV of *GIMEP* also increases. It can also be observed that as the *CA50* location retards from 50 to 60 (CAD ATDC), the exhaust gas temperature also increases from 640°C to 720°C.

19
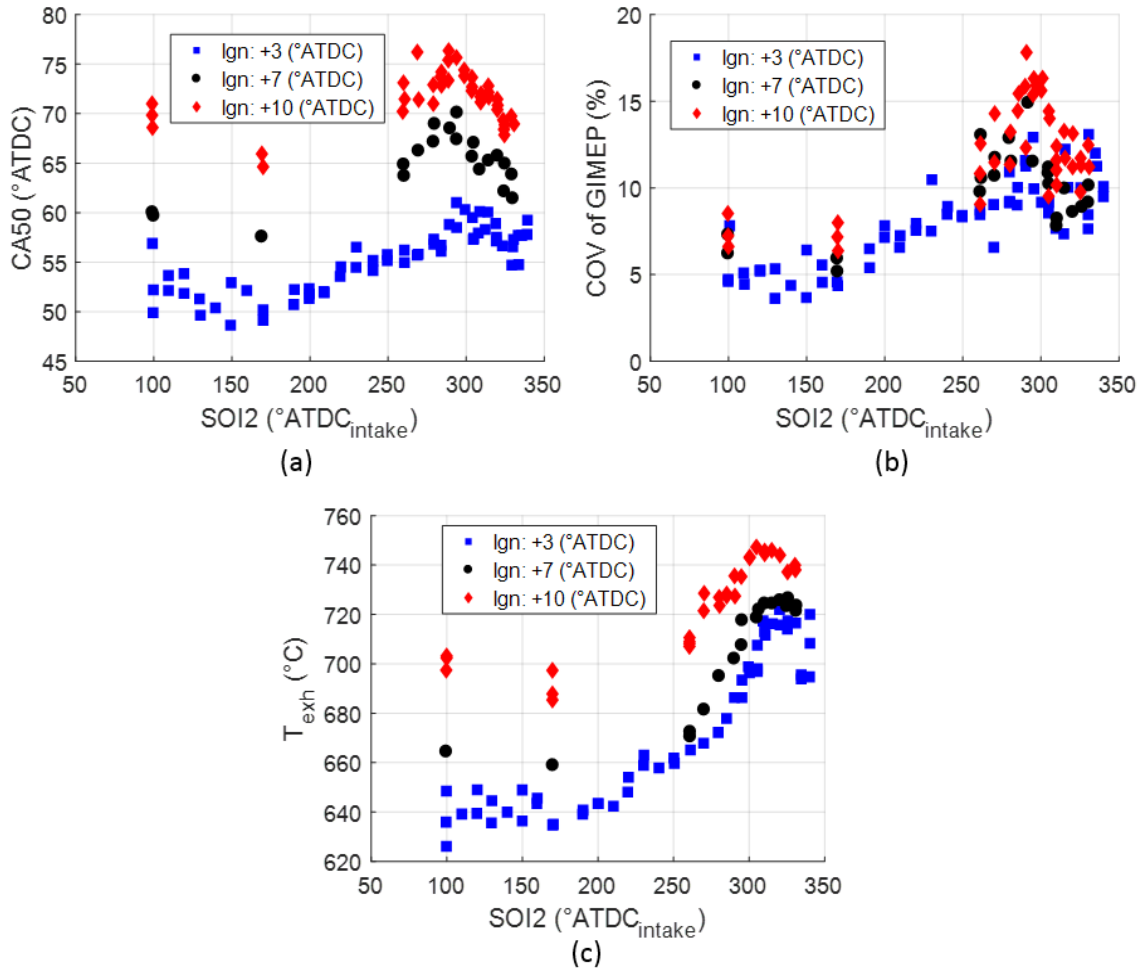
Figure 13: Effects of Second Injection timing on (a) CA50, (b) COV of GIMEP and (c) Exhaust runner temperature for different ignition timings; plotted from the data in [18]

2.2 Cold Start Literature Review Summary

Highly retarded spark timing has been studied in detail and its effects on exhaust gas temperature, *CA50* and combustion stability have been shown. From these studies, a number suggest the most efficient way of increasing the exhaust gas temperature is by retarding the spark timing for faster catalyst light-off. However, all the studies show a limitation on the extent of the spark timing retard as the combustion stability starts to deteriorate.

20

The effect of multiple injections on the combustion stability has also been studied in the literature. Split injection reduces the problems related to wall and/or piston wetting which helps in improving the combustion stability. All these studies are mainly in regard with cold start of the engine. Although, the effect of timing of the first injection is studied to be insignificant, the effect of second injection timing on exhaust gas temperature, *CA50* and combustion stability is studied.

While these studies provide the basis on the trends of *CA50* and exhaust temperature with spark retard and split injection, there is a lack of study which gives correlation between the control parameters including split injection parameters and spark timing on combustion parameters (like *CA00-10, CA50, CA10-90*) and exhaust gas temperature. Thus, the intent of this research is to provide correlations which can be further used for understanding the sensitivity of these parameters and for future control purposes.

2.3 Exhaust Thermal Model Literature Review

Temperature of the catalyst during cold start should be carefully controlled. The catalyst is generally not active below 350 -400°C and begins to age rapidly above 1000°C. Severe ageing of the catalyst can occur at temperatures above 1400°C and the substrate itself can melt [36]. As this research concerns the cold start operation of the engine, our focus is on the reaching the catalyst light-off temperature.

Peyton Jones et al. [37] describes the catalyst models typically fall into one of the following three categories.

1)   Detailed physical model based on fundamental chemical and thermos-fluid dynamic principles. They include heat and transfer equations in three-dimensional

21

accounting the change in exhaust gas composition as the continuously react with each other in the catalytic environment.

2) Simplified kinetic models, based on the reactions between various gas components, as well as the gas storage on the catalyst surface. Such models can be represented by coupled, lumped parameters. These models are required to have input gas composition either measured or predicted.

3) Simplified models, based on the assumption that catalyst behavior is based on the dynamics of gas storage. Models like these contain single non-linear dynamic characterization of input/output AFR response.

The oxygen storage potential of the catalyst is well studied in different literatures. However, [36] show that the storage and release of oxygen is not significant during the cold start conditions. Typically running the engine on the rich side results in less oxygen in the exhaust for the catalyst to store. Also, the oxygen storage mechanism of absorption/ desorption is dependent on transient AFR over a wide range of engine operation. However, steady state conversion efficiency of the engine has an important role during cold start operations of the engine. The conversion efficiency can be described as the "S" shaped Wiebe function.

$$y = 1 - \exp\left[-a(\frac{u - u_0}{\Delta u})^m \right] \qquad (1)$$

Where, u_0 is the ordinate at y = 10% and Δu the difference in u and a and m are fitting parameters. This Wiebe function can be extended to two-dimensional equation of catalyst efficiency (η) as a function of temperature (T) and phi (ϕ) as shown in the following equation.

22

$$\eta = 1 - \exp\left[-a_1(\frac{\phi - \phi_0}{\Delta\phi})^{m_1} - a_2(\frac{T - T_0}{\Delta T})^{m_2}\right] \qquad (2)$$

Andrianov et al. [19] developed a cold start emission model of an SI engine and aftertreatment system. This included developing thermal models for downstream components from engine like exhaust manifold, connecting pipes and three-way catalyst. The exhaust thermal model in this thesis is similar to the one developed by Andrianov. Thermal modeling is done using only convective heat transfer and applying the first law of thermodynamics on the gas, and neglecting the kinetic energy, equations for the exhaust manifold model are made. Similar equations are used in modeling exhaust manifold model proposed in this thesis. Also, similar equations are extended to the turbocharger model proposed in this work. Nusselt number is calibrated for convective heat transfer coefficient values to calibrate the exhaust manifold model by Andrianov, whereas, the model proposed in this work, convective heat transfer multiplied by the surface area value is used to calibrate the exhaust manifold and turbocharger model.

Gonzalez et al [20], developed a catalyst model considering the water vapor condensation inside the catalyst during cold start conditions for a gasoline engine operating at stoichiometric conditions. Assuming stoichiometric combustion, equation (3) is used to estimate the mass of water vapor in the exhaust gas.

$$C_8H_{18} + \frac{25}{2}(O_2 + 3.76N_2) \rightarrow 8CO_2 + 9H_2O + 47N_2 \qquad (3)$$
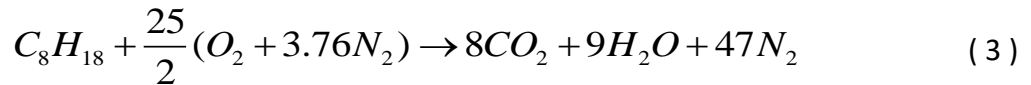
From this equation for gasoline (approximated as Isooctane), it is derived that 1.4 kg of water vapor is produced per kg of fuel burned and, also partial pressure of water vapor in exhaust gas is determined to be 0.14 bar. With the value of partial pressure of water vapor, the dew point of the exhaust gas is determined to be 53 °C using the vapor pressure

23

curve for water as shown in Figure 14. Having calculated the dew point temperature, the mass of condensed water is calculated with saturation pressure at each temperature.
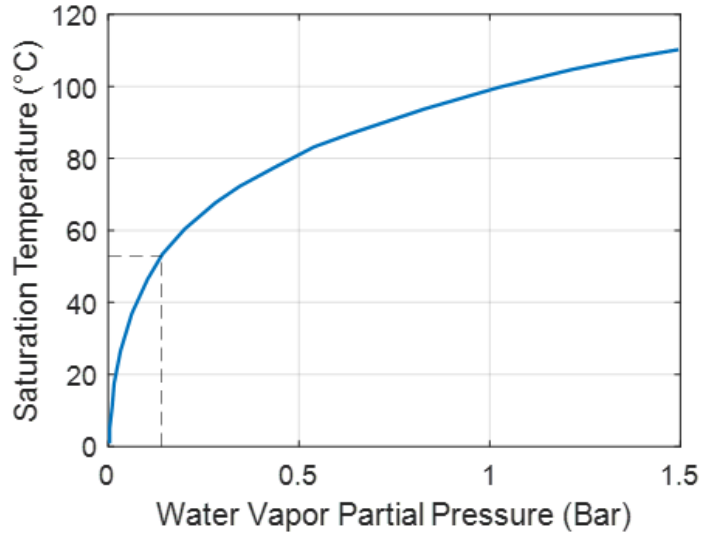
Figure 14: Vapor Pressure curve for water; plotted from data in [20]

2.4 Exhaust Thermal Model Literature Review Summary

Simple thermal models are studied in details and a similar simple model is proposed in this thesis for exhaust manifold, turbocharger and catalyst. Although all the catalyst models studied have included exhaust gas reaction equations occurring inside the catalyst, whereas, the model proposed in this thesis, the exhaust gas reaction equations are neglected and only focused on the heat transfer between the gas and the catalyst substrate.

A stoichiometric equation is solved for E10 fuel as done by Gonzalez et al [20] for gasoline (Isooctane), and water vapor concentration is calculated which is used to calculate the dew point temperature for the exhaust gas and amount of water condensed inside the catalyst at low temperatures.

24

Chapter 3

3.1 Experimental Setup

A four-cylinder Ford 2.0L Ecoboost direct-injection turbocharged spark-ignition engine was used for testing split injection. The engine is located in APSRC lab facility of Michigan Technological University. Characteristics of the engine are given in Table 2. The fuel used for testing was gasoline E10 with the fuel properties are shown in Table 3.

Table 2: 2L Ford Ecoboost Engine Specifications

Bore	87.5 mm
Stroke	83.1 mm
Connecting Rod Length	155.86 mm
Wrist Pin Offset	0.6 mm
Compression Ratio	9.3:1
Engine Displacement	1.999 L
Number of Cylinders	4
Firing Order	1-3-4-2

Table 3: E10-87 AKI Test Fuel Properties

Carbon (Wt%) [m/m]	83.06
Hydrogen (Wt%) [m/m]	13.48
Oxygen (Wt%) [m/m]	3.46
Density [kg/m^3]	741.9

Lower Heating Value [*MJ/kg*]	41.725
Stoichiometric Air-Fuel Ratio (AFR)	14.06
Research Octane Number [-]	91.7
RVP [*kPa*]	65.7
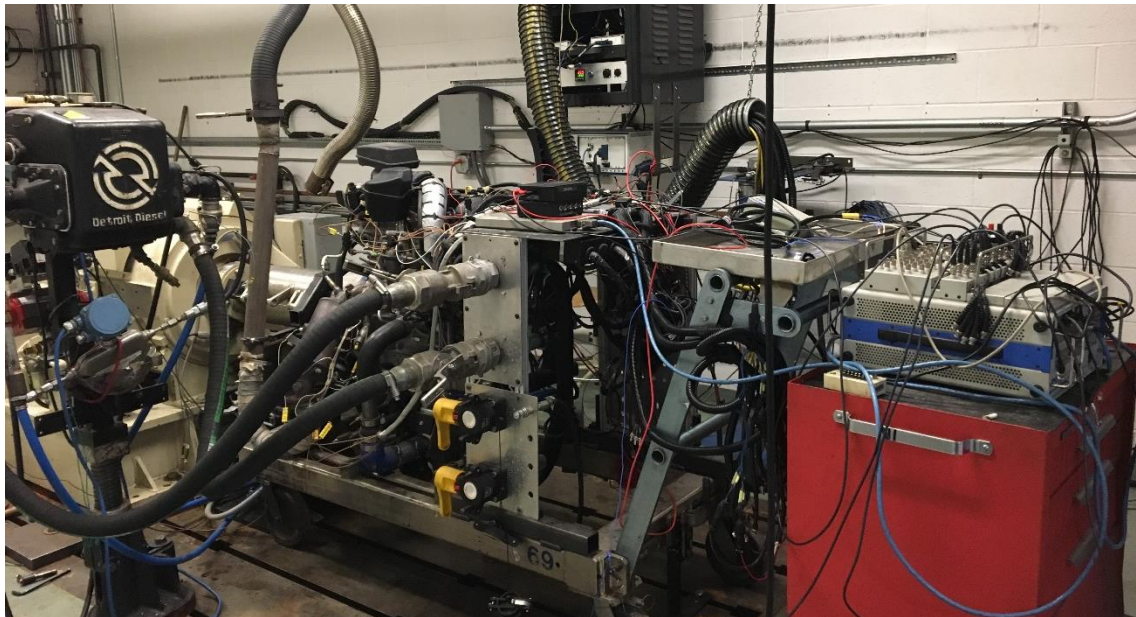
Figure 15: 2.0L Ford Ecoboost engine with AC Dynamometer

The engine is coupled to an AC dynamometer which is used to control the speed of the engine (Figure 15). National Instruments LabVIEW [21] software is used as a software interface to control the speed of the dynamometer. Temperature measurements using thermocouples are also logged using LabVIEW [21]. ATI Vision software [22] is used as the ECU interface to control the engine controlling parameter including load, air/fuel ratio, injection timing, valve timing, spark timing, etc. Combustion Analysis Software (CAS) [23] is used to track and analyze real time combustion parameters although a few combustion

26

parameters from CAS cannot be trusted which will be discussed later. CAS is used to log combustion parameters including in-cylinder pressure, IMEP, etc.
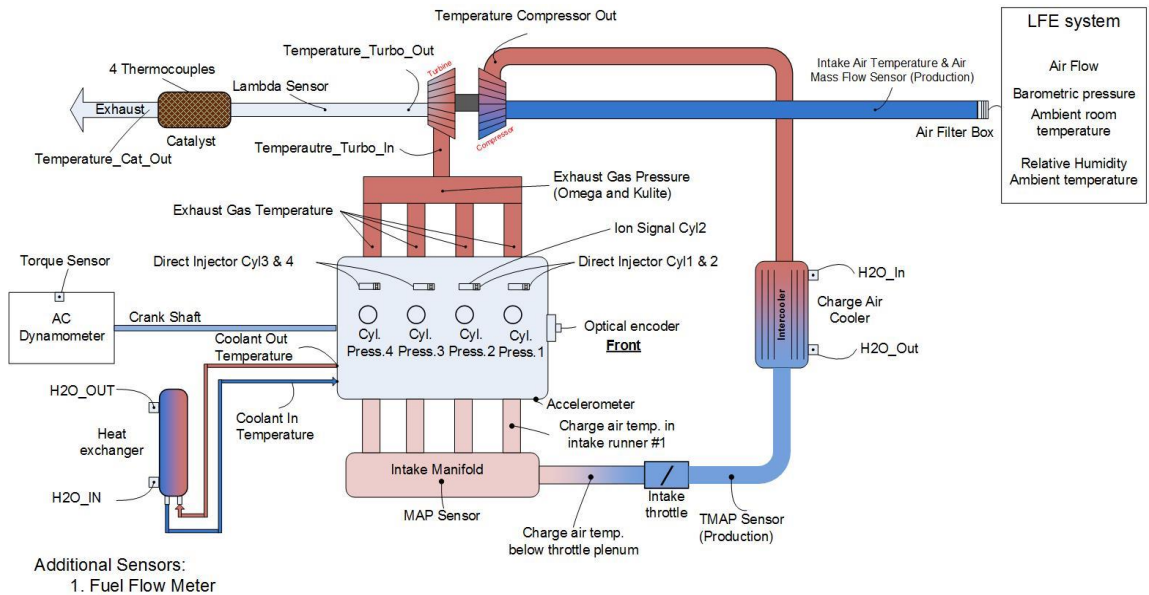
Figure 16: Engine Instrumentation Overview

Figure 16 shows an overview of the instrumentation on the Ford 2.0L engine. Each cylinder of the engine is equipped with Kistler 6125A pressure transducer used to log in-cylinder pressure data. This pressure data is used to calculate the combustion parameters including *CA50, CA00-10, CA10-90*, etc. *IMEP* is also calculated using pressure data. A BEI HS25 Incremental optical encoder attached to the engine and allows to log data for every 0.5 crank angle giving a good resolution of the data recorded.

As shown in Figure 17, there are four 1/8" K-type ungrounded thermocouples installed in the exhaust port near the exhaust valve measuring the temperature of the exhaust gas coming out of the engine form each cylinder. One 1/8" K-type ungrounded thermocouple to measure the exhaust manifold temperature is installed on the block between the exhaust manifold and turbocharger. Another 1/8" K-type ungrounded thermocouple installed on the same block is used to measure the exhaust manifold outlet temperature

going to the turbocharger. The cold junction compensation (CJC) for these thermocouples are done in the DAQ system itself.
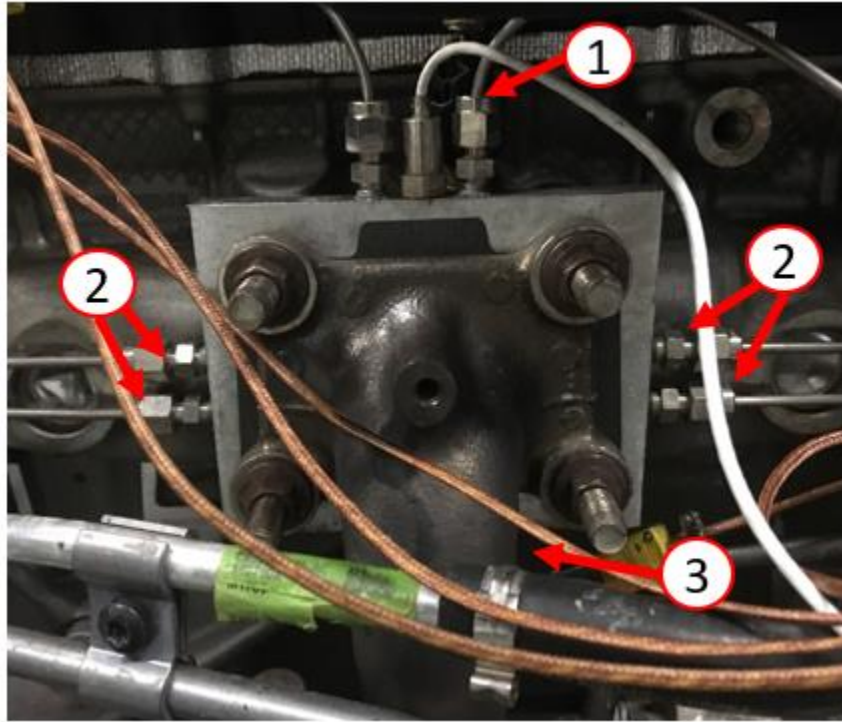
Figure 17: Exhaust Thermocouples; 1. Exhaust Manifold Body Temperature, 2. EGT located at the exhaust valve for 4 cylinders, 3. Exhaust Manifold Outlet Temperature

Inlet temperature of the exhaust gas is measured by a thermocouple located at the inlet of the catalyst. Four thermocouples are installed on the catalyst at various locations as shown in Figure 18 to measure the exhaust gas temperatures. The catalyst was provided by Ford Motor Co. and the exact location/ penetration and type of the thermocouples were unknown. The thermocouple shown as 'Catalyst In' in the Figure 18 serves two purposes in model calibration. One, it is used as Turbine Outlet temperature for calibrating Turbocharger model and second, as a Catalyst Inlet temperature while calibrating the Catalyst model. Another thermocouple located at the outlet of the catalyst is used to measure the exhaust gas temperature.

28
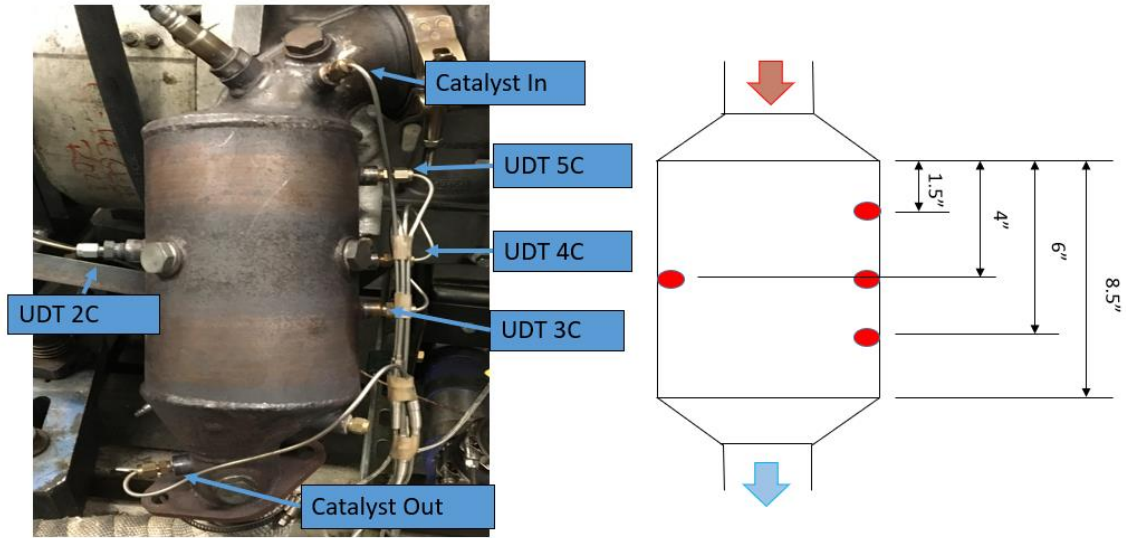
Figure 18: Three-Way Catalyst with thermocouples measuring exhaust gas temperatures at different locations

A summary of the sensors used in this study is shown in Table 4.

Table 4: Summary of sensors used for the study

System	Sensor	Make/Model	Signal Name	DAQ/ Software
In-Cylinder Pressure	Pressure Sensor	Kistler - 6125A Serial Number Cyl1: 615358 Cyl2: 615359 Cyl3: 953358 Cyl4: 641982	PresTrace.Cyl1 PresTrace.Cyl2 PresTrace.Cyl3 PresTrace.Cyl4	CAS
Crank Angle	Optical Encoder	BEI HS25	tqca1	CAS
Exhaust Gas Temperature near valve	Thermocouple	1/8" K-type Ungrounded	EGT 1 EGT 2 EGT 3	NI

			EGT 4	
Exhaust Manifold Outlet Temperature	Thermocouple	1/8" K-type Ungrounded	Right Bank Turbine In	NI
Turbine Outlet / Catalyst Inlet Temperature	Thermocouple		EGT Right Bank Turbine Out Converter In	NI
Exhaust Gas Temperatures inside Catalyst	Thermocouple		UDT 2C UDT 2C UDT 4C UDT 5C	NI
Catalyst Outlet Temperature	Thermocouple		EGT Right Bank Converter Out	NI

3.2 Experimental Procedure

Tests for Split Injection Correlations

Cold start tests were conducted for developing correlations for split injection parameters with combustion parameters and exhaust temperature. A test procedure was developed to simulate cold start and to have repeatability. The tests were done at 1250 RPM and engine load of 2.5± 0.2 bar IMEP. The following test procedure was followed.

1) Engine IMEP changes when either of the four controlling parameters (*SOI, EOI, SR* and *SA*) is changed. Hence, it is required to adjust throttle angle for each combination of *SOI, EOI, SR* and *SA* to maintain *IMEP* at 2.5 bar. The throttle

adjustment for a combination of *SOI, EOI, SR* and *SA* was done when the engine was warmed up and the throttle angle was noted.

2) Once the throttle angle was noted, the engine was motored using the motoring capability of the AC dynamometer until the coolant temperature drops down to 33°C.

3) Engine was made to run at all preset control parameters value of *SOI, EOI, SR, SA* and throttle angle at 1250 RPM and the CAS data was logged in 'Startup Combustion' mode. The 'Startup Combustion' mode allows data to be recorded at the start of the engine. 1000 cycles of data were recorded.

4) After completing the test, *SOI, EOI, SR* and *SA* values were changed for the next test data point, and the throttle angle was noted for next data test point and the procedure is repeated.

Tests for Validation/ Calibration of Thermal Model

The test procedure for the tests to validate the thermal model was as follows. The engine was allowed to cool overnight to ensure all the engine component's temperatures were the same as the ambient temperature. The data logging in CAS was set in 'Startup Combustion' mode and engine was started with a constant throttle angle to produce ~2.5 bar *IMEP* at 1250 RPM. Data including exhaust temperatures, in-cylinder pressures, etc. were recorded for the first 8000 cycles (CAS allows data logging up to 8000 cycles).

31

Chapter 4

Combustion Parameters Calculation

4.1 Equations Used for Combustion Parameters Estimation

It is known that by doing split injection the combustion stability improves [13][14]. Split injection is defined when one injection is done in the intake stroke and one injection in the compression stroke. *SOI* refers to start of first injection and *EOI* refers to end of second injection timing. As mentioned earlier, ATI Vision software [22] is used as the ECU interface to control the operating parameters of the engine. Thus, it allows to override values for *SOI* and *EOI* timings whereas, end of injection for the first injection and start of injection for the second injection timing is determined by the software depending on the amount of fuel to be injected and fuel rail pressure. For a certain lambda value, the injected fuel for each injection is determined by Split Ratio (*SR*). *SR* equals 1 refers to when all the injection happens in first injection and *SR* equals 0 means all the injection happens in the second injection while compression. Figure 19 shows the schematic of split injection. As we are dealing with cold start conditions, it is better to have retarded spark timing (after TDC) for quicker light-off of the catalyst [11].
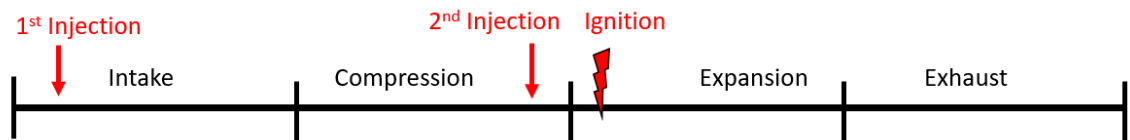
Figure 19: Schematic of Split Injection

In-cylinder pressure trace is used to calculate the combustion parameters on per cycle basis. Crank angle-based pressure data was recorded every 0.5 CA for first 1000 cycles.

An average of these for a particular test is used to find correlations between the combustion parameters and controlling parameters including start of injection, split ratio and ignition timing. Pressure trace is used to calculate combustion parameters including *CA50*, *CA00-10* and *CA10-90*. The values of these parameters are based on polytropic indices of compression and expansion. As we are dealing with cold start condition, partial burn of the fuel is to be considered while calculating the combustion parameters. Details are discussed later in this chapter.

4.1.1 Polytropic Indices Calculation

Polytropic indices are calculated form the in-cylinder pressure curve and volume of the cylinder using the below formula. This polytropic index is calculated for compression as well as expansion according to the following equation.

$$n_{poly} = \frac{\ln(P_2) - \ln(P_1)}{\ln(V_2) - \ln(V_1)} \qquad (4)$$

Where *P* is the absolute cylinder pressure, *V* is the cylinder volume, and 1 and 2 are points in the compression and expansion stroke.

Crank Angle (*CA*) equal to -180 CAD refers to Bottom Dead Center (BDC) in compression stroke and 180 CAD refers to BDC after expansion. 0 CAD indicates Top Dead Center (TDC) of expansion stroke.

Usually -90 to -50 BTDC is chosen as 1 and 2 points for calculating polytropic index for the compression stroke. Similarly, for calculating expansion polytropic coefficient, 70 to 110 ATDC interval is chosen. Figure 20 shows the log P-V diagram for a typical advanced combustion. Polytropic indices are the slopes of the curve in the compression and

33

expansion region. The curve highlighted by blue color shows the interval for calculation of compression polytropic coefficient and the curve highlighted in green shows the interval for calculation of the expansion polytropic coefficient. The diamond on the curve shows the spark timing.
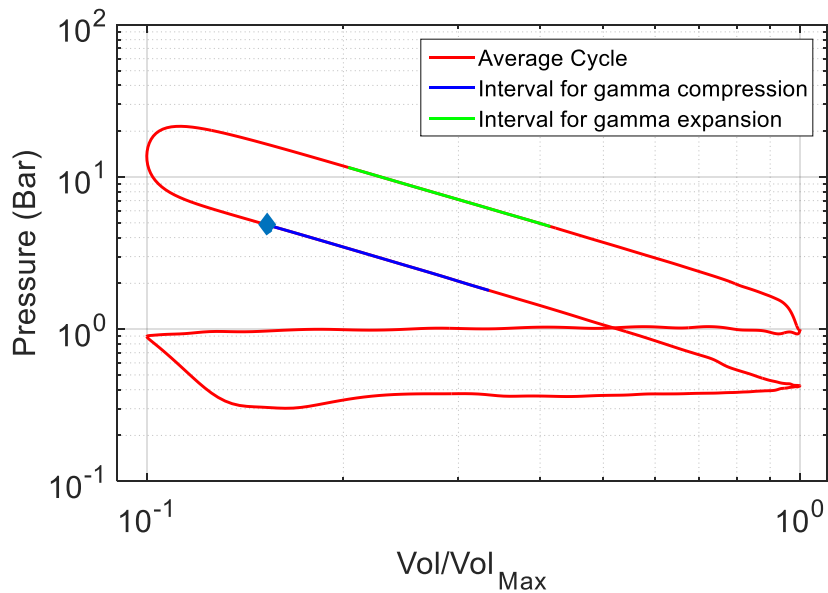
Figure 20: Log PV diagram for Advanced Combustion

4.1.2 Heat Release Rate Calculation

Heat Release Rate is calculated using the pressure data with volume and the polytropic indices. The equation used to calculate the heat release rate is as follows [24].

$$\frac{dQ}{d\theta} = \frac{n_c}{n_c - 1} P \frac{dV}{d\theta} + \frac{1}{n_c - 1} V \frac{dP}{d\theta} \tag{5}$$

Where Q is the apparent heat released, n_c is the combustion polytropic coefficient, P and V are the instantaneous pressure and volume values. The data logged is logged every 0.5

34

CA. Therefore, the continuous differential equation must be approximated. Central difference method is used in our case for the approximation.

$$\frac{dQ_{(i)}}{d\theta_{(i)}} = \frac{n_{c(i)}}{n_{c(i)}-1}P_{(i)}\frac{V_{(i+1)}-V_{(i-1)}}{\theta_{(i+1)}-\theta_{(i-1)}} + \frac{1}{n_{c(i)}-1}V_{(i)}\frac{P_{(i+1)}-P_{(i-1)}}{\theta_{(i+1)}-\theta_{(i-1)}} \qquad (6)$$

Where, i is increment every 0.5 CA which gives the heat released rate values every 0.5 CA. Combustion γ value used here can be interpolated from compression and expansion polytropic indices, which are calculated from log P-V diagram as shown in Figure 21. CA_{HR_start} refers to the crank angle at which heat release start and CA_{HR_stop} refers to the crank angle at which heat release stop.
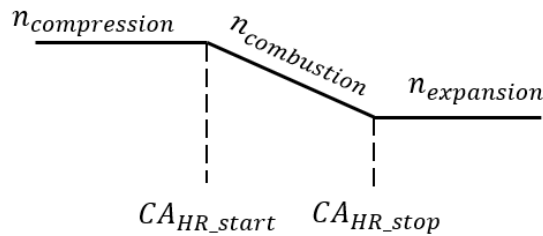
Figure 21: Schematic of interpolation for calculating combustion gamma

Heat released can be calculated by integrating equation (5).

4.1.3 Combustion Parameters Calculation

Combustion Delay (*CA00-10*), 50% mass burn location (*CA50*) and Burn Duration (*CA10-90*) are important parameters defining combustion characteristics. The polytropic coefficient should is a vital parameter for calculation of combustion parameters. For retarded combustion, where combustion is still happening for the interval 70 to 110 CAD ATDC, will lead to unreliable values for PolyE. This gives incorrect values for Mass Fraction Burn (MFB). Two methods are proposed for to deal with this issue.

35

Method A

As the PolyE values are incorrect, one way is to ignore the PolyE values and work with just PolyC values instead. This will prevent from calculating wrong MFB values.

Method B

Another method proposed in this work is changing the interval for calculation of expansion polytropic coeffect from 70 - 110 CAD ATDC to 7 to Ignition timing plus 12 CAD. Figure 22 shows the modified interval for calculation of expansion polytropic coefficient.
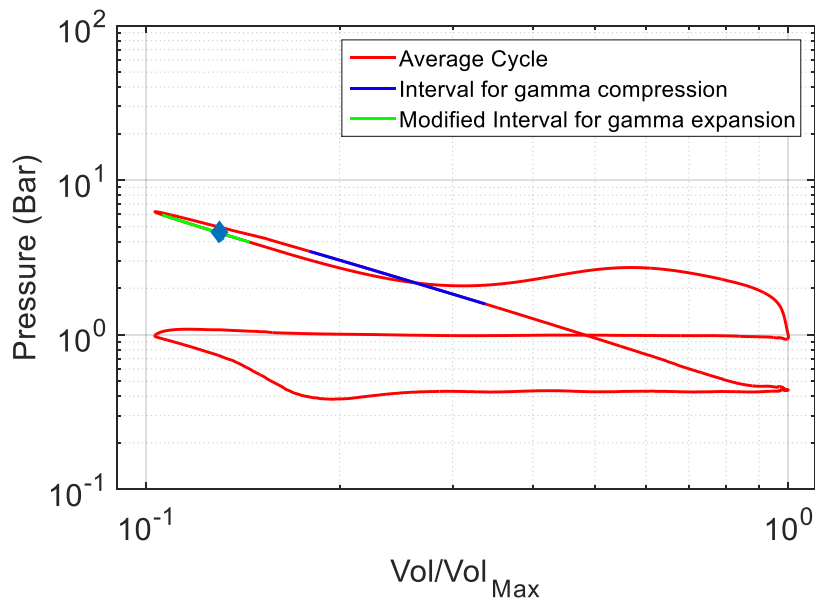
Figure 22: Log PV Diagram for Retarded Combustion

Heat released is often used to calculate the location of mass fraction burned by normalizing its values by the net heat released for the same cycle. Heat released normalized by its maximum value at every crank angle per cycle would give the curve for

36

MFB. It is assumed that all the injected fuel is burned during combustion promotes the idea of diving the heat released values by its maximum value.

$$MFB = \frac{Q}{\max(Q)} \qquad (7)$$

As this work focusses on the cold start on an engine, because of the cold walls, lower temperatures, higher heat transfer to the wall, there may rise a situation where cycles may not burn completely. Hence, engine cycles with partial burn are also taken into consideration while calculating the mass fraction burn curve.
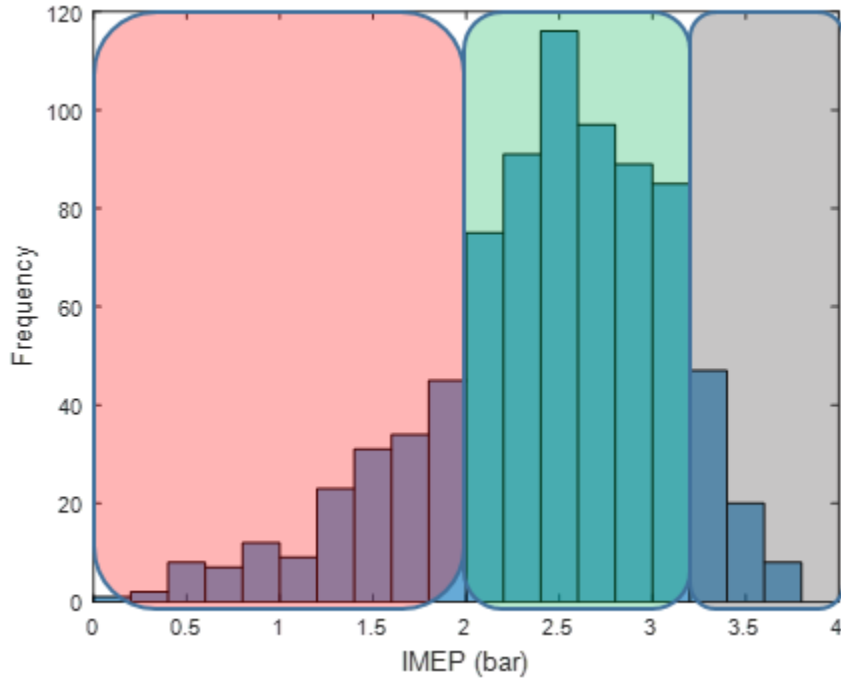
Figure 23: IMEP distribution for test -70 CAD BTDC EOI, 340 CAD BTDC SOI, 0.7 SR and 15 CAD ATDC, target IMPE = 2.5 bar @ 1250 rpm; Red- partial burn, green - complete burn, grey - high IMEP due to preceding partial burns

Figure 23 shows a sample test data with IMEP distribution indicating partial burns cycles in the data set. For a sample test data run at steady state, heat release values for all the

www.manaraa.com

cycles is sorted in ascending order and median of the sorted heat release is recorded. 80% of the median is calculated and used as a threshold for determining partially burnt cycles. For all the cycles above the threshold, equation (7) is used for mass fraction burn calculations. For the cycles having Q lower than the threshold, the mean of all the cycles having Q more than the median value is calculated and used in the denominator for mass fraction burn calculations as shown in equation (8). Because of this, there may be a few cycles which would not have CA90 or CA50 values.

$$ MFB_{partail\_burn} = \frac{Q_{partail\_burn}}{mean(Q > Q_{median})} \tag{8} $$

4.1.4 Indicated Mean Effective Pressure

In cylinder pressure data of the engine over an engine cycle can be used to calculate the work transfer from the gas to the piston of the engine. The cylinder pressure and corresponding volume can be plotted, and area enclosed in the curve gives the indicated work (W). Work delivered to the piston over compression and expansion stroke only gives gross indicated work (W_{ig}) whereas, if all four strokes are considered it becomes net indicated work (W_{in}).

$$ W = \oint PdV \tag{9} $$

Indicated mean effective pressure (*IMEP*) is an important factor for comparing performance of engines with different displacement volume. It is a representation of how much work has been produced by the piston in an engine cycle. This can be calculated using the in-cylinder pressure data against crank angle or cylinder volume. IMEP can be classified either as Gross IMEP or Net IMEP depending on whether Pumping loss is

38

accounted or not. Gross IMEP is calculated for the compression and expansion cycle, neglecting pumping whereas Net IMEP is calculated for an entire cycle of 720 CAD.

$$IMEP_{g\_or\_n} = \frac{W_{ig\_or\_in}}{V_d}$$ (10)

Where, $IMEP_{ig\_or\_in}$ is indicated mean effective pressure (gross or net), $W_{ig\_or\_in}$ is the indicated work produced (gross or net) on the piston and V_d is the displaced volume.

Coefficient of Variance of IMEP (COV_{IMEP}) and **Standard Deviation of IMEP** (SD_{IMEP}) are important factors in determining cycle to cycle variation of combustion which defines combustion stability. Standard deviation is a measure to represent variation in the data set. A low standard deviation means the data points tends to be close to the mean whereas, a high standard deviation value means the data points are spread out. Similarly, higher value of SD_{IMEP} or COV_{IMEP} represents spread out data points meaning higher cycle to cycle variation of combustion showing unstable combustion. The equation for standard deviation is given below.

$$SD = \sqrt{\frac{\sum_{i=1}^{N}(x_i - \bar{x})^2}{N-1}}$$ (11)

Where, N is the number of points (x) in data set and $\bar{x}$ is the mean of the points in the data set. The correlation between the coefficient of variance and standard deviation for a data set is as follows,

$$COV_{IMEP} = \frac{SD_{IMEP}}{mean(IMEP)} \times 100 \qquad\qquad (12)$$

Gross COV_{IMEP} is a popular parameter to define combustion stability for normal advanced combustion, but, because this study is regarding cold start where IMEP values are pretty low (<2.5 bar), we use SD_{IMEP}. This is done because the low values of IMEP for cold start and any small variation in IMEP would show large COV_{IMEP} which gives false interpretation. Typically, less than 2% COV_{IMEP} or 7 kPa SD_{IMEP} is considered as a limit for combustion stability for part load conditions. For idle conditions where IMEP is lower than part load, 10-14 kPa SD_{IMEP} is the limit for combustion stability as per Ford's guidelines.

Exhaust Thermal Model

4.2 Equations Used for Exhaust Thermal Model

To determine the light-off time of the Three-Way Catalyst (TWC), it is important to estimate the temperature of the TWC based upon energy to the exhaust flow and loses to the environment. To estimate the catalyst temperature, all the downstream components from the engine including the exhaust manifold, the turbocharger and the connecting pipes are required to be modeled. The body temperature of all the components depends on the temperature of the inlet gases into the component and the mass flow of the exhaust gases.

4.2.1 Combustion Equation

Ideal combustion of the E10 fuel produces CO_2, H_2O, O_2 and N_2. Solving these equations for the coefficients for a, b, c and d would give the number of moles of CO_2, H_2O, O_2 and N_2 respectively for 1 mole of C. This can be used to calculate the partial pressure and mass fraction of the water vapor.

$$CH_{HCR}O_{OCR} + R \cdot \lambda \cdot (O_2 + 3.77N_2) \rightarrow a \cdot CO_2 + b \cdot H_2O + c \cdot O_2 + d \cdot N_2 \quad (13)$$
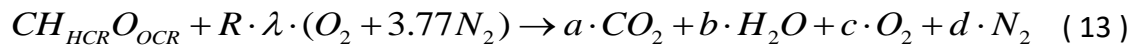
HCR is the Hydrogen to Carbon molar ratio. OCR is the Oxygen to Carbon molar ratio. These values can be obtained from the fuel properties. R is the reaction coefficient for one mole of Carbon which is given by the following equation.

$$R = 1 + \frac{HCR}{4} - \frac{OCR}{2} \qquad (14)$$

Table 5: Combustion equation values for E10 fuel for lambda =1

Variable	HCR	OCR	R	a	b	c	d
Value	1.93	0.03	1.46	1	0.96	0	5.54

4.2.2 Dew Point Temperature Calculation

During a cold start operation, because of the temperature of the exhaust components being at the room temperature, the temperature of the exhaust gases tends to fall below its dew point temperature. This leads to condensation of water vapor present in the exhaust gases, as can be seen from equation (13). To calculate the mass flow of water vapor in exhaust gases, chemical equation of fuel combustion is to be solved. The solving of chemical equation requires the knowledge of mass to mole conversion which is done using the following equation,

$$n_i = \frac{m_i}{MW_i} \qquad (15)$$

Here n_i is the number of moles, m_i is the mass and MW_i is the molecular weight. Mole fraction is the number of moles of each component divided by the total number of moles.

42

This is required to calculate the partial pressure of the water vapor in the exhaust gases. It is later used to calculate the dew point temperature.

$$y_{H_2O,vapor} = \frac{n_{H_2O,vapor}}{n_{CO_2} + n_{O_2} + n_{H_2O,vapor} + n_{N_2}}$$

(16)

To determine the mass of water vapor in the exhaust gases, mass fraction is used. This value is used to calculate the water vapor holding capacity of the air and the dew point temperature. For lambda equal to 1, $y_{H2O,vapor}$ is calculated to be 0.12.

$$x_{H_2O,vapor} = \frac{(n_{H_2O,vapor} \cdot MW_{H_2O,vapor})}{(n_{CO_2} \cdot MW_{CO_2}) + (n_{O_2} \cdot MW_{O_2}) + (n_{H_2O,vapor} \cdot MW_{H_2O,vapor}) + (n_{N_2} \cdot MW_{N_2})}$$

(17)

Mixing ratio or Mass Mixing Ratio is the mass of water vapor divided the mass of dry air. This ratio is used to estimate the Dew Point Temperature of the exhaust gas. The dew point temperature for E10 fuel for stoichiometric combustion is 326 K.

4.2.3 Exhaust Manifold Thermal Model

The exhaust manifold thermal model incorporates the exhaust manifold as well as the exhaust valves. Heat transfer from the exhaust valves are also considered while modeling exhaust manifold. The exhaust thermal model estimates the temperature of the exhaust gas at the outlet of the exhaust manifold as a function of inlet temperature of the exhaust gas of the exhaust manifold. The model for the exhaust manifold is modeled as lumped model with convective heat transfer. It is assumed that the flow is incompressible and is at steady state. Kinematic variation in the flow including filling in the exhaust manifold for the first cycle, heat transfer between the exhaust gases from first cycle and the gases

43

already present inside the exhaust manifold when the engine was run last, etc. are neglected.
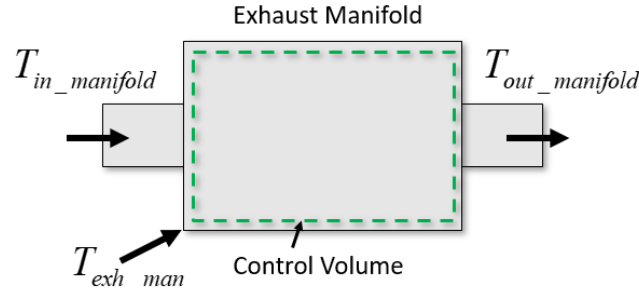
Figure 24: Schematic of Exhaust Manifold Control Volume

Figure 24 shows a schematic of the exhaust manifold control volume. Applying the first law of thermodynamics to the exhaust manifold control volume gives the following equation (18).

$$\dot{m}_{g(k)} \cdot C_{p\_g} \cdot (T_{in\_manifold(k)} - T_{out\_manifold(k)}) =$$
$$h_{gs\_manifold} \cdot A_{i\_manifold} \cdot (T_{g\_manifold(k)} - T_{m\_manifold(k)})$$

(18)

Where, $\dot{m}_{g(k)}$ is exhaust gas mass flow rate for k^{th} cycle, C_{p_g} is the heat capacity of exhaust gas in constant pressure process, $T_{in\_manifold(k)}$ is the temperature of the exhaust gas at the inlet of the exhaust manifold, $T_{out\_manifold(k)}$ is the temperature of the exhaust gas at the outlet of the exhaust manifold for k^{th} cycle, $h_{gs\_manifold}$ is the convective hear transfer between exhaust gas and the body of the exhaust manifold for k^{th} cycle, $A_{i\_manifold}$ is the internal surface area of the exhaust manifold, $T_{g\_manifold(k)}$ is the average temperature of the exhaust gas inside the exhaust manifold for k^{th} cycle and $T_{m\_manifold(k)}$ is the temperature of the exhaust manifold body for the kth cycle. $H_{gs}.A_{i\_manifold}$ is calibrated for various temperature to calibrate the model based on the experimental data. The value of C_{p_g} for the exhaust gas is assumed to be same as that of air that for the temperature.

44

It is assumed that the body temperature of the exhaust manifold is constant for one engine cycle with no thermal gradient along the flow of the exhaust gases. Also, for heat transfer from the exhaust gas to exhaust manifold, the gas temperature is assumed as the average of the inlet and outlet gas temperature.

$$T_{g\_manifold(k)} = \frac{T_{in\_manifold(k)} + T_{out\_manifold(k)}}{2} \qquad (19)$$

The conductive heat transfer in and out of the exhaust manifold body is negligible compared to the convective heat transfer. Also, the radiation heat transfer from the exhaust manifold is neglected as the model is mainly designed for cold start conditions. Figure 25 shows a schematic diagram of heat transfer to the wall of the exhaust manifold from the exhaust gas and from the wall of exhaust manifold to the surroundings.
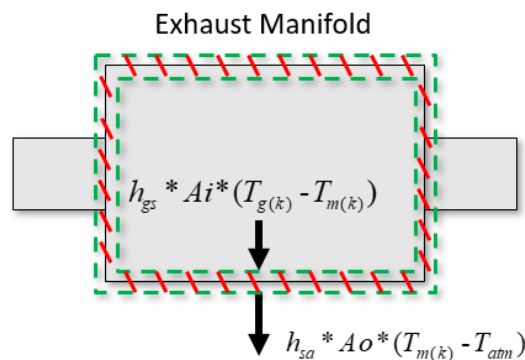
Figure 25: Schematic of heat transfer from the Exhaust Manifold to ambient

Again, applying first law of thermodynamics to exhaust manifold body for the heat transfers.

45

$$m_{m\_manifold} \cdot C_{p\_man} \cdot (\frac{dT_{m\_manifold}}{dt}) = h_{gs\_manifold} \cdot A_{i\_manifold} \cdot (T_{g\_manifold} - T_{m\_manifold}) -$$
$$h_{sa\_manifold} \cdot A_{o\_manifold} \cdot (T_{m\_manifold} - T_{atm})$$

(20)

Where, $m_{m\_manifold}$ is the mass of exhaust manifold, C_{p_man} heat capacity of the exhaust manifold, $T_{m\_manifold}$ is the temperature of the exhaust manifold, $h_{sa\_manifold}$ is the convective heat transfer coefficient between the exhaust manifold body with surrounding, $A_{o\_manifold}$ is exhaust manifold outer surface area and T_{atm} is the ambient temperature. The subscript manifold stands for exhaust manifold. $h_{gs\_manifold}.A_{i\_manifold}$ and $h_{sa\_manifold}.A_{o\_manifold}$ are calibrated to calibrate the model.

The rise in temperature of the exhaust manifold is computed on a cycle basis. The time interval between two cycles is calculated using engine speed. Therefore, the equation can be re-written as follows. $T_{m\_manifold(k+1)}$ is used as the temperature of the exhaust manifold for the next cycle. The subscript k refers to k^{th} cycle and $k+1$ refers to the next cycle of the kth cycle.

$$m_{m\_manifold} \cdot C_{p\_man} \cdot (\frac{T_{m\_manifold(k+1)} - T_{m\_manifold(k)}}{t_{k+1} - t_k}) = h_{gs\_manifold} \cdot A_{i\_manifold} \cdot (T_{g\_manifold(k)} - T_{m\_manifold(k)})$$
$$-h_{sa\_manifold} \cdot A_{o\_manifold} \cdot (T_{m\_manifold(k)} - T_{atm})$$

(21)

4.2.4 Turbocharger Thermal Model

Turbocharger thermal model incorporates the connecting pipe connecting the exhaust manifold and turbocharger. Here, as the modeling is done for cold start condition, turbocharger is considered as thermal mass and the work produced is neglected. The

46

turbocharger model estimated the temperature of the exhaust gas at the outlet of the turbocharger as a function of temperature at the inlet of the turbocharger. Similar to the exhaust thermal model the equations used for turbocharger model are as follows.

$$\dot{m}_{g(k)} \cdot C_{p\_g} \cdot (T_{in\_turbo(k)} - T_{out\_turbo(k)}) = h_{gs\_turbo} \cdot A_{i\_turbo} \cdot (T_{g\_turbo(k)} - T_{m\_turbo(k)})$$

(22)

Where, $T_{in\_turbo(k)}$ is the temperature of the exhaust gas at the inlet of the turbocharger for k^{th} cycle, $T_{out\_turbo(k)}$ is the temperature of the exhaust gas at the outlet of the turbocharger for k^{th} cycle, h_{gs_turbo} is the convective heat transfer coefficient between exhaust gas and the body of the turbocharger, A_{i_turbo} is the inner surface area of the turbocharger, $T_{g\_turbo(k)}$ is the average temperature of the exhaust gas inside the turbocharger and $T_{m\_turbo(k)}$ is the temperature of the turbocharger for k^{th} cycle.

Again, similar to the exhaust manifold model, the gas temperature inside the turbocharger is estimated as the average of inlet and outlet temperature of the gas.

$$T_{g\_turbo(k)} = \frac{T_{in\_turbo(k)} + T_{out\_turbo(k)}}{2}$$

(23)

The temperature rise of the turbocharger is calculated for the next cycle.

$$m_{m\_turbo} \cdot C_{p\_turbo} \cdot (\frac{dT_{m\_turbo}}{dt}) = h_{gs\_turbo} \cdot A_{i\_turbo} \cdot (T_{g\_turbo} - T_{m\_turbo})$$
$$-h_{sa\_turbo} \cdot A_{o\_turbo} \cdot (T_{m\_turbo} - T_{atm})$$

(24)

Where, m_{m_turbo} is the mass of turbocharger, C_{p_turbo} heat capacity of the turbocharger, $T_{m\_manifold}$ is the temperature of the turbocharger, h_{sa_turbo} is the convective heat transfer coefficient between the turbocharger body with surrounding, A_{o_turbo} is turbocharger outer surface area and T_{atm} is the ambient temperature. The subscript turbo stands for turbocharger. $H_{gs\_turbo}.A_{i\_turbo}$ and $h_{as\_turbo}.A_{o\_turbo}$ are calibrated to calibrate the model.

4.2.5 Catalyst Thermal Model

Unlike exhaust manifold and turbocharger model, catalyst model is modeled as a temperature gradient model. The catalyst model estimates the temperature of the outlet gas temperature and the catalyst body temperature as a function of temperature of the exhaust gases at the inlet of the catalyst. The catalyst is divided into several sections as desired and temperature gradient of the catalyst can be estimated. The radial heat gradient is neglected. Also, the heat generated due to the exothermic reactions inside the catalyst is neglected.

48
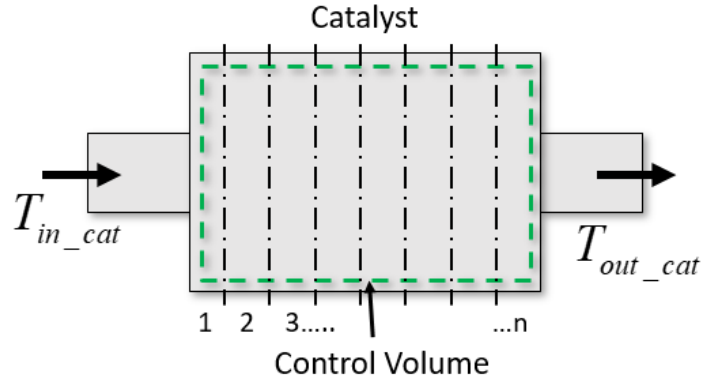
Figure 26: Schematic of Catalyst

Figure 26 shows a schematic of the Catalyst. The catalyst is divided into *n* number of parts for better accuracy in the calculations. The dotted green line represents the control volume for the catalyst which is divided by the vertical dotted black lines. The equation used for heat transfer between the exhaust gases and the catalyst body is as follows.

$$\dot{m}_g \cdot C_{p\_g} \cdot (T_{in\_cat(k,n)} - T_{out\_cat(k,n)}) = h_{gs\_cat} \cdot A_{i\_cat} \cdot (T_{g\_cat(k,n)} - T_{m\_cat(k,n)})$$

(25)

Here $T_{in\_cat(k,n)}$, $T_{out\_cat(k,n)}$, $T_{g(k,n)}$ and $T_{m\_cat(k,n)}$ is the temperature of exhaust gases at the inlet, temperature of the exhaust gases at the outlet, temperature of the exhaust gases inside the catalyst and temperature of the catalyst of the division *n*. $T_{g\_cat(k,n)}$ can be approximated by the following equation.

$$T_{g\_cat(k)} = \frac{T_{in\_cat(k)} + T_{out\_cat(k)}}{2}$$

(26)

The temperature at the outlet of the element is used as the temperature of the inlet of the next element as shown in equation (27).

49

$$T_{in\_cat(k,n+1)} = T_{out\_cat(k,n)} \qquad (27)$$

As the catalyst is divided into *n* divisions, there would conductive heat transfer between the elements.
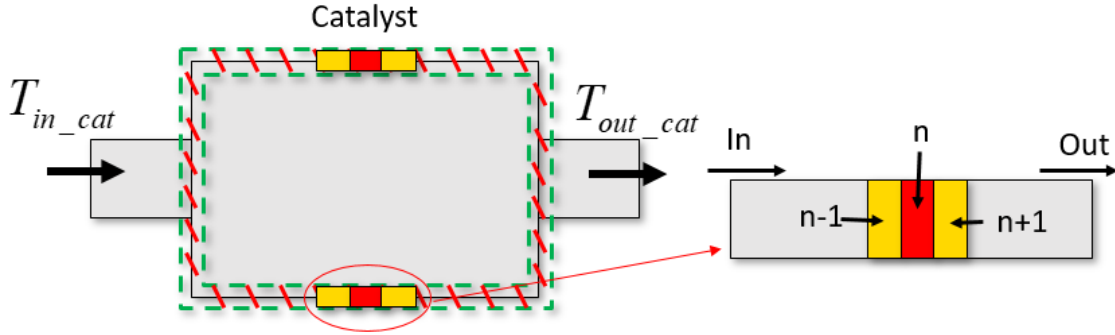
Figure 27: Schematic of division of Catalyst

As the catalyst is divided into *n* number of elements, heat transfer from the neighboring element is to be considered. A schematic of the same is shown in Figure 27. *n-1* is the preceding neighboring element and *n+1* is the succeeding neighboring element.

$$m_{m\_cat,n} \cdot C_{p\_cat} \cdot \left(\frac{T_{m\_cat(k+1,n)} - T_{m\_cat(k,n)}}{t_{k+1} - t_k}\right) = h_{gs\_cat} \cdot A_{i\_cat} \cdot (T_{g\_cat(k,n)} - T_{m\_cat(k,n)})$$

$$-h_{sa\_cat} \cdot A_{o\_cat} * (T_{m\_cat(k,n)} - T_{atm}) + \frac{K \cdot A_{cross}}{x} \cdot (T_{m\_cat(k,n-1)} - T_{m\_cat(k,n)})$$

$$-\frac{K \cdot A_{cross}}{x} \cdot (T_{m\_cat(k,n)} - T_{m\_cat(k-1,n+1)})$$

$$(28)$$

Where, $m_{m\_cat,n}$ is the mass of the catalyst per element, C_{p_cat} is the heat capacity of the catalyst, T_{m_cat} is the temperature of the catalyst, h_{gs_cat} is the coefficient of convective heat transfer between exhaust gas and catalyst, A_{i_cat} is the internal surface area in contact with the exhaust gas, h_{as_cat} is the coefficient of convective heat transfer between

50

the catalyst and surroundings, A_{o_cat} is the outer surface area of the catalyst, A_{cross} is the cross sectional area of the catalyst , K is the thermal conductivity of the catalyst and x is the center to center distance between two adjacent elements.

A schematic of the equation (28) for an element is shown in Figure 28. The arrows pointing toward the element are the heat addition to the element and the ones pointing away from the element are the heat loss from the element.

$$h_{gs} * A\,i * (T_{g\_cat(k,n)} - T_{m\_cat(k,n)})$$

$$\frac{K * A_{cross}}{x}(T_{m\_cat(k,n-1)} - T_{m\_cat(k,n)})$$

$$\frac{K * A_{cross}}{x}(T_{m\_cat(k,n)} - T_{m\_cat(k-1,n+1)})$$

$$h_{sa} * A\,o * (T_{m\_cat(k,n)} - T_{atm})$$
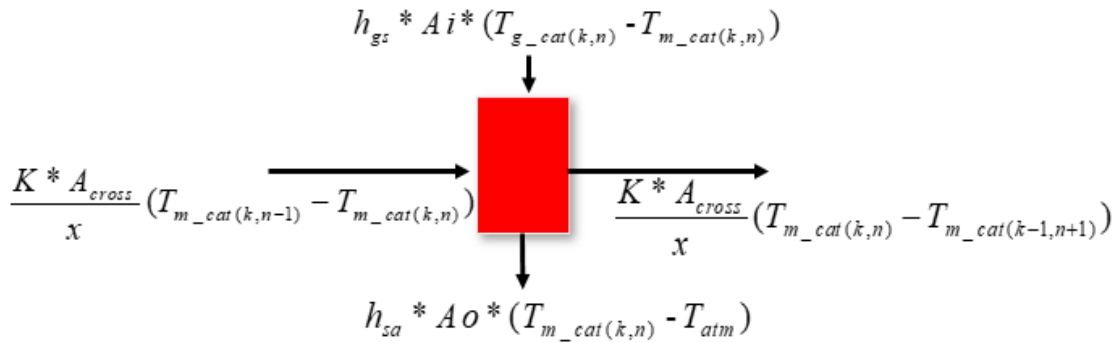
Figure 28: Schematic of Heat Transfer of a division of Catalyst

4.2.5.1 Vapor Condensation

Vapor condensation occurs when the air/ exhaust is a not able to sustain water vapor at the gas temperature as the gas temperature reduces due to convection to the catalyst and other components. The temperature at which first drop of dew is formed is called the dew point temperature. This dew point temperature is used to calculate the temperature of vapor condensation and mass of vapor condensed. Depending on the temperature, the capacity to hold vapor changes. Depending on the temperature of the exhaust gas at the

inlet on outlet of each division, mass of water vapor condensed is calculated. For E10 fuel, the red dot on the graph (Figure 29) shows the temperature where the condensation starts (326 K), and no condensation will occur if the temperature of the exhaust gas is above the red dot temperature.
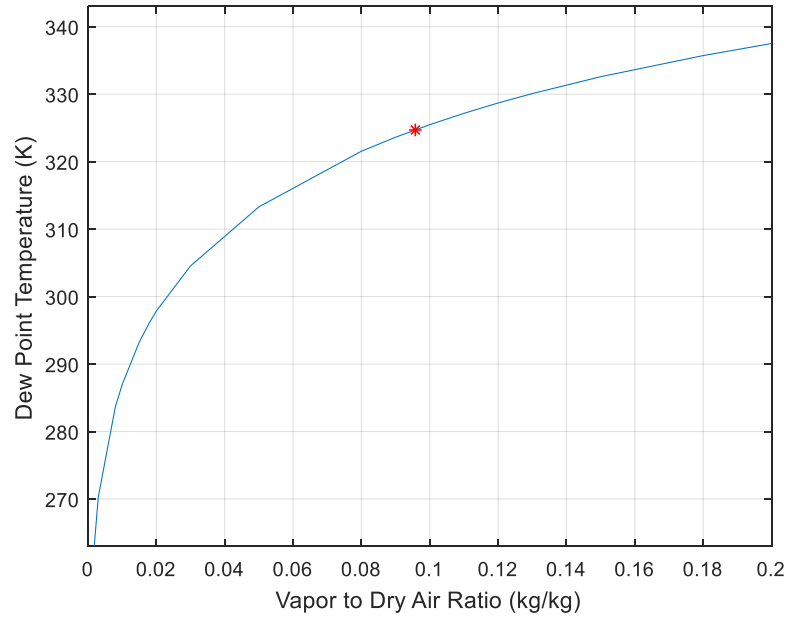
Figure 29: Mixing Ratio vs Dew Point Curve at 1 bar total pressure

Energy released due condensation is assumed to be transferred to the catalyst body and the equation used for heat transfer including vapor condensation is as follows.

$$m_{m\_cat,n} \cdot C_{p\_cat} \cdot \left(\frac{T_{cat(k+1,n)} - T_{cat(k,n)}}{t_{k+1} - t_k} \right) = h_{gs} \cdot Ai \cdot (T_{g\_cat(k,n)} - T_{m\_cat(k,n)}) - h_{sa} \cdot Ao \cdot (T_{m\_cat(k,n)} - T_{atm}) +$$

$$\frac{K \cdot A_{cross}}{x} \cdot (T_{m\_cat(k,n-1)} - T_{m\_cat(k,n)}) - \frac{K \cdot A_{cross}}{x} \cdot (T_{m\_cat(k,n)} - T_{m\_cat(k-1,n+1)}) + \dot{m}_{H2O\_cond} \cdot h_{fg\_cond}$$

(29)

$$\dot{m}_{H2O\_cond} * h_{fg} \qquad h_{gs} * Ai * (T_{g\_cat(k,n)} - T_{m\_cat(k,n)})$$

$$\frac{K * A_{cross}}{x}(T_{m\_cat(k,n-1)} - T_{m\_cat(k,n)}) \qquad \frac{K * A_{cross}}{x}(T_{m\_cat(k,n)} - T_{m\_cat(k-1,n+1)})$$

$$h_{sa} * Ao * (T_{m\_cat(k,n)} - T_{atm})$$
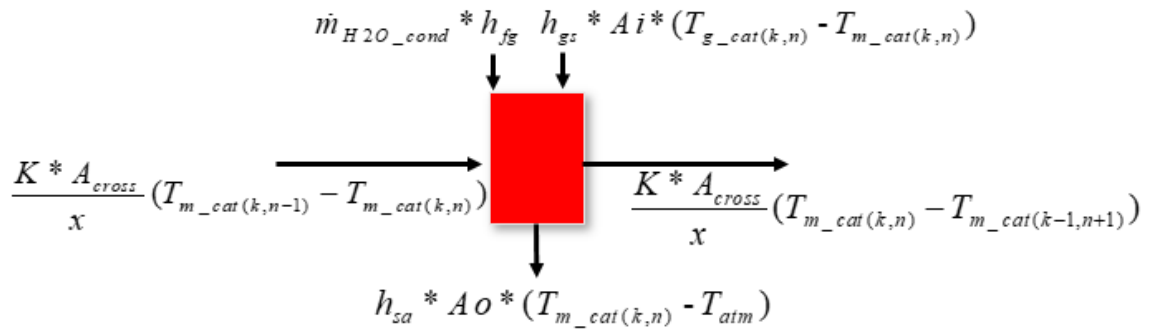
Figure 30: Schematic of Heat Transfer of a division of Catalyst with Vapor Condensation

Where, $\dot{m}_{H2O\_cond}$ is the mas of water vapor to be condensed converted into mass flow rate using engine speed, h_{fg_cond} is the heat of condensation at the temperature at which the condensation is occurring. The value of h_{fg_cond} is interpolated from the data curve shown in Figure 31. Figure 30 shows a schematic representation of equation (29) for an element of the catalyst.
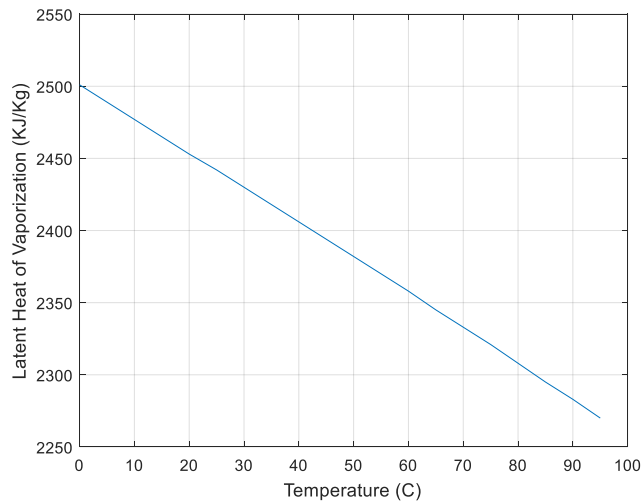
Figure 31: Latent Heat of Vaporization with Temperature

The amount of water condensed is stored in the same element of the catalyst where the vapor was condensed. This changes the mass flow rate of the exhaust gases.

53

$$\dot{m}_g = \dot{m}_g - \dot{m}_{H_2O\_cond} \qquad\qquad (30)$$

Where, $\dot{m}_g$ is the mass flow rate of exhaust gas and $\dot{m}_{H2O\_cond}$ is the mass of water vapor condensed converted to mass flow rate.

4.2.5.2 Re-evaporation of Condensed Water

Once the water vapor is condensed inside the catalyst, the condensed water will start to evaporate as the temperature of the exhaust gas and the catalyst body temperature start to increase. Also, the exhaust gases flowing through the catalyst, should have the capacity to hold water which would depend on the temperature of the catalyst and mixing ratio (mass of vapor divided by dry air mass). This capacity can be determined by using the dew point temperature correlation as shown in Figure 29. Depending on the vapor holding capacity, the amount of liquid water vaporized (m_{H2O_evap}) is determined. If condensed water mass is more than the capacity of the exhaust gases to hold vapor, the mass of water vaporized will be capacity of the exhaust gas until it saturates. Otherwise, if the vapor holding capacity of the exhaust gases is more than the liquid water, all the mass of liquid water will evaporate.

Two techniques of accommodating the heat transfer for the re-evaporation have been proposed. Using these techniques, the catalyst substrate temperature for next cycle is calculated.

Method 1

Once the amount of the condensed water inside the catalyst is known, temperature of the catalyst substrate is calculated using equation (29). If the mass to be evaporated is more than the capacity of holding vapor, equation (31) is used.

54

$$m_{m\_cat} \cdot C_{p\_cat} \cdot (T_{m\_cat(k+1,n)} - T_{m\_cat(k,n)}) = m_{m\_cat} \cdot C_{p\_cat} \cdot (T_{evap} - T_{cat(k,n)})$$
$$+ m_{H_2O\_evap} \cdot h_{fg\_evap}$$

(31)

Where, m_{H2O_evap} is the mass of water to be vaporized, T_{evap} is the temperature at which the water vapor evaporates, and h_{fg_evap} is the heat of vaporization of water at T_{evap}.

The above equation is derived considering the heat required to change the temperature of the catalyst if there was no re-evaporation would be same as the heat for increasing the temperature plus evaporation. As the mass of water to be evaporated is more than the capacity of the exhaust gas, the temperature of the catalyst would remain at T_{evap} until complete liquid water has been evaporated.

If the amount of condensed mass be less than the capacity of the exhaust gases to hold vapor, equation (32) is used.

$$m_{m\_cat} \cdot C_{p\_cat} \cdot (T_{m\_cat(k+1,n)} - T_{m\_cat(k,n)}) = m_{m\_cat} \cdot C_{p\_cat} \cdot (T_{evap} - T_{m\_cat(k,n)})$$
$$+ m_{H_2O\_evap} \cdot h_{fg\_evap} + m_{m\_cat} \cdot C_{p\_cat} \cdot (T'_{m\_cat(k+1,n)} - T_{evap})$$

(32)

$T'_{m\_cat(k+1,n)}$ would give the new catalyst substrate temperature for the next cycle.

Method 2

Once mass of water to be vaporized (m_{H2O_evap}) is known, depending on the mass of liquid water and vapor holding capacity, the temperature of the catalyst substrate is for the next cycle is calculated using equation (33).

55

$$m_{m\_cat} \cdot C_{p\_cat} \cdot \left(\frac{T_{cat(k+1,n)} - T_{cat(k,n)}}{t_{k+1} - t_k}\right) = h_{gs} \cdot A_{i\_cat} \cdot (T_{g\_cat(k,n)} - T_{m(k,n)}) - h_{sa} \cdot A_{o\_cat} \cdot (T_{m\_cat(k,n)} - T_{atm})$$

$$+ \frac{K \cdot A_{cross}}{x} \cdot (T_{m\_cat(k,n-1)} - T_{m\_cat(k,n)}) - \frac{K \cdot A_{cross}}{x} \cdot (T_{m\_cat(k,n)} - T_{m\_cat(k-1,n+1)}) + \dot{m}_{H2O\_cond} \cdot h_{fg\_cond}$$

$$- \dot{m}_{H2O\_evap} \cdot h_{fg\_evap}$$

$$(33)$$

Where, $\dot{m}_{H2O\_evap}$ is the mass of water to be vaporized converted to flow rate using engine speed. Figure 32 shows a schematic representation of the equation (33) for an element of the catalyst.
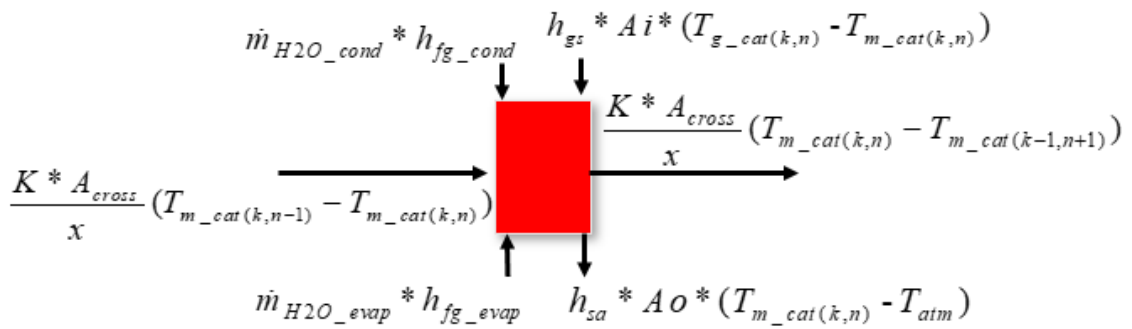
Figure 32: Schematic of heat transfer of a division of catalyst with vapor re-evaporation

Chapter 5

Correlations of Split Injection Parameters

In this section, correlations of combustion parameters including *CA50*, *CA00-10* and *CA10-90* with Start of first injection (*SOI*), End of second injection (*EOI*), Split Ratio (*SR*) and Spark Timing (*SA*) are given.
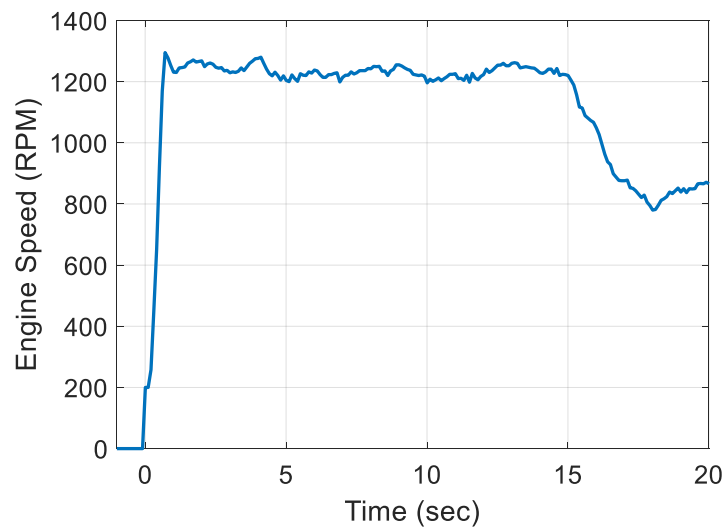
Figure 33: Engine Speed Curve during Cold Start

Figure 33 shows a typical engine speed curve during cold start of an engine. The initial phase during which the engine speed increases is called ramp up period. After ramp-up, comes the high speed idle where the engine speed is about 1250 RPM. High speed idle is used for faster heating of the catalyst. After the high speed idle, the engine goes to low speed idle where engine speed is around 800 RPM. The correlations for combustion parameters and exhaust gas temperature with split injection parameters are applicable for the high speed idle period during engine start up where the engine speed is around 1250 RPM. Thus, all the experiments done for correlations were at 1250 RPM.

The tests done are quasi-cold start meaning the engine oil was allowed to be cooled at 33°C and then with a preset throttle and spark time for the IMEP to be 250 *KPa*, engine was run at 1250 *RPM* and 1000 cycles were recorded from first cycle. All the parameters are calculated with two methods as discussed in Section 4.1.1. R^2 is a statistical measure of closely the regression fit matches with the experimental data. R^2 equal to 1 means perfect correlation and R^2 equal to zero means no correlation.

Root mean square error (RMSE) is also a statistical tool to measure of the error between the estimated and actual value. RMSE is calculated by the equation showed below.

$$RMSE = \sqrt{\frac{\sum_{t=1}^{n}(\hat{y}_t - y_t)^2}{n}}$$

(34)

Where, $\hat{y}$ is the predicted and y is the observed value for *n* different predictions. The unit of RMSE is same as the unit of the predicted or observed values.

5.1 CA50 correlation with Control Parameters

Method A

The correlation for *CA50* calculated using Method A is shown in equation (35). PolyE value is neglected and combustion parameters are calculated by just using PolyC values.

$$CA50 = 17.5 + 0.412 \cdot EOI + 0.0720 \cdot SOI + 71.4 \cdot SR - 0.126 \cdot SA + 0.00218 \cdot EOI \cdot SOI$$
$$- 0.000350 \cdot EOI \cdot SOI - 0.628 \cdot EOI \cdot SR + 0.00307 \cdot EOI \cdot SA - 0.1668 \cdot SOI \cdot SR$$
$$+ 0.00191 \cdot SOI \cdot SA + 2.409 \cdot SR \cdot SA$$

(35)

58
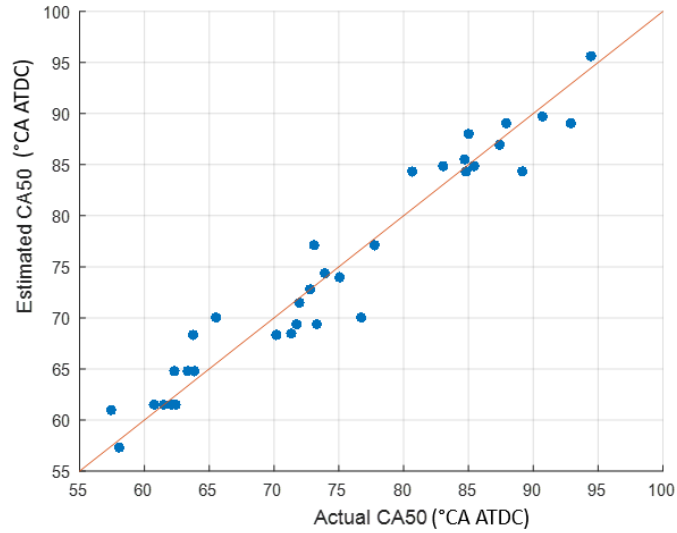
Figure 34: CA50 correlation fit using Method A

The R^2 for the correlation for *CA50* using Method A was found out to be 0.94 and *RMSE* to be 3.2°CA. The correlation for *CA50* consists of many terms as it can be seen from equation (35). Some of the terms are important for the correlation where as some of the terms are not significant. The significant terms could be found out using Pareto Chart. The Pareto Chart gives the significance of each independent variable and interaction variable for a dependent parameter. It can be observed that *SA*, *EOI* and *SR* are the important contributing factors towards CA50 correlation.
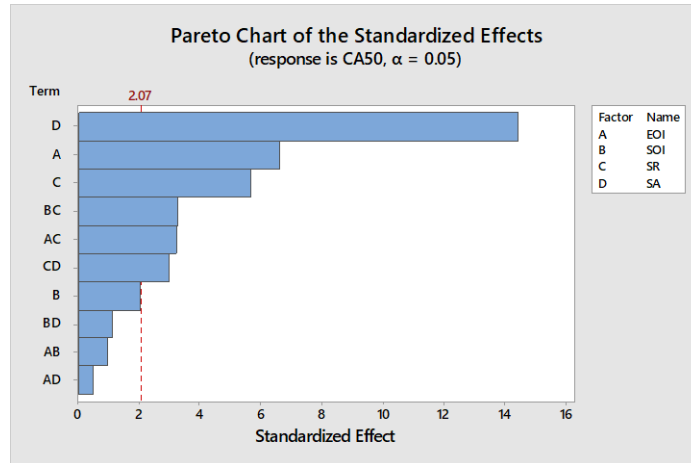
Figure 35: Pareto Chart for CA50 calculated using Method A for confidence interval of 95%

The Pareto Chart for *CA50* calculated using Method A is given in Figure 35. The vertical line shows significance reference for confidence interval of 95%. Using the Pareto Chart and correlation coefficients, a reduced model for *CA50* is developed as shown in the equation below.

$$CA50 = 34.3 + 0.511 \cdot EOI + 27.7 \cdot SR + 0.284 \cdot SA - 0.676 \cdot EOI \cdot SR + 2.34 \cdot SR \cdot SA$$

(36)

The R^2 for the reduced correlation for *CA50* using Method A was found out to be 0.88 and *RMSE* to be 4.2°CA. Figure 36 shows the comparison between actual *CA50* and the estimated *CA50* using the reduced correlation using Method A.
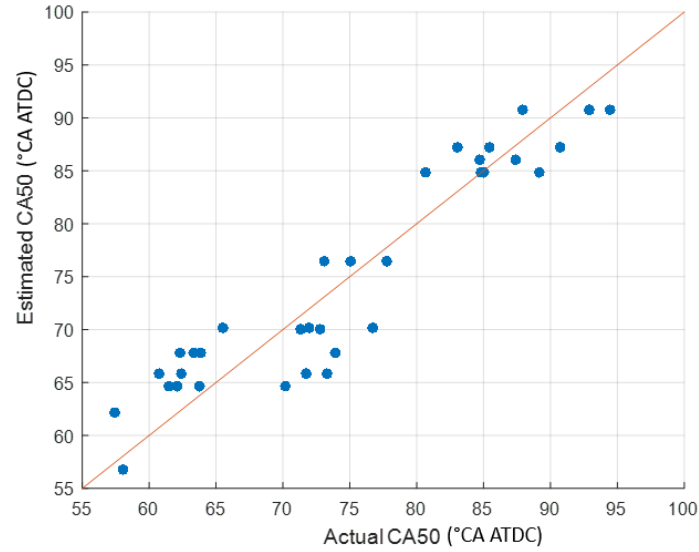
Figure 36: Reduced CA50 correlation using Method A

Method B

The correlation for *CA50* calculated using Method B is shown in equation (37). The combustion parameters are calculated by changing the interval for PolyE.

$$CA50 = 17.7 + 0.419 \cdot EOI + 0.0722 \cdot SOI + 71 \cdot SR - 0.164 \cdot SA + 0.00209 \cdot EOI \cdot SOI$$
$$- 0.000360 \cdot EOI \cdot SOI - 0.624 \cdot EOI \cdot SR + 0.00301 \cdot EOI \cdot SA - 0.1674 \cdot SOI \cdot SR$$
$$+ 0.00195 \cdot SOI \cdot SA + 2.463 \cdot SR \cdot SA$$

(37)

61
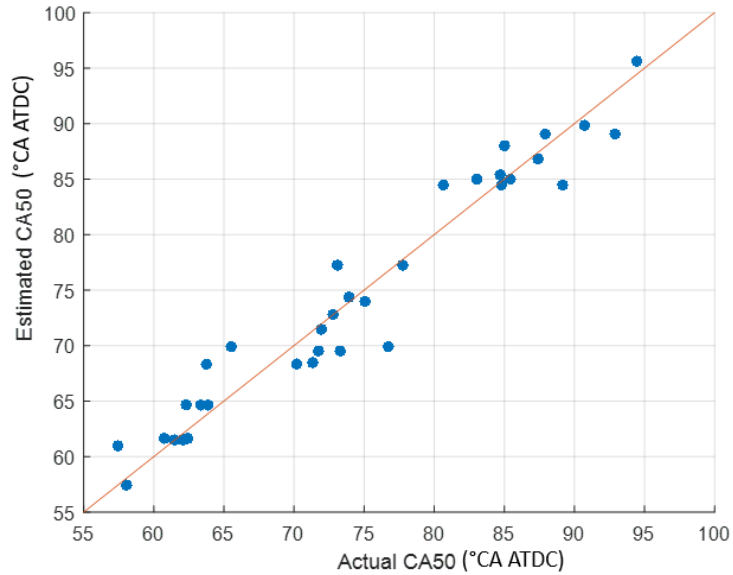
Figure 37: CA50 correlation fit using Method B

The R^2 for the correlation for *CA50* using Method B was found out to be 0.94 and *RMSE* to be 3.2°CA. Figure 37 shows a comparison between actual *CA50* and estimated *CA50* values. Similar exercise for reducing the correlation terms, as shown for Method A, was repeated for Method B. The Pareto Chart for CA50 correlation using Method B is shown in Figure 38. It can be observed that *SA*, *EOI* and *SR* are the important contributing factors towards CA50 correlation.

Using the Pareto Chart and correlation coefficients, a reduced model for *CA50* is developed as shown in the equation below.

$$CA50 = 34.8 + 0.507 \cdot EOI + 27.1 \cdot SR + 0.256 \cdot SA - 0.671 \cdot EOI \cdot SR + 2.39 \cdot SR \cdot SA \quad (38)$$
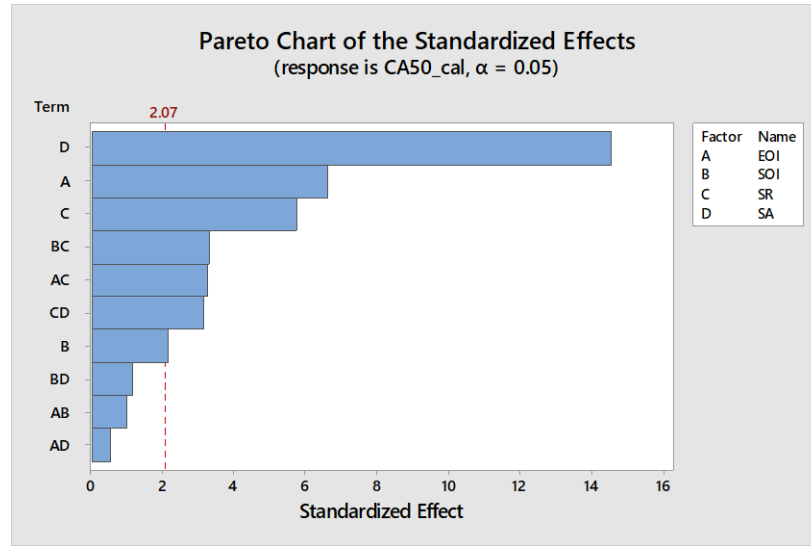
Figure 38: Pareto Chart for CA50 calculated using Method B for confidence interval of 95%

The R^2 for the reduced correlation for *CA50* using Method B was found out to be 0.87 and *RMSE* to be 4.2°CA. Figure 39 shows the comparison between actual *CA50* and the estimated *CA50* using the reduced correlation using Method B.
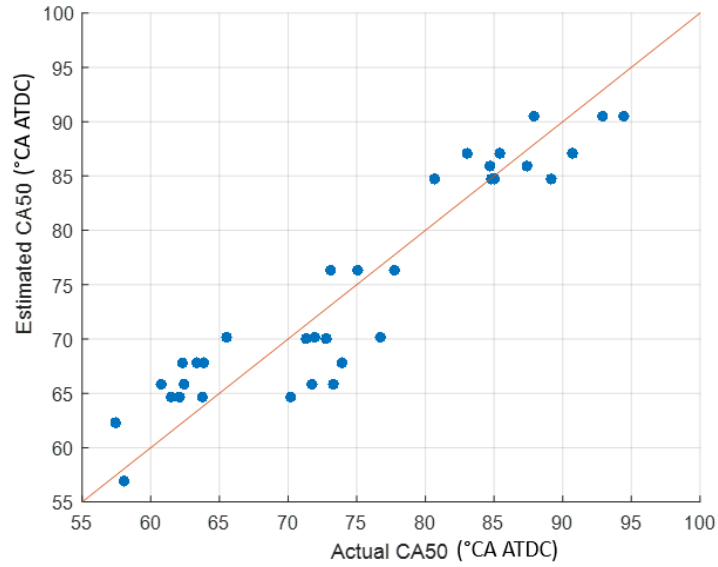
Figure 39: Reduced CA50 correlation fit using Method B

Comparison of Method A and Method B

A comparison of Method A and Method B is shown in Figure 40. It can be seen from the figure that *CA50* values calculated using Method A and *CA50* values calculated using Method B correlated very well with each other (R^2=1).

64
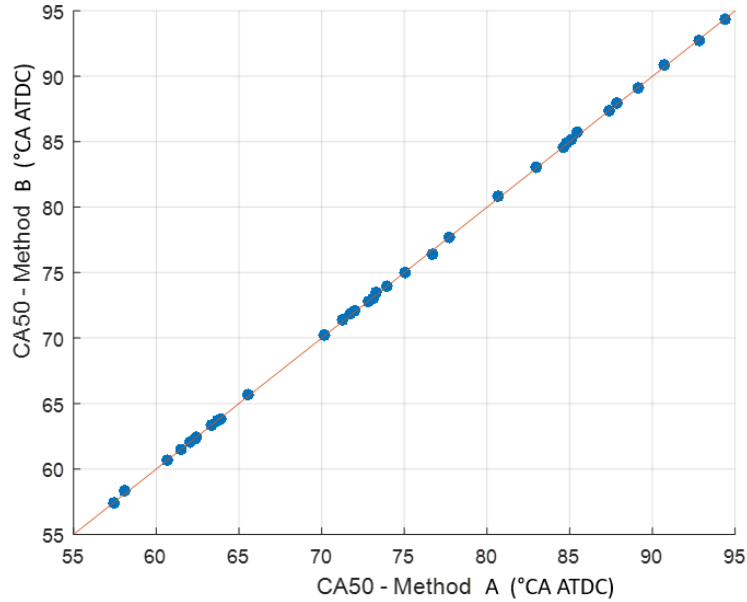
Figure 40: CA50 Comparison of Method A and Method B

5.2 CA10-90 correlation with Control Parameters

Method A

The correlation for *CA10-90* calculated using Method A is shown in equation (39). PolyE value is neglected and *CA10-90* values are calculated by just using PolyC values.

$$CA10-90 = 33.5 + 0.406 \cdot EOI + 0.0025 \cdot SOI + 54.7 \cdot SR + 1.196 \cdot SA + 0.00182 \cdot EOI \cdot EOI$$
$$+ 0.000149 \cdot EOI \cdot SOI - 0.456 \cdot EOI \cdot SR - 0.01632 \cdot EOI \cdot SA - 0.0359 \cdot SOI \cdot SR$$
$$+ 0.00099 \cdot SOI \cdot SA - 2.236 \cdot SR \cdot SA$$

(39)

65
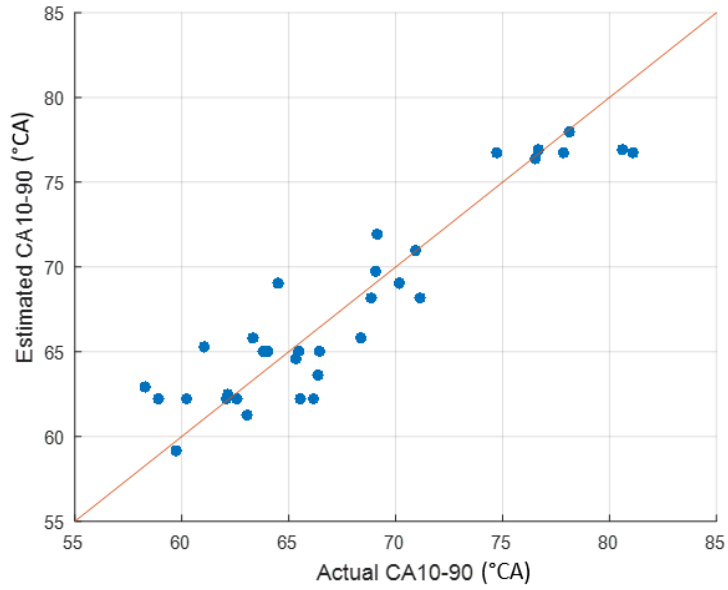
Figure 41: CA10-90 correlation fit using Method A

The R^2 for the correlation for CA10-90 using Method A was found out to be 0.85 and RMSE to be 2.8°CA. Figure 41 shows a comparison between actual CA10-90 and estimated CA10-90 values. Again, Pareto Chart is used to check the significance of each independent and interaction variable for *CA10-90* correlation. It can be observed that *SA* and *EOI* are the important contributing factors towards *CA10-90* correlation.

66
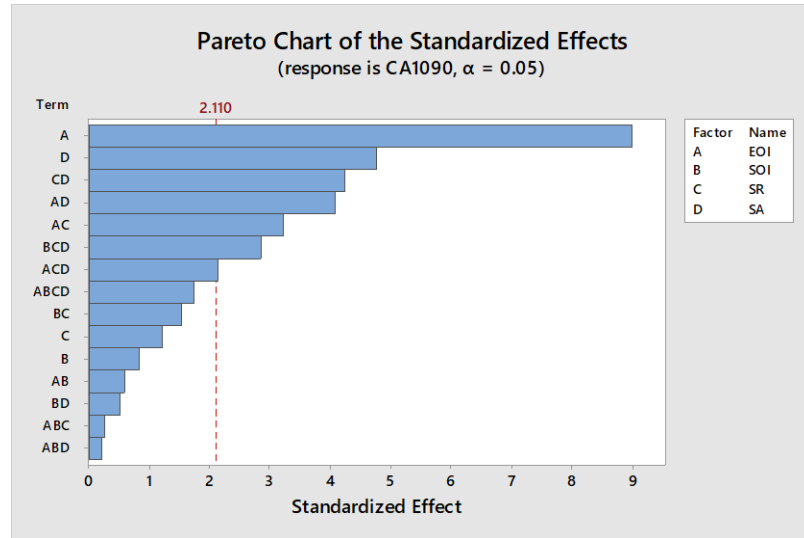
Figure 42: Pareto Chart for CA10-90 calculated using Method A for confidence interval of 95%

Using the Pareto Chart and correlation coefficients, a reduced model for *CA10-90* is reduced as shown in the equation below.

$$CA10-90 = 31.04 + 0.622 \cdot EOI + 45.5 \cdot SR + 1.417 \cdot SA - 0.477 \cdot EOI \cdot SR - 0.01612 \cdot EOI \cdot SA$$
$$-2.191 \cdot SR \cdot SA$$

(40)

The R^2 for the reduced correlation for *CA10-90* using Method B was found out to be 0.84 and *RMSE* to be 2.7°CA. Figure 43 shows the comparison between actual *CA10-90* and the estimated *CA10-90* using the reduced correlation using Method A.

67

Figure 43: Reduced CA10-90 correlation fit using Method A

Method B

The correlation for *CA10-90* calculated using Method B is shown in equation (41). The *CA10-90* values are calculated by changing the interval for PolyE.

$$CA10-90 = 32.6 + 0.474 \cdot EOI + 0.0036 \cdot SOI + 50.2 \cdot SR + 1.256 \cdot SA + 0.00028 \cdot EOI \cdot EOI$$
$$+ 0.000157 \cdot EOI \cdot SOI - 0.368 \cdot EOI \cdot SR - 0.01563 \cdot EOI \cdot SA - 0.0292 \cdot SOI \cdot SR$$
$$+ 0.00069 \cdot SOI \cdot SA - 2.248 \cdot SR \cdot SA$$

(41)

The R^2 for the correlation for *CA10-90* using Method B was found out to be 0.86 and *RMSE* to be 2.5°CA. Figure 44 shows a comparison between actual *CA10-90* and estimated *CA10-90* values.
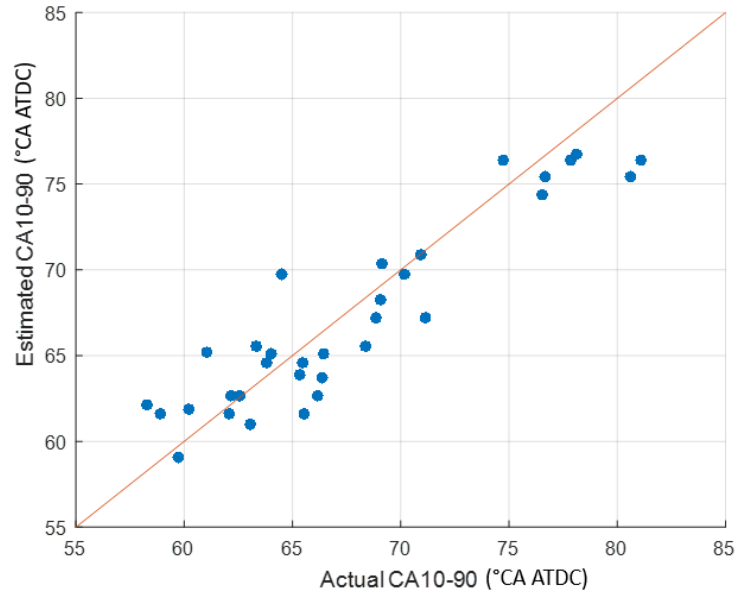
Figure 44: CA10-90 correlation fit using Method B

Similar exercise for reducing the correlation terms was repeated for Method B. The Pareto Chart for *CA10-90* correlation using Method B is shown in Figure 45. It can be observed that *SA* and *EOI* are the important contributing factors towards *CA10-90* correlation.

Figure 45: Pareto Chart for CA10-90 calculated using Method B for confidence interval of 95%

Using the Pareto Chart and correlation coefficients, a reduced correlation for *CA10-90* is developed as shown in the equation below.

$$CA10-90 = 32.99 + 0.5436 \cdot EOI + 42.7 \cdot SR + 1.438 \cdot SA - 0.372 \cdot EOI \cdot SR$$
$$-0.01550 \cdot EOI \cdot SA - 2.256 \cdot SR \cdot SA$$

(42)

The R^2 for the reduced correlation for *CA10-90* using Method B was found out to be 0.86 and *RMSE* to be 2.3°CA. Figure 46 shows the comparison between actual *CA10-90* and the estimated *CA10-90* using the reduced correlation using Method B.
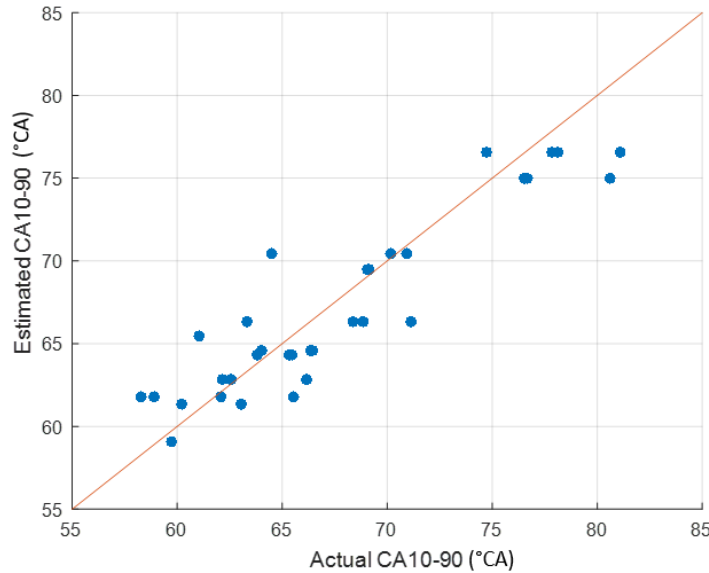
Figure 46: Reduced CA10-90 correlation fit using Method B

Comparison of Method A and Method B

A comparison of Method A and Method B is shown in Figure 47. It can be seen from the figure that *CA10-90* values calculated using Method A and *CA10-90* values calculated using Method B correlated very well with each other (R^2=0.99).

70
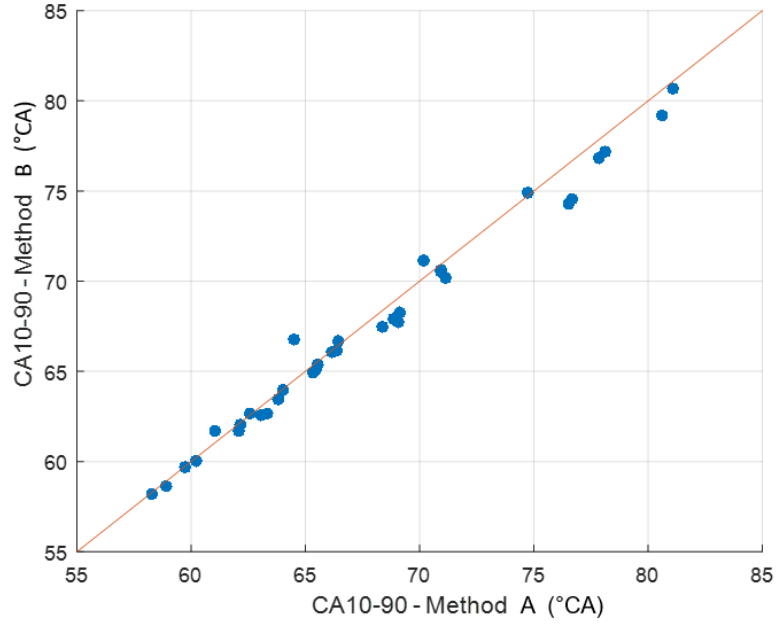
Figure 47: CA10-90 Comparison of Method A and Method B

5.3 CA00-10 correlation with Control Parameters

Method A

The correlation for *CA00-10* calculated using Method A is shown in equation (43). PolyE value is neglected and *CA00-10* values are calculated by just using PolyC values.

$$
\begin{aligned}
CA00-10 &= 4.1 + 0.161 \cdot EOI + 0.0637 \cdot SOI + 50.8 \cdot SR - 0.690 \cdot SA + 0.00135 \cdot EOI \cdot EOI \\
&+ 0.000036 \cdot EOI \cdot SOI - 0.414 \cdot EOI \cdot SR + 0.00336 \cdot EOI \cdot SA - 0.1351 \cdot SOI \cdot SR + \\
&0.00010 \cdot SOI \cdot SA + 2.120 \cdot SR \cdot SA
\end{aligned}
$$

(43)

71

The R^2 for the correlation for *CA00-10* using Method A was found out to be 0.88 and RMSE to be 2.2°CA. Figure 48 shows a comparison between actual *CA00-10* and estimated *CA00-10* values.
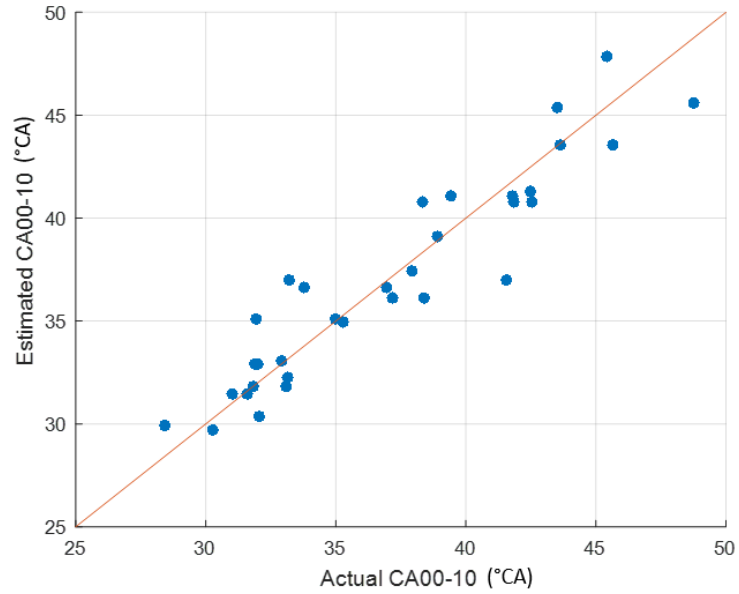
Figure 48: CA00-10 correlation fit using Method A

Again, Pareto Chart is used to check the significance of each independent and interaction variable for *CA00-10* correlation (Figure 49). It can be observed that *SA, SR* and *EOI* are the important contributing factors towards *CA00-10*correlation.
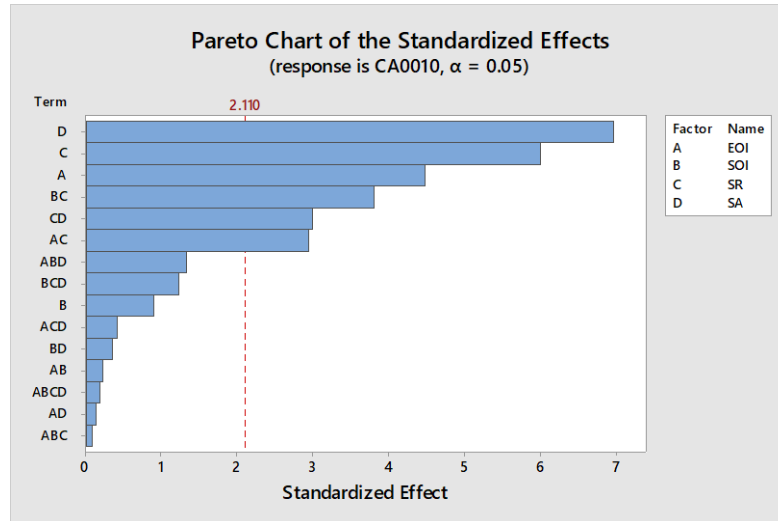
Figure 49: Pareto Chart for CA00-10 calculated using Method A for confidence interval of 95%

Using the Pareto Chart and correlation coefficients, a reduced correlation for *CA00-10* is developed as shown in the equation below.

$$CA00-10 = 19.76 + 0.288 \cdot EOI + 15.0 \cdot SR - 0.707 \cdot SA - 0.432 \cdot EOI \cdot SR + 0.00476 \cdot EOI \cdot SA + 2.008 \cdot SR \cdot SA$$

(44)

The R^2 for the reduced correlation for *CA00-10* using Method A was found out to be 0.75 and *RMSE* to be 2.9°CA. Figure 50 shows the comparison between actual *CA00-10* and the estimated *CA00-10* using the reduced correlation using Method A.
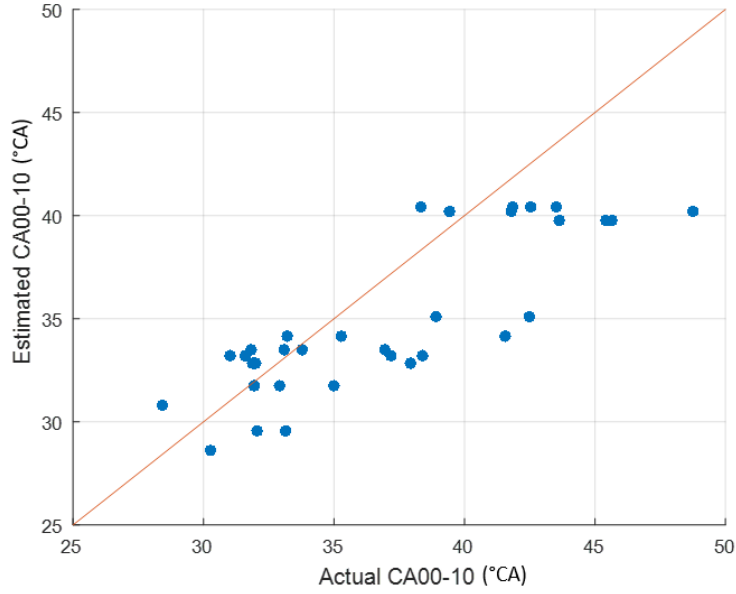
Figure 50: Reduced CA00-10 correlation fit using Method A

Method B

The correlation for *CA00-10* calculated using Method B is shown in equation (45). The *CA00-10* values are calculated by changing the interval for PolyE.

$$CA00-10 = 4.6 + 0.167 \cdot EOI + 0.0622 \cdot SOI + 49.4 \cdot SR - 0.675 \cdot SA + 0.00117 \cdot EOI \cdot EOI$$
$$+ 0.00004 \cdot EOI \cdot SOI - 0.403 \cdot EOI \cdot SR + 0.00335 \cdot EOI \cdot SA - 0.1317 \cdot SOI \cdot SR$$
$$+ 0.00003 \cdot SOI \cdot SA + 2.126 \cdot SR \cdot SA$$

(45)

The *R²* for the correlation for *CA00-10* using Method B was found out to be 0.88 and *RMSE* to be 2.2°CA. Figure 51 shows a comparison between actual *CA00-10* and estimated *CA00-10* values.

74
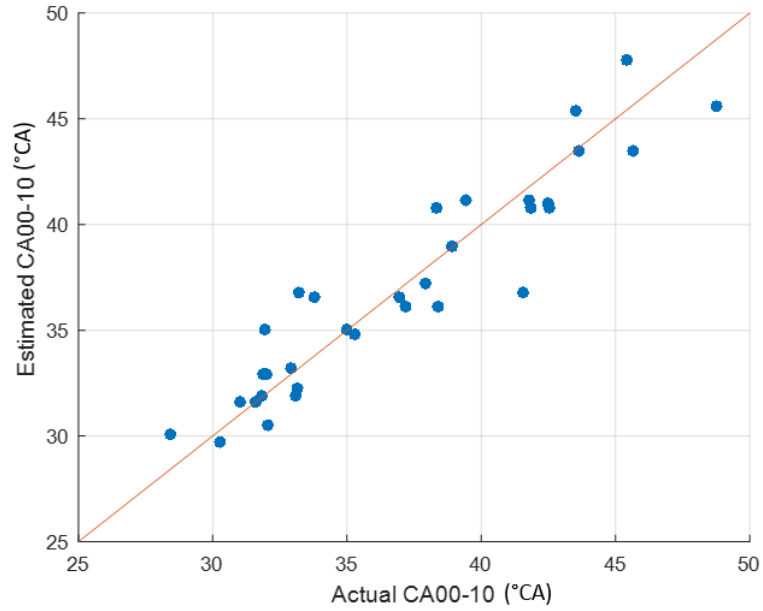
Figure 51: CA00-10 correlation fit using Method B
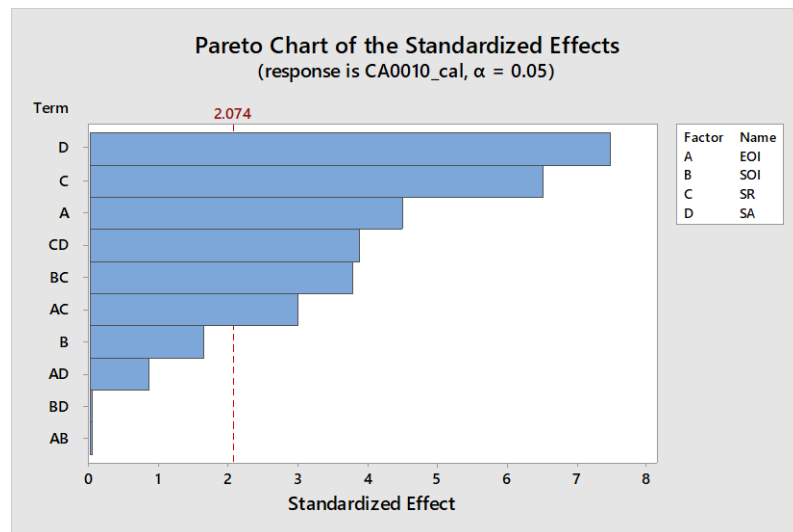
Figure 52: Pareto Chart for CA00-10 calculated using Method B for confidence interval of 95%

Similar exercise for reducing the correlation terms was repeated for Method B. The Pareto Chart for *CA10-90* correlation using Method B is shown in Figure 52. It can be observed

75

that *SA, SR* and *EOI* are the important contributing factors towards *CA00-10* correlation. Using the Pareto Chart and correlation coefficients, a reduced correlation for *CA00-10* is developed as shown in the equation below.

$$CA00-10 = 20.08 + 0.277 \cdot EOI + 14.5 \cdot SR - 0.706 \cdot SA - 0.419 \cdot EOI \cdot SR + 0.00474 \cdot EOI \cdot SA$$
$$+ 2.005 \cdot SR \cdot SA$$

(46)

The R^2 for the reduced correlation for *CA00-10* using Method B was found out to be 0.75 and *RMSE* to be 2.8CA. Figure 46 shows the comparison between actual *CA00-10* and the estimated *CA00-10* using the reduced correlation using Method B.
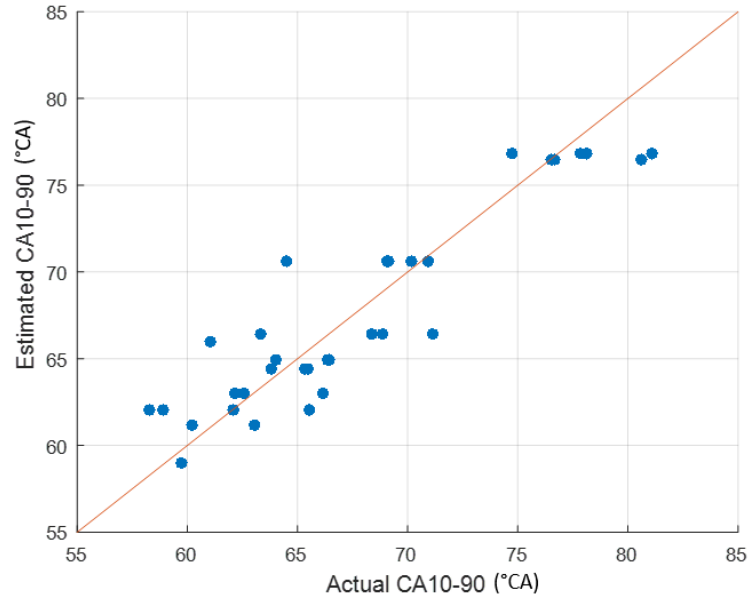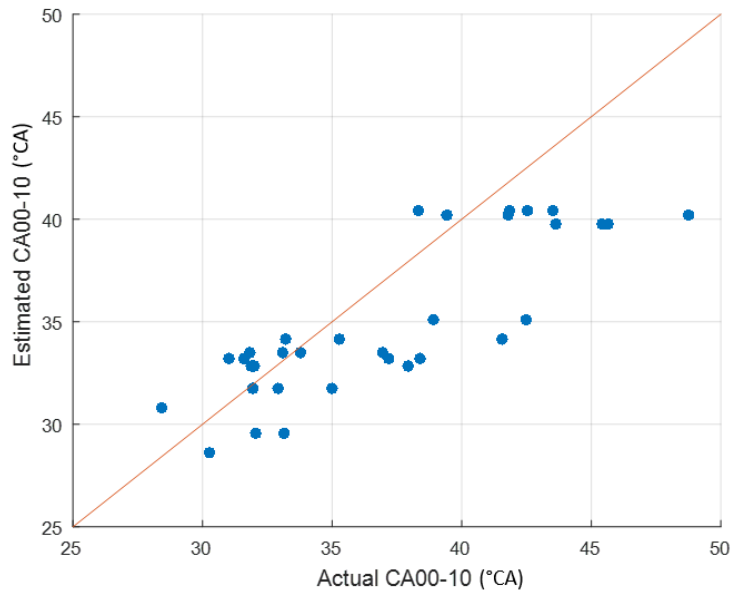

Figure 53: Reduced CA00-10 correlation fit using Method B

Comparison of Method A and Method B

76

A comparison of Method A and Method B is shown in Figure 54. It can be seen from the figure that *CA10-90* values calculated using Method A and *CA10-90* values calculated using Method B correlated very well with each other (R^2=0.99).
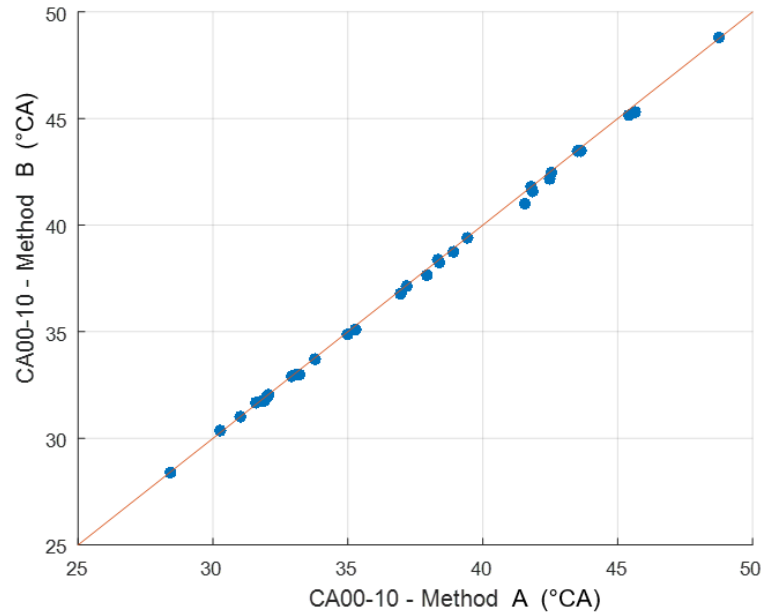
Figure 54: CA00-10 Comparison of Method A and Method B

5.4 Exhaust Gas Temperature Correlation

The correlation for the average of exhaust gas temperature is made considering the *CA50* values as well. As seen from Figure 40 the *CA50* values are same for Method A and Method B, thus, doesn't matter which values are taken for the correlation. The correlation for average of 800 cycles for all the tests done is given below.

77

$$T_{exh} = 96 - 10.89 \cdot EOI + 1.086 \cdot SOI - 500 \cdot SR - 89.6 \cdot SA + 41.6 \cdot CA50 - 0.015 \cdot EOI \cdot EOI$$
$$- 0.366 \cdot CA50 \cdot CA50 + 0.00871 \cdot EOI \cdot SOI - 1.94 \cdot EOI \cdot SR - 0.267 \cdot EOI \cdot SA$$
$$+ 0.1871 \cdot EOI \cdot CA50 + 0.234 \cdot SOI \cdot SR + 0.0495 \cdot SOI \cdot SA - 0.0289 \cdot SOI \cdot CA50$$
$$+ 30.1 \cdot SR \cdot SA + 2.3 \cdot SR \cdot CA50 + 1.149 \cdot SA \cdot CA50$$

$$(47)$$

The R^2 for the correlation for T_{exh} was found to be 0.96 and *RMSE* to be 22°C. Figure 51 shows a comparison between actual T_{exh} and estimated T_{exh} values.
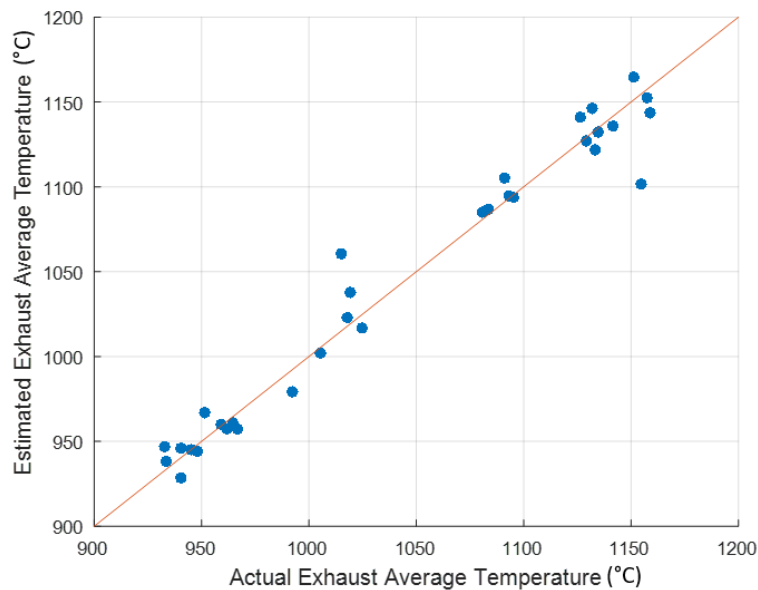
Figure 55: Exhaust Temperature correlation fit

Similar exercise of generating Pareto Chart is done to see the significance of each term for reducing the number of terms in the correlation. For the average of the exhaust gas temperature, from Figure 56, it can be seen that Spark Advance is the main contributor whereas, split ratio is the least contributor towards the correlation.
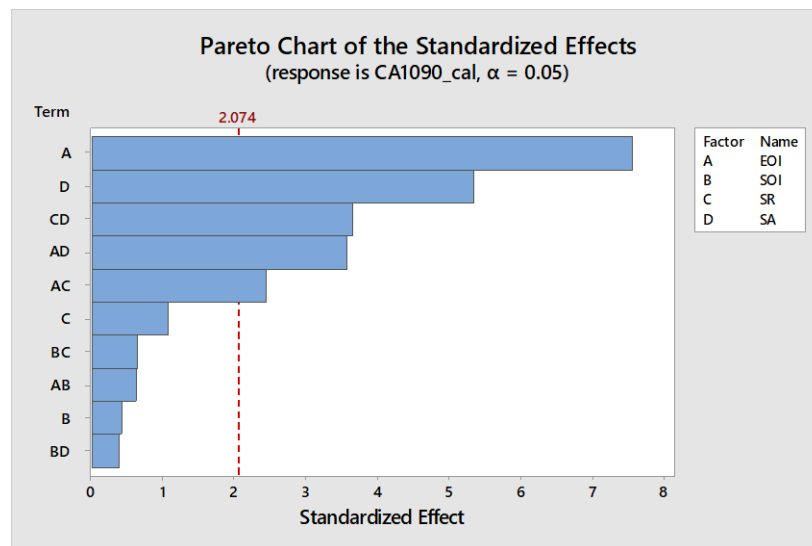
78
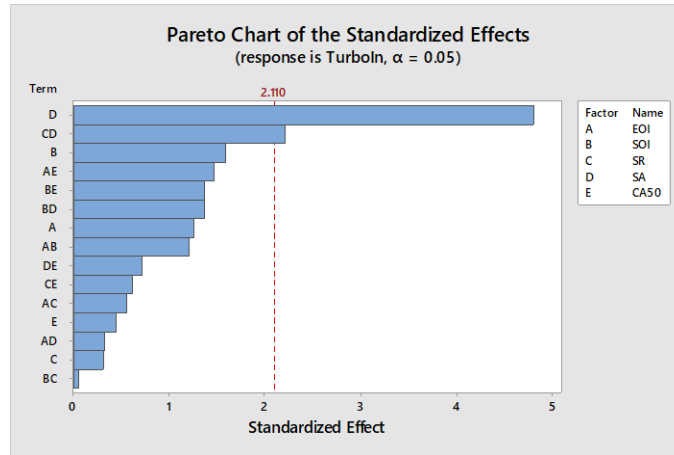
Figure 56: Pareto Chart for Exhaust Gas Temperature for confidence interval of 95%

Using the Pareto Chart and correlation coefficients, a reduced correlation for T_{exh} is shown in the equation below.

$$T_{exh} = 888 - 162 \cdot SR - 5.12 \cdot SA + 3.54 \cdot CA50 + 28.6 \cdot SR \cdot SA - 2.88 \cdot SR \cdot CA50$$

(48)

The R^2 for the reduced correlation for T_{exh} using Method B was found out to be 0.92 and *RMSE* to be 25°C. Figure 57 shows the comparison between actual T_{exh} and the estimated T_{exh} using the reduced correlation.

In Figure 57, an outlier can be seen which do not follow the reduced correlation. The deviation for that point for high level correlation is 45°C. The deviation increases to 120°C when the correlation terms are reduced.
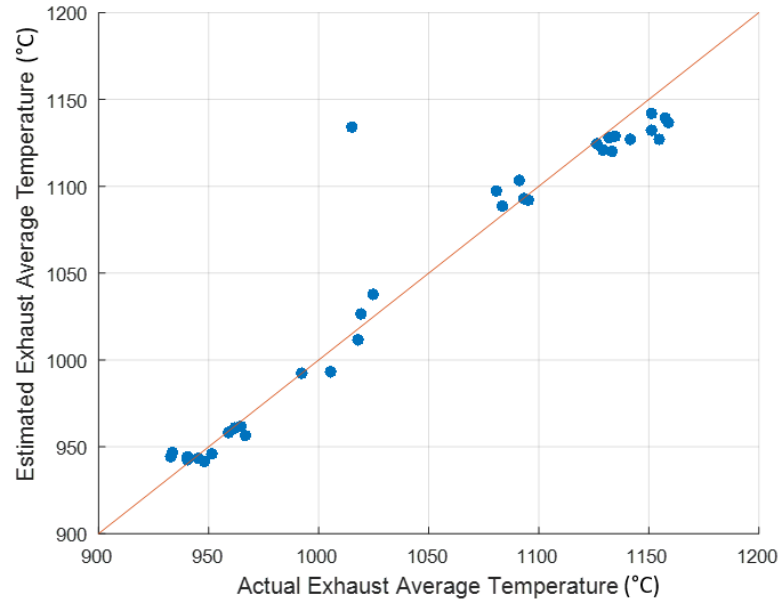
Figure 57: Reduced Exhaust Temperature correlation fit

80

5.5 Summary of Correlations

A summary of the correlations with R^2, *RMSE* and the major contributing factors for the correlation is shown in Table 6. All the R^2 values are more than 0.80 except for reduced correlation for *CA00-10*.

Table 6: Summary of R^2 and RMSE for High Level and Reduced Correlations

			R^2		RMSE		Major Contributing Factors
			Method A	Method B	Method A	Method B	
High Level Correlation		CA50	0.94	0.94	3.2 (°CA)	3.2 (°CA)	SA, EOI, SR
		CA10-90	0.85	0.86	2.8 (°CA)	2.5 (°CA)	SA, SR, EOI
		CA00-10	0.88	0.88	2.2 (°CA)	2.2 (°CA)	EOI, SA
		T_{exh}	0.96		22 (°C)		SA
Reduced Correlation		CA50	0.88	0.88	4.2 (°CA)	4.2 (°CA)	SA, EOI, SR
		CA10-90	0.84	0.86	2.7 (°CA)	2.3 (°CA)	SA, SR, EOI
		CA00-10	0.75	0.76	2.9 (°CA)	2.8 (°CA)	EOI, SA
		T_{exh}	0.92		25 (°C)		SA

Exhaust Thermal Model

The exhaust thermal model had to be calibrated. As discussed earlier, the test procedure followed for data collection was by letting the engine cool down to the room temperature and start the engine with constant throttle angle to produces around 2.5 bar *IMEP* at 1250 *RPM* as shown in Figure 58. It can be observed that *IMEP* values come close to 2.5 bar after about 100 cycles. The idea was to keep the *IMEP* and mass flow rate steady. All other engine controlling parameters were set to auto mode.
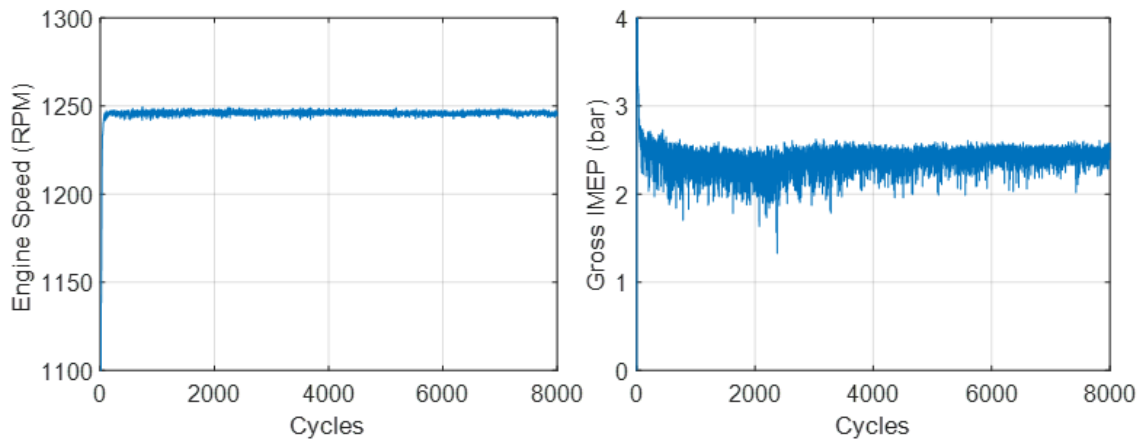
Figure 58: Engine Speed and IMEP for first 8000 cycles

5.6 Exhaust Manifold Model

The exhaust manifold is modeled as a lumped system. It estimates the exhaust manifold temperature as a function of exhaust manifold inlet temperature. The estimated exhaust manifold outlet temperature is compared with the measured values thermocouple located at the outlet of the exhaust manifold. The convective heat transfer coefficient is calibrated to match the estimated and measured values.

82
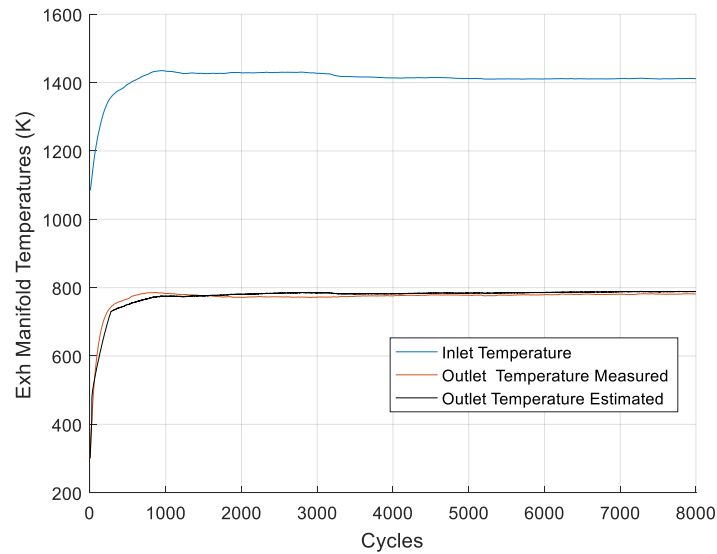
Figure 59: Comparison of Measured and Estimated Exhaust Manifold Outlet Temperature

The exhaust manifold body temperature can also be compared to measured values by the thermocouple mounted on the end of exhaust manifold. As this is modeled as lumped model, the temperature of the entire exhaust manifold is considered to be same for an instance i.e. no thermal gradient is considered. Figure 59 shows a comparison between estimated and measured exhaust gas temperature at the outlet of the exhaust manifold. The exhaust manifold inlet temperature is the average value of measured valued form the thermocouples measuring exhaust gas temperature near the exhaust valve. The measured temperature at the exhaust valve is usually lower than the temperature measured at the outlet of the exhaust manifold. This happens mainly because of two reasons as below.

1. The comparatively cooler oil flowing through the jackets nearby exhaust manifold to cool down the engine block affects the temperature measured by the thermocouple.

83

2. The thermocouple is not exposed to steady flow of exhaust gas at the valve. Thus, the measured value by the thermocouple will be the temperature maintained by both convective and radiation heat transfer.

Therefore, to deal with such situation, a constant of 200°C is added to the average values of the thermocouple measurement at the exhaust valve. The exhaust manifold inlet temperature is expected to be replaced by the engine exhaust temperature values form the Air Charge model.
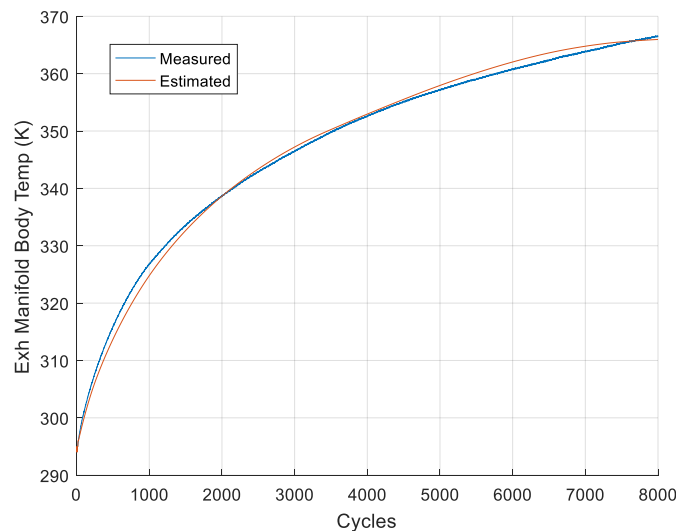
Figure 60: Comparison of Measured and Estimated Exhaust Manifold Body Temperature

A comparison between exhaust manifold measured and estimated body temperature is shown in Figure 60. Although, the exhaust gas temperature at the outlet of the exhaust manifold seems to reach a steady value, the exhaust manifold seems to increase even after first 8000 cycles.

84

5.7 Turbocharger Model

Turbocharger is also modeled as a lumped model. The heat lost in the work done by turbocharger during cold start is negligible and hence, turbocharger is considered just a thermal body. A thermocouple is mounted at the outlet of the turbocharger used to measure the exhaust gas temperature. These values are used to compare the estimated values to validate the model. The convective heat transfer coefficient is calibrated as a function of turbocharger body temperature. Figure 61 shows a comparison between the estimated and measured gas temperature values at the outlet of the turbocharger. Inlet temperature to the turbocharger is the outlet temperature of the exhaust manifold. The exhaust gas temperature at the outlet of the turbocharger seems to reach a steady value after 6000 cycles. The outlet temperature of the turbocharger will be treated as the inlet temperature for the catalyst model.
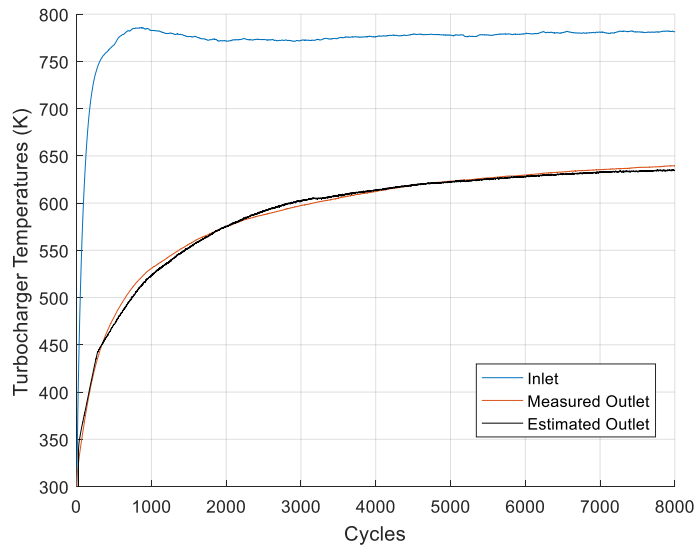
Figure 61: Comparison of Measured and Estimated Turbocharger Outlet Temperature

85

5.8 Catalyst Model

As discussed earlier, the catalyst is modeled for thermal gradient including re-evaporation of the condensed vapor in the exhaust gas. This is important because of the possibility of earlier part of catalyst reaching light-off temperature whereas the temperature of later part is still below the catalyst light-off temperature. Note that the heat generated due to exothermic chemical reactions is not considered and only the thermal part is covered. Two methods are proposed in this thesis for estimating catalyst substrate temperature and catalyst outlet temperature. The results from Method 1 and Method B are shown in this section.

Method 1

In Method 1 of estimating the temperatures of catalyst, first catalyst substrate temperature is calculated neglecting water re-evaporation and then that temperature is used to calculate the new temperature with re-evaporation. Figure 62 shows a comparison between the measured and estimated gas temperature at the outlet of the catalyst for inlet temperature as shown in blue.
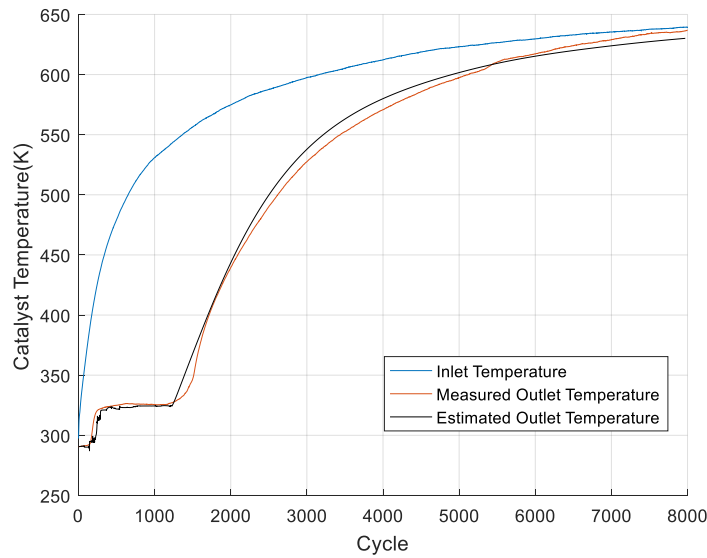
Figure 62: Comparison of Catalyst Outlet Measured and Estimated Temperature using Method 1

As the catalyst is modeled for thermal transient, the catalyst is to be divided in *n* number of parts. For this study, the catalyst is divided into 25 parts as shown in Figure 63 and Figure 64. Figure 63 shows the curve for gas temperature at the outlet of every division of the catalyst. Figure 64 shows the substrate temperature of each part of catalyst has a different temperature. The curve for the exhaust gas temperature and catalyst substrate temperature flattens at around 326K. The dew point temperature of the exhaust gas for E10 fuel is 326K, and hence the condensation and re-evaporation can be observed in that region.

87
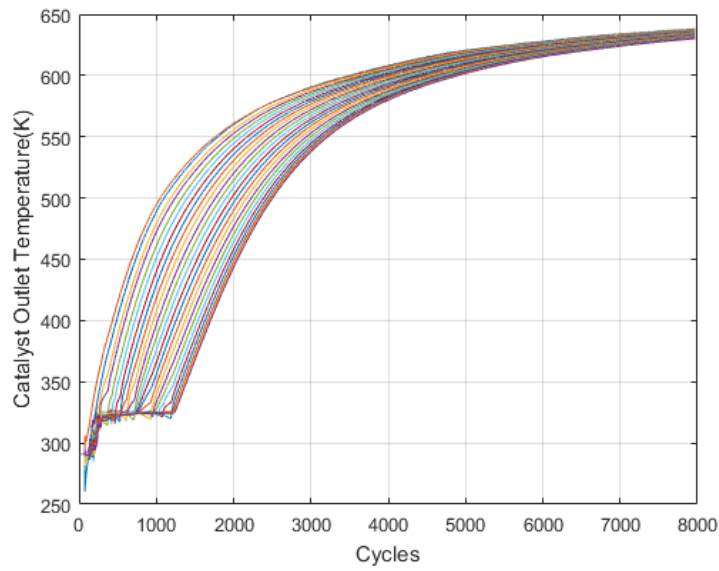
Figure 63: Estimated Outlet Gas Temperature from each part of Catalyst Using Method 1
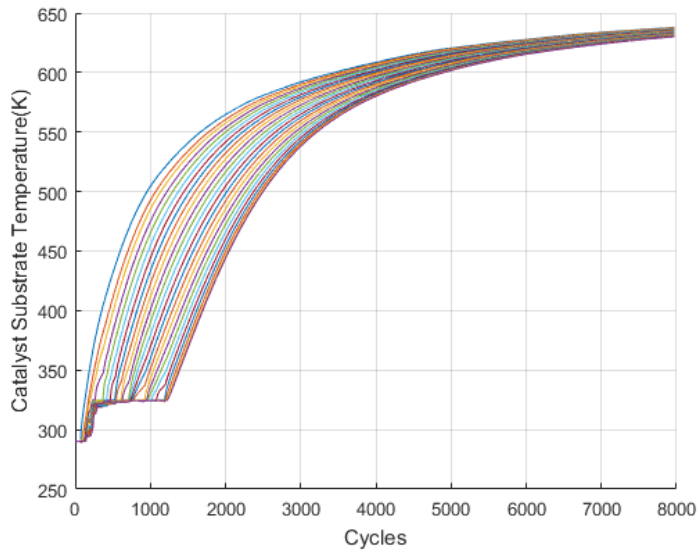
Figure 64: Estimated Catalyst Substrate Temperature when Catalyst divided in 25 parts using Method 1

Method 2

In Method 2 of estimating the temperatures of catalyst, the mass of water to be evaporated and converted to mass flow rate using engine speed and the catalyst

88

substrate temperature for next cycle is determined. Similar to Method 1, a comparison between the measured and estimated gas temperature at the outlet of the catalyst for inlet temperature is shown in Figure 65.
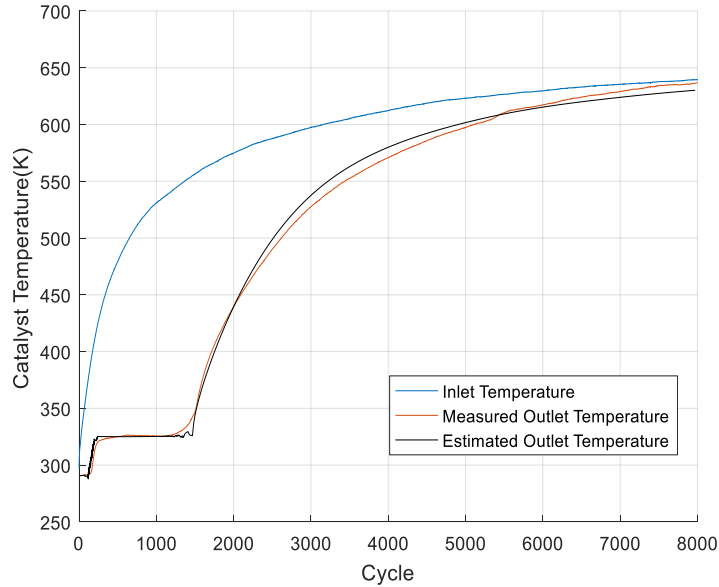
Figure 65: Comparison of Catalyst Outlet Measured and Estimated Temperature using Method 2

The catalyst is divided into 25 parts and the gas temperature at the outlet of every division and catalyst substrate temperature of each part can be seen in Figure 66 and Figure 67 respectively. Again, the flattening of the exhaust gas temperature can be seen at 326K because of the condensation and re-evaporation of water vapor.
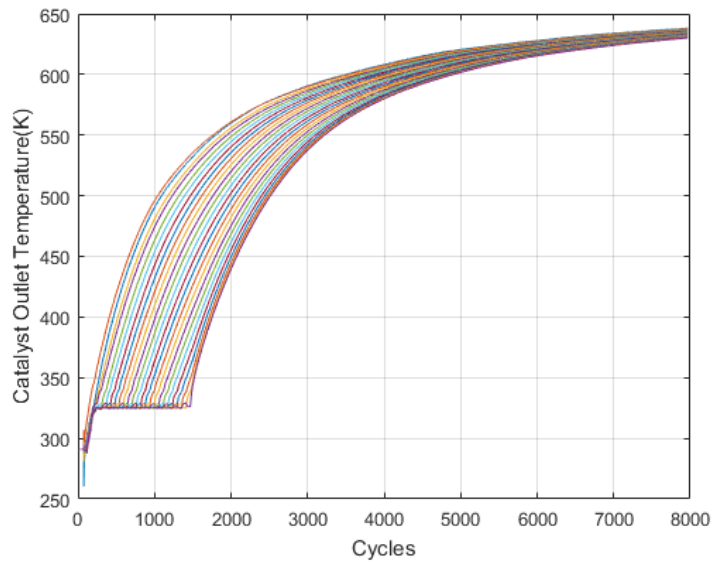
Figure 66: Estimated Outlet Gas Temperature from each part of Catalyst Using Method 2
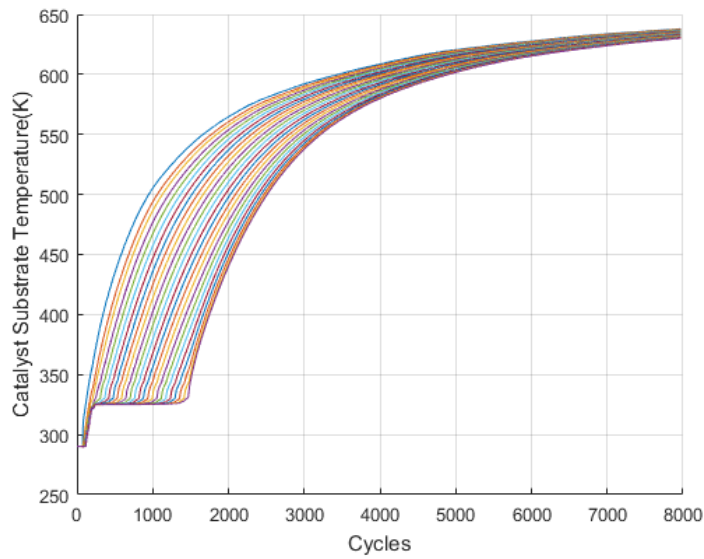
Figure 67: Estimated Catalyst Substrate Temperature divided in 25 parts using Method 2

90

5.9 Summary of Catalyst Model

The axial temperature distribution of the exhaust gas and substrate temperature is higher at the beginning of the cold start but tends to narrow down in later cycles. This shows the temperature of the exhaust gas as well as catalyst comes to steady state temperature value and any axial temperature distribution can be hardly seen.

The temperature curves using Method 2 looks smooth than the temperature curves using Method 1. This is because a single equation is used for in Method 2 whereas, an additional step is involved in calculating the catalyst substrate. The extra step of assuming same energy transfer with and without re-evaporation, induces a small dip in the exhaust gas temperature because of latent heat of vaporization, which is physically not possible.

Currently the catalyst model is calibrated for 25 divisions. If the same calibration is used for lesser number of divisions, the drop in the exhaust gas temperature across every element will be huge. If the temperature drop is huge, the amount of vapor condensed would also be huge as the amount of condensed vapor is calculated using inlet and outlet temperature of each element. A large amount of condensed water leads to large amount of energy released due to condensation. Re-evaporation also works in similar technique. The large amount of energy transfer to/ from the catalyst body would lead to sudden increase and drop in catalyst body temperature. This behavior of catalyst temperature is not expected physically. Hence the model needs different calibration values if to be used for lesser number of catalyst divisions.

Biot's number is a dimensionless quantity used to give a comparison between convective and conductive heat transfer.

$$N_{Biot's} = \frac{R_{conductive}}{R_{convective}} \qquad (49)$$

Where, $R_{convective}$ and $R_{conductive}$ are the convective and conductive resistances respectively. $R_{convective}$ can be calculated as below.

$$R_{convective} = \frac{1}{h.A} \qquad (50)$$

Where, h is the coefficient of convective heat transfer and A is the surface are in contact. And $R_{conductive}$ can be calculated as below.

$$R_{conductive} = \frac{x}{k.A_c} \qquad (51)$$

Where, k is the coefficient of conductive heat transfer and A_c is the cross sectional and x is the length.

For the current calibration for 25 divisions, the Biot's number is 1.2. This indicates that both conduction and convection heat transfer play important role in the determining the temperature of the catalyst substrate.

Chapter 6

Summary and Conclusion

6.1 Summary

In this thesis, correlations between split injection parameters meaning, one injection in intake and another in compression, with combustion parameters and engine exhaust temperature including ignition delay, *CA50*, burn duration are shown for 1250 *RPM* and 2.5 bar *IMEP*. These correlations can be later used for control purposes. The control parameters included in the correlation are *SOI. EOI, SR* and *SA*.

This thesis also comprises of exhaust thermal model where exhaust downstream components like exhaust manifold, turbocharger and catalyst are modeled. Exhaust Manifold and Turbocharger are modeled as lumped model whereas the catalyst model has been modeled as a thermal gradient model using two different techniques. Thermocouples mounted on exhaust manifold are used to measure exhaust manifold body temperature and exhaust manifold outlet gas temperature, another thermocouple is used to measure the outlet gas temperature from the turbocharger and a few more thermocouples on the catalyst to measure the gas temperature. These thermocouple readings are used to calibrate the exhaust thermal model.

6.2 Conclusion

Conclusions that can be made for the split injection correlations.

- Start of injection timing for first injection (*SOI*) does not have a significant role in estimating combustion parameters and exhaust temperature. This may be

93

because extremely retarded spark timing, which allow enough time for vaporization and mixing of fuel with air.

- $CA50$ ($R^2=0. 88$) and $CA10-90$ ($R^2=0. 84$) have better correlation fit than $CA00-10$ ($R^2=0. 75$) which can be seen from the R-squared values. More tests can be done to fine tune the correlations and improve R-squared values.

- Spark Timing, EOI and SR are significant factors in $CA50$ correlations. This can be seen from the Pareto Charts. Standardized effect values for Spark Timing, EOI and SR are 14.4, 6.5 and 5.7 respectively for Method A and 14.5, 6.6 and 5.8 respectively for Method B for the reference significance value of 2.07.

- Spark Timing, SR and EOI are significant factors in $CA10-90$ correlations. This can be seen from the Pareto Charts. Standardized effect values for EOI and SA are 9.0 and 4.7 respectively for Method A and 7.5 and 5.3 respectively for Method B for the reference significance value of 2.07. Standardized effect values for interaction terms of $EOIxSR$ and $SA*SR$ are 3.2 and 4.2 respectively for Method A and 2.4 and 3.6 respectively for Method B.

- Similarly, from the Pareto Chart for $CA00-10$ shows that EOI, SR and Spark Timing are significant in the correlation. Standardized effect values for Spark Timing, SR and EOI are 6.9, 6.0 and 4.5 respectively for Method A and 7.5, 6.5 and 4.5 respectively for Method B for the reference significance value of 2.07.

- Spark Timing play an important role in estimating the exhaust temperature. Standardized effect values for Spark Timing is 4.9 for the reference significance value of 2.07.

- The two techniques shown in calculating the combustion parameters gives similar results. The model to model comparison gives $R^2>0.99$ for $CA50, CA10-90$ and $CA00-10$ correlations. Therefore, either of the technique for calculation of combustion parameters can be used.

94

- The correlations are only good for 1250 RPM engine speed. Engine runs at 1250 RPM during the high speed idle period for a cold start.

Conclusions that can be made for Exhaust Thermal Model are:

- Condensation of water vapor in exhaust plays an important role in defining the temperature curve of the catalyst. Hence, should not be neglected. This can be seen from the flattening of temperature curve at dew point temperature of 326K.
- Both techniques for re-evaporation calculation (Method 1 and Method 2) shown to model the catalyst temperatures gives a good match with the experimental data proving that either of the method can be used in modeling catalyst temperatures.
- Method 2 for handling water vapor is better. It has simpler equation and gives smooth temperature curves. Whereas, a small dip in the gas temperature can be seen while using Method 1.
- The heat generated due to exothermic reactions in the catalyst is neglected in the catalyst model. In reality, the temperature values at various parts of the catalyst may be higher than the modeled temperature values. These catalyst temperatures at different parts of the catalyst might be even higher than the inlet gas temperature.
- For the current calibration for 25 divisions, the Biot's number is 1.2. This indicates that both conduction and convection heat transfer play important role in the determining the catalyst substrate temperature

6.3 Suggestions for Future Work

Following suggestion can be taken into consideration to improve the split injection correlation and exhaust thermal model work:

- More testing can be done to fine tune the correlations. Now that it is known *SOI* does not play a significant role in correlations, testing can be done with more focus on *SR*, *SA* and *EOI*.

- Emissions analyzer was unavailable during this work. Correlations can be made for emissions as well with the split injection parameters once the emission bench setup is complete.

- The exhaust manifold model and turbocharger model are now modeled as lumped model. These can be changed to heat distributed model for better results.

- Heat generated by exothermic reactions in the catalyst is neglected for the work in this thesis. This heat can be taken into consideration for improved temperature curve.

- As explained in Section 5.9, the catalyst model can used with lesser divisions by changing the calibrated parameter values for control purposes.

Chapter 7

7.1 Spark Plug Fouling Background and Literature Review

There has always been a problem of fouling of spark plugs during cold start. According to Greenshields [25], there are three types of fouling. 1) Short circuit due to bridging of gap between the electrodes which may be caused due to increase of engine operation output, which fuses deposits laid on it or due any other engine part like exhaust valve or piston crown. 2) Decrease of shunt resistance due deposition on ceramic core which provides an alternative path at elevated temperatures. 3) Corona discharge over the whole ceramic of the spark plug due to presence of conductive material distributed discontinuously over the surface.

Jawad and Sobolak [27] studied the effects of cold temperature on spark plug performance. They soaked the vehicle with an engine which was prepped to the condition as seen at the assembly plan in cold camber maintained at 20 °C. After soaking the engine for 8 hours in the cold chamber, the test procedure involved starting the engine, shifting the transmission into drive and running the engine at full throttle for 20 secs. Then the engine was allowed to soak for another 15 mins and the same procedure was followed until the spark plug gets fouled. Table 7 shows the results for the tests and it can be concluded that additive enriched fuel plays a significant role to combat cold weather spark plug fouling.

Table 7: Fuel properties versus quantity of starts before the spark plug fouled, data extracted from [27]

Fuel Number	Fuel ID	RVP (psi)	Ethanol %	Engine fouled at test number
1	BASE	12.5	0	40
2	RVP High	15.0	0	45
3	RVP Low	10.0	0	43
4	Ethanol	12.5	10	60
5	Additive	12.5	0	65

Several works have been done to use ion probe as tool to study combustion. Ion signal has been proven to be a good in-cylinder signal to be used to detect misfire and predict knock due to Pre-Ignition (P.I.) [29]. NOx generation is also studied using ion signal and results shows that ion has good potential in predicting NOx generation [30]. The ion signal shows characteristics which seems related to the combustion happening inside the cylinder [28] which is also explained in the next section of this Chapter. Henein et al., [28], performed a study with different ion probes and made the following observations.

- Probe length influences the characteristics of the ion signal, short length probes give signal with more peaks, indicative of flames and combustion whereas, longer probes give signals with less ion peaks.
- Soot deposits on the probe reduce the resistance between the ion probe electrodes and produce a zero shift.
- The first combustion peak represents the rate of heat release and the second and third (if any) are related to mixing and diffusion-controlled combustion.

There are mainly two sources of the ion current in an IC engine i.e. chemi-ionization and thermal ionization [31]. For the chemi-ionization, CH radical is responsible for the ion current in a gasoline engine and the ion formation reactions are as follows,

$$CH + O \rightarrow CHO^+ + e \qquad (52)$$

Above reaction is competitively slow as compared to the following reactions,

$$CHO^+ + H_2O \rightarrow H_3O^+ + CO \qquad (53)$$

$$CHO^+ + NO \rightarrow NO^+ + HCO \qquad (54)$$

$$CH^+ + C_2H_2 \rightarrow C_3H_3^+ + e \qquad (55)$$
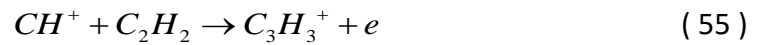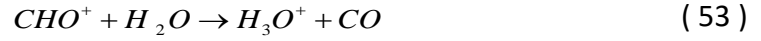
In lean and slightly rich conditions, reaction (53) is dominant whereas reaction (55) is dominant during rich and sooty conditions. The ions recombination reaction is:

$$H_3O^+ + e \rightarrow 2H + OH \qquad (56)$$

For thermal ionization, formation of ions at high temperature is mainly due to the following reaction [32]:

$$NO + M \rightarrow NO^+ + e + M \qquad (57)$$

The ions recombination reaction is:

99

$$NO^+ + e \rightarrow N + O \qquad\qquad (58)$$

7.2 Ideal Ion Waveform

An ideal ion curve sensed from the spark plug with a typical in-cylinder pressure curve is shown in Figure 68. When a coil is connected to a spark plug, the secondary voltage of the ignition coil must rise enough to break the potential between the spark plug known as breakdown voltage. The amount of time taken by the ignition coil to charge until the breakdown voltage is known as dwell. While measuring the ion current using the spark plug, it is being observed that the ion signal is interfered at the start of dwell and shows as spike on the ion signal. Figure 68 shows an ideal ion curve with single spark event.
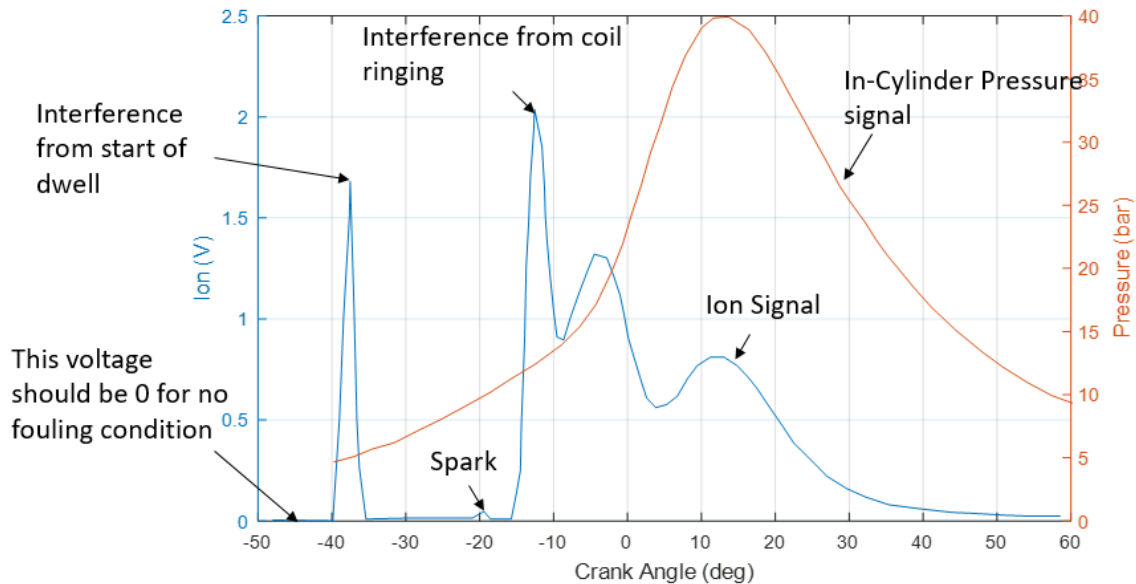
Figure 68: "Ideal" Ion Curve

After the interference from the dwell, an ideal waveform of a clean plug, should drop to 0 volts and continue to be 0 volts until spark occurs. A small hump in the waveform indicates spark event as seen in Figure 68. When, not enough power remains in the

100

ignition coil, spark ends, and the remaining power is rung out. This can be detected by a second peak at the end of spark. The rest of the curve indicates the combustion happening inside the combustion chamber.

7.3 Literature Review Summary

A lot of work is done to prevent fouling of spark plug with either using additives in the fuel or using different calibrations on the engine until the vehicle reaches the customers. All the studies focusing on reduction of soot formation on the spark plug to improve engine startability involves visual inspection of the spark plug. This requires physically removing the spark plug which takes a lot of time and human effort.

Although ion probe is widely used in combustion analysis, PI determination and NOx formation, it has not been used to determine the condition of a spark plug. The principle of zero shift of the ion current because of soot formation on the electrodes, is used to determine the shunt resistance of the spark plug.

Chapter 8

8.1 Experimental Setup

A 2.0L four cylinder Direct-Injection (DI) engine on Lincoln MKC was used to run tests to measure the spark plug fouling. Spark plug was used as a probe to measure the ion current from the cylinder. Engine geometry are shown in Table 8.

Table 8: 2L Ford Ecoboost Engine Specifications on Lincoln MKC

Bore	87.5 mm
Stroke	83.1 mm
Connecting Rod Length	155.86 mm
Wrist Pin Offset	0.6 mm
Compression Ratio	9.3:1
Engine Displacement	1.999 L
Number of Cylinders	4
Firing Order	1-3-4-2

Signals to PicoScope

Ion Box

Signals from Ionization Coils (Secondary Negative)
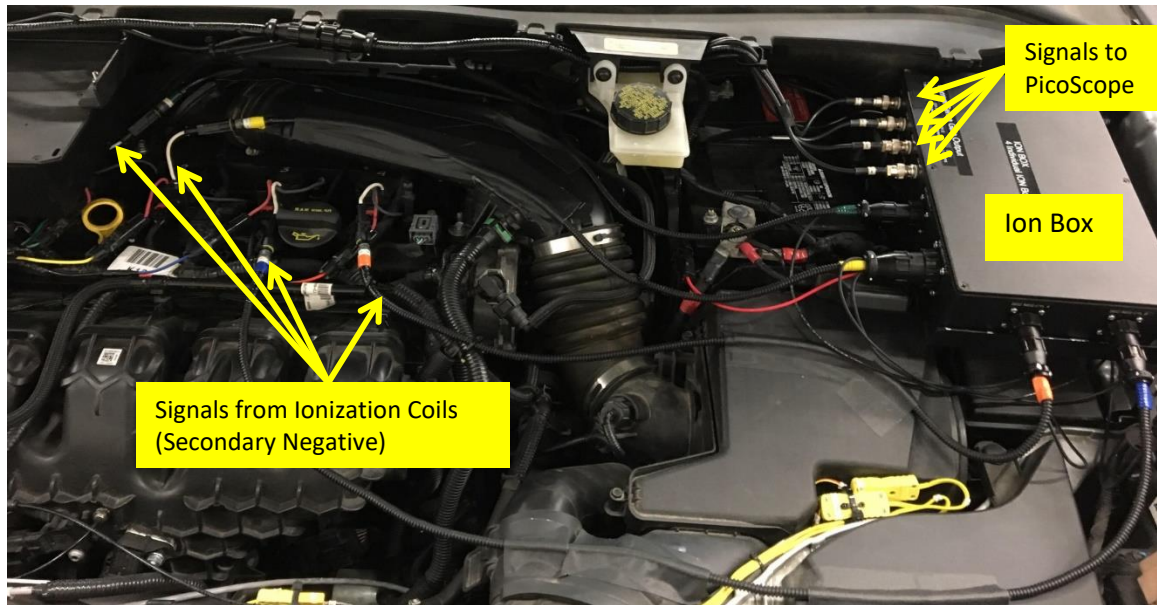
Figure 69: 2L DI engine mounted with modified ignition coils connected to ion box

Figure 69 shows the experimental setup on the vehicle to measure the shunt resistance of all the four spark plugs. Ignition coils on the engine are modified to take a secondary negative output to measure the ion current. The ion current is typically around 200 μA or less. This signal is fed to the Ion Box installed under the hood of the vehicle. Initially the secondary negative wires were routed together which led to noise issue in the signal. Separated wires resulted in better ion signal quality. The ion box uses a DC to DC converter is used for greater stability and higher voltage capacity. Also, the value of *R1* can be modified for desired sensitivity (Figure 70).
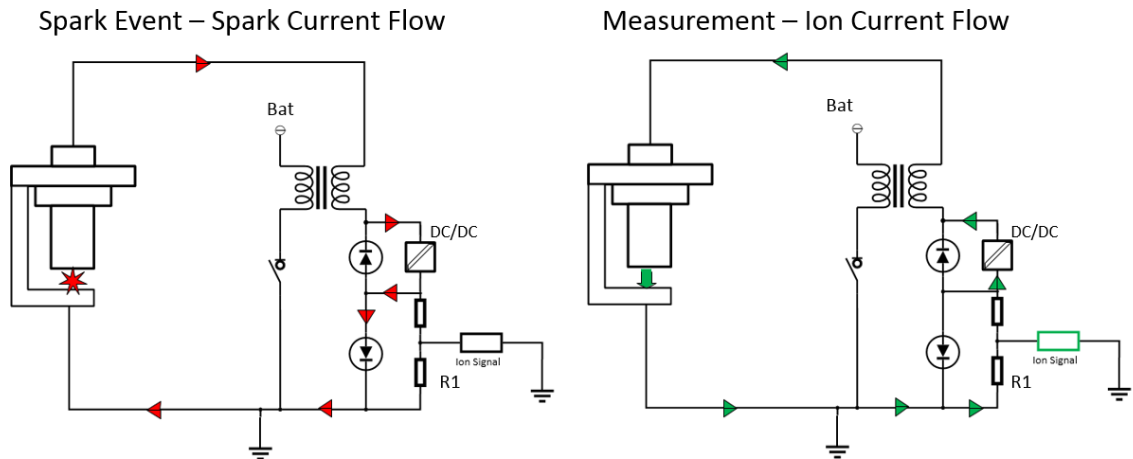
Figure 70: Ion Measurement Principle

Two different ion boxes were present one with 250 *KΩ* resistance as *R1* and the other with 1 *MΩ* resistance on the other box. The 250 *KΩ* ion box outputs the signal with a voltage range of 0 to 5*V* and the 1 *MΩ* ion box outputs signal with a range of 0 to 10*V*.

A PicoScope 4824 [33] was used to measure the ion signal from the ion box. Sampling rate was set up to 20 *KS/s* and sometimes 30 *KS/s*. This sampling rate range was defined for better computation speed on the tool and to capture minute details on the ion signal.

Figure 71: PicoScope for data logging [34]

104

ATI Vision [22] software was used as the ECU interface to control the engine calibration parameters including spark timing (SA), mass of fuel injected (m_f), and split injection parameters like SOI, EOI and SR. The vehicle was tested in parking lot and in the cold chamber with temperature of 0°F. The engine was calibrated to force spark plug fouling. Also, ATI is important for logging calibration parameters data which can be plotted by the tool for proper interpretation of results.

ATI EDAQ (Figure 72) can also be used to capture ion data simultaneously. The signal from the ion conditioning box is split up, one goes to PicoScope and other goes to ATI EDAQ. The reason PicoScope is used is because of its higher sampling rate which allows the capture of minute details of the ion signal, which EDAQ fails to capture. The purpose of ATI EDAQ will be explained in Section 9.3.2.

Figure 72: ATI EDAQ to capture ion signals [35]

Chapter 9

Plug Fouling Algorithm

9.1 Overview

Ion signal was recorded using PicoScope and calibration parameters were recorded using ATI Vision. For any test done to measure the spark plug fouling, the calibrator or the person doing the test must start recording data on PicoScope and ATI Vision first and then start the engine. The tool will not work correctly if data logging is started while the engine is already running. The tool will also work if ATI Vision is not available for logging the data. The use the tool, a simple four following steps are to be followed.

1. Start logging data in ATI Vision and PicoScope
2. Start the cold start test
3. Save the logged files in Matlab file format (.m) in a same folder
4. Run the plug fouling diagnostic tool

The algorithm on which the tool works is shown in Figure 73.

106
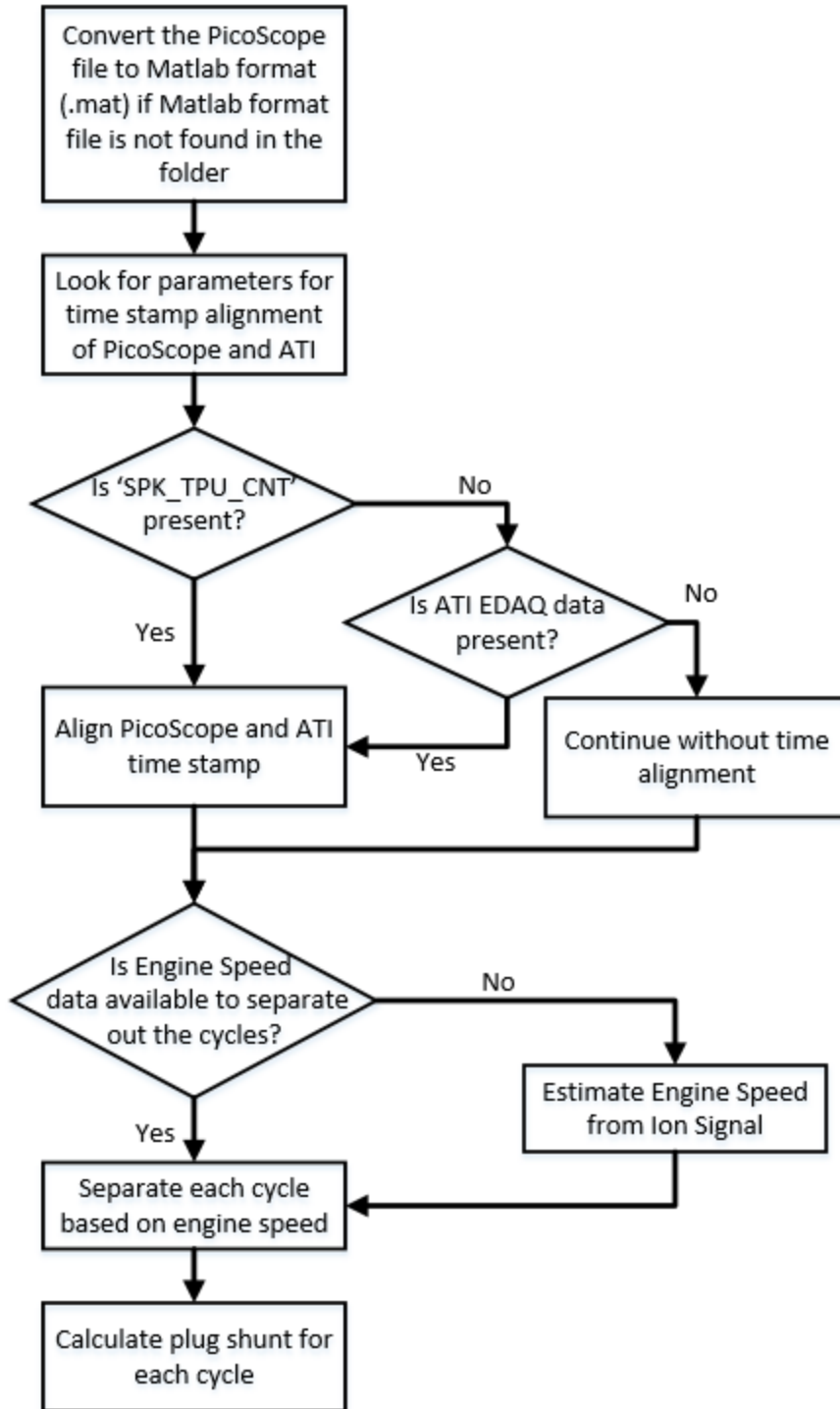
Figure 73: Algorithm for plug fouling diagnostic tool

9.2 Filter and Analyze PicoScope Data

The spark plug diagnostic tool works for number of cylinders up to 8 but, it is not necessary that there are always 8 cylinders connected to the PicoScope. The tool looks for number of active cylinders.

PicoScope sometimes have missing values while recording the data. This happens when the ion signal shoots up like in case of interference from start of dwell and interference from coil ringing. The value is shown as infinite in the signal; hence, it becomes difficult for Matlab to recognize these values. Thus, these values are to be replaced by its neighboring values.
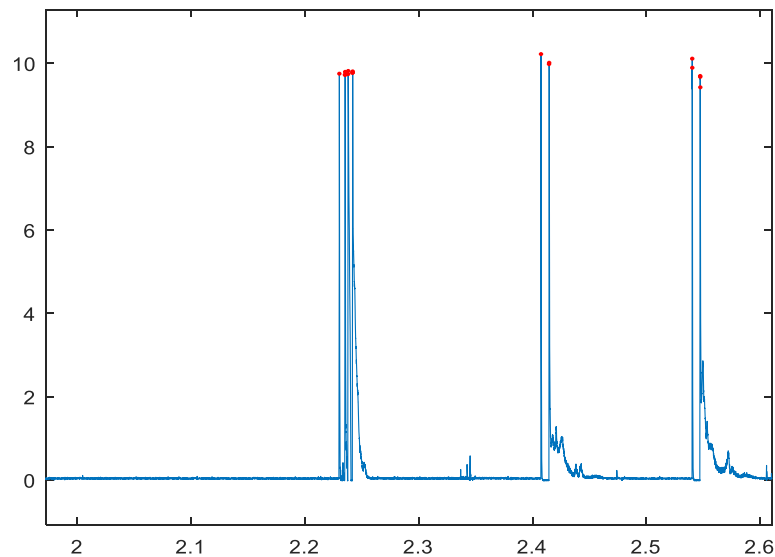
Figure 74: Ion Signal showing spikes due to interference due to start of dwell and coil ringing (red dots)

The data recorded in PicoScope is time based and not crank angle based. Therefore, each cycle must be separated out from the time based continuous signal. Start of dwell is used as an indication for cycle start and the cycle continues until next start of well spike is

108

recorded. For a 1 $M\Omega$ ion box, 7.5V is used as a threshold for separating out noise from the spike due to interference due to start of dwell and coil ringing. Similarly, 3.6V is used as a threshold for 250 $K\Omega$ ion box.

Figure 74 shows a sample of ion signal. The x-axis is the time stamp and the y-axis is the voltage value recorded in the PicoScope. The red dots show the spikes due to interference of start of dwell and coil ringing. Multiple spikes in first cycle shows spark restrikes which are sometimes used for starting the engine.

9.3 Alignment of PicoScope and ATI Vison time stamp

PicoScope and ATI Vision for data logging is started at different times. Although, these two are started nearly simultaneously before starting the tests, there is still a difference in both of their time stamps. These time stamps are to be aligned to match the Ion data with the ATI parameter data. This alignment is done via a parameter called "*SPK_TPU_CNT*" recorded in ATI. If "*SPK_TPU_CNT*" is not found, alignment is done via ATI EDAQ data.

9.3.1 Alignment via SPK_TPU_CNT

ATI Vision has a parameter called "*SPK_TPU_CNT*" which keeps a count number of spark events and the counter resets after 256 counts. The technique of alignment is matching the time of the spark count on counter with the first spike due to start of dwell on the ion signal. Because of the low sampling speed of the ATI, sometimes, 1st count on the counter is not recorded. Equation (59) is used to estimate the time of 1st count on the counter. It can be seen from Figure 75 that first peak on PicoScope is 9.8 sec whereas first count on the Spark Count is 3.4 sec. Figure 76 shows PicoScope time for first peak match with the ATI first count.

109

$$t_{spk(1)} = t_{spk(0)} + \frac{t_{spk(n)} - t_{spk(0)}}{n} \tag{59}$$

Where, $t_{spk(1)}$ is time for 1st spark on spark counter, $t_{spk(0)}$ is time for last 0 count on the spark counter, $t_{spk(n)}$ is time for first non-zero count on the spark counter and n is first non-zero value on the spark counter
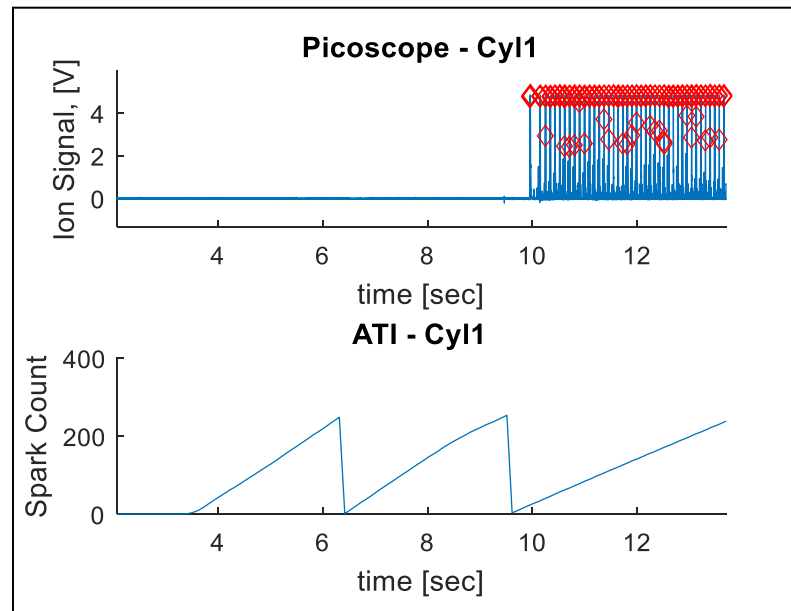
Figure 75: PicoScope and ATI data before alignment

110
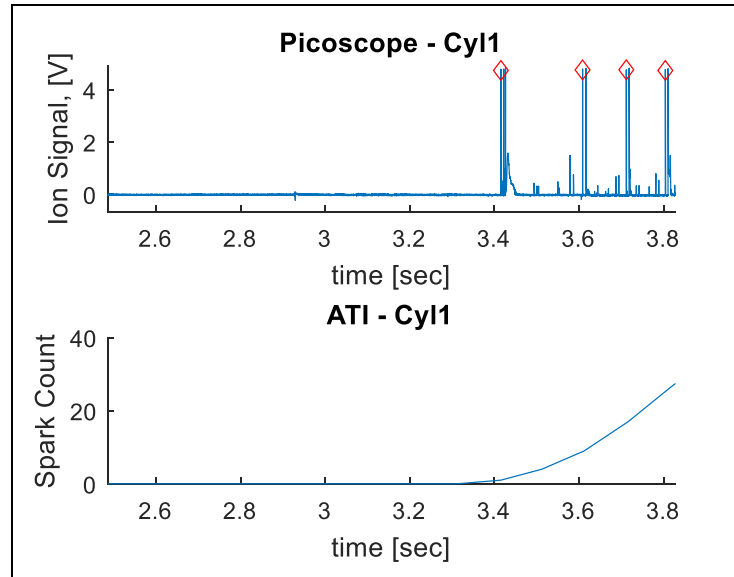
Figure 76: PicoScope and ATI data after alignment

9.3.2 Alignment via ATI EDAQ

The signal form the ion box is split up into two channels. One goes to PicoScope and the other goes to ATI EDAQ. ATI EDAQ is also used for data acquisition, but, the problem with using EDAQ is low sampling speed. Sampling rate slower than 20 *KS/s* is not preferred as it miss out a few intricate details of the ion signals like restrikes, diffusion flame, etc. Similar to separating out spikes in PicoScope data, spikes in ATI vision are detected for voltage more than $0.5V$. Time at the first spike in ATI Vision and time at the first spike in PicoScope is noted and time stamp is aligned accordingly. It can be seen from Figure 77 that first peak on PicoScope is 17.8 sec whereas first peak on ATI EDAQ is 6.5 sec. Figure 78 shows PicoScope time of first peak match with the ATI EDAQ first peak.

111
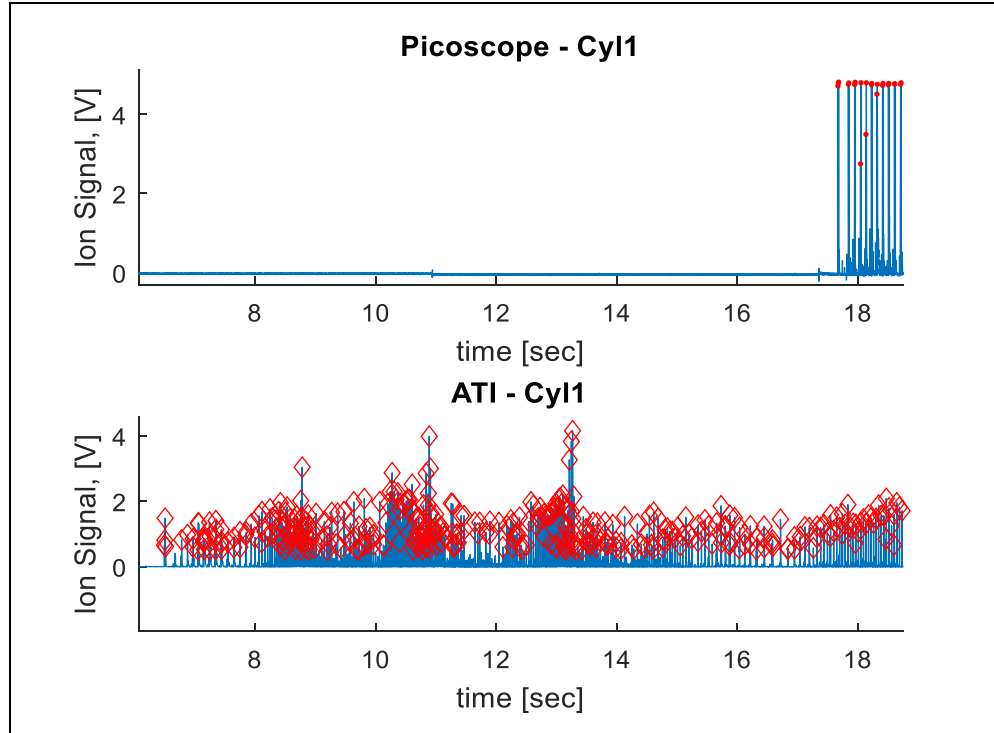
Figure 77: PicoScope and ATI data before alignment
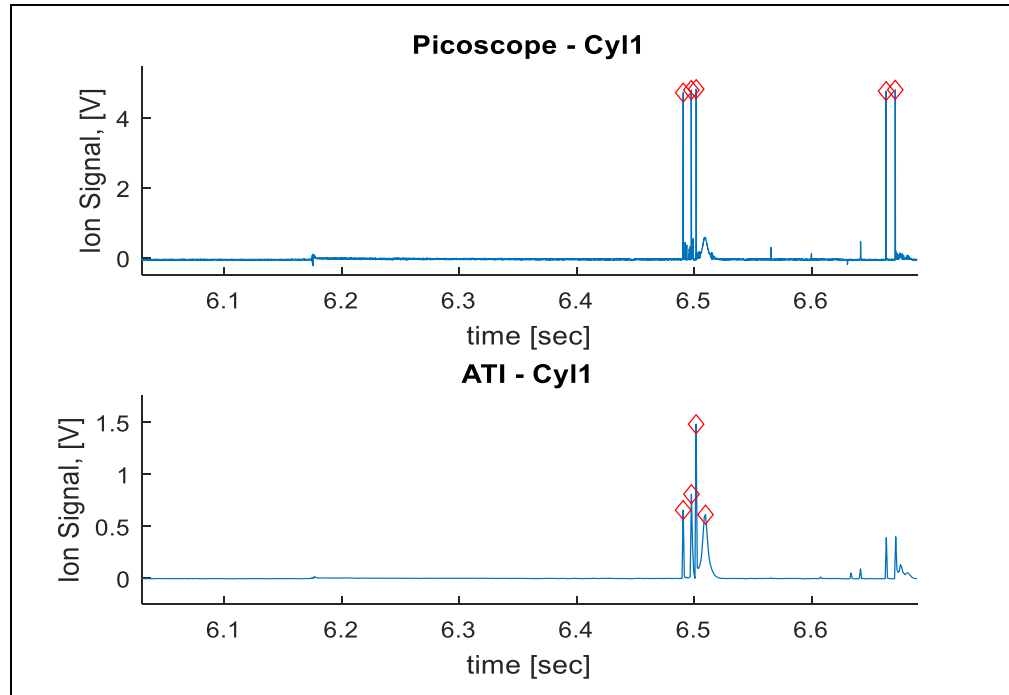
Figure 78: PicoScope and ATI data after alignment

9.4 Engine Speed Estimation

Ion data is logged as time-based data and not crank angle-based data. Each cycle must be separated out for fouling calculation for every cycle. Hence, engine speed as a parameter is used to separate out the cycles from each other.

113
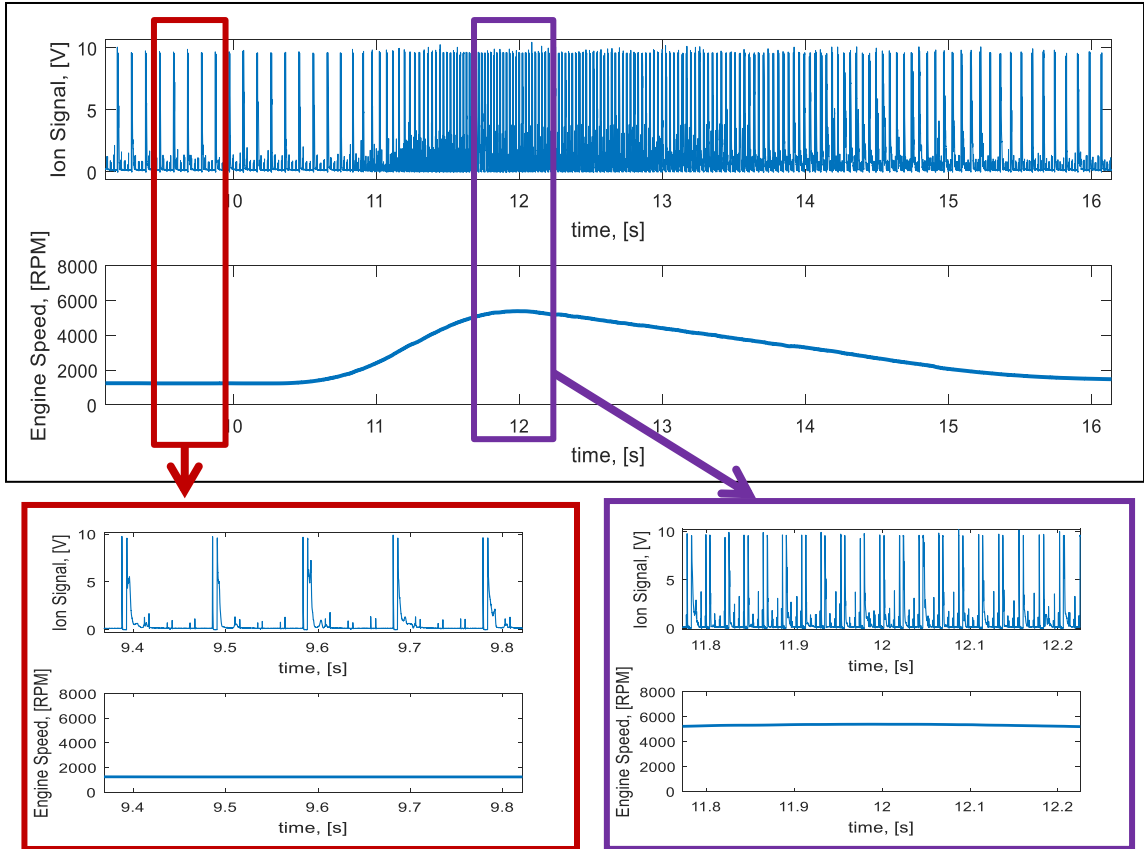
Figure 79: Ion Signal with Engine Speed

As shown in the Figure 79, cycles are well separated when then engine speed is slow and gets close to each other as the speed increases. Hence separating cycles out gets difficult. As seen in the figure in red, small spikes are seen between two consecutive cycles, are the cross talk between the cylinders. The amplitude of the cross-talk increases as the engine speed increases. Sometimes, the cross talks are as high as the threshold value set for separating out the spikes due to interference due to dwell and coil ringing. A look up was made to omit all the spikes which comes into a certain region of the cycle. This also takes care of the spark restrikes. This region of omitting spikes is based on engine speed. Hence engine speed plays a very important role in computing plug fouling.

114
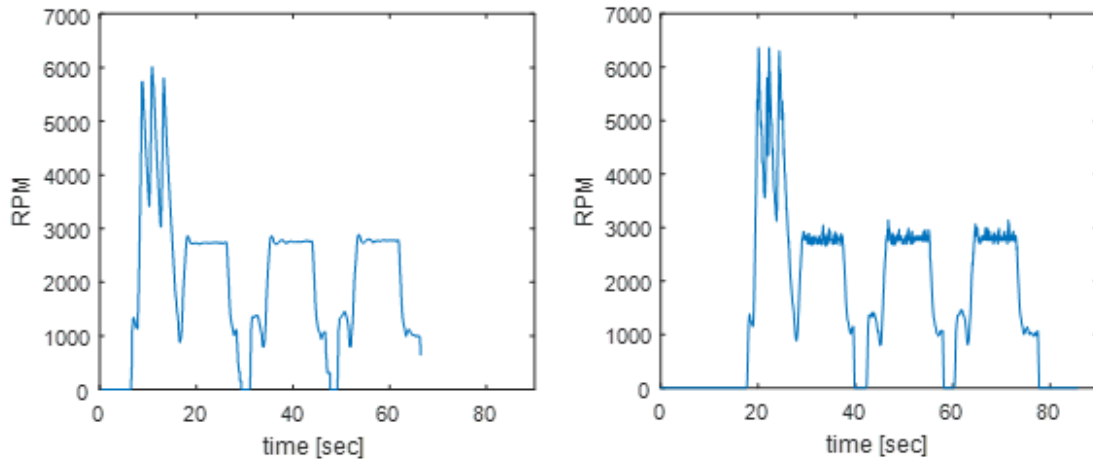
Figure 80: Actual Engine Speed (left) and Estimated Engine Speed (right)

If engine speed data from ATI is not available, engine speed is estimated. No engine speed data case will happen if the tool is to be used without ATI system installed on the vehicle. This would be the case if the tool is to be used by a spark plug supplier who wouldn't have access to ATI and only have PicoScope. Figure 80 shows a comparison between actual engine speed graph vs estimate engine speed graph. Engine speed is estimated using frequency of spikes in ion signal.

Finally cycles form a continuous ion data is separated out to measure plug fouling for each cycle. Figure 81 shows raw ion signal indicating all the spikes due to interference from dwell, coil ringing and restrikes. Whereas, Figure 82 shows same ion signal indicating only first spike due to interference from start of dwell after time stamp alignment.

115
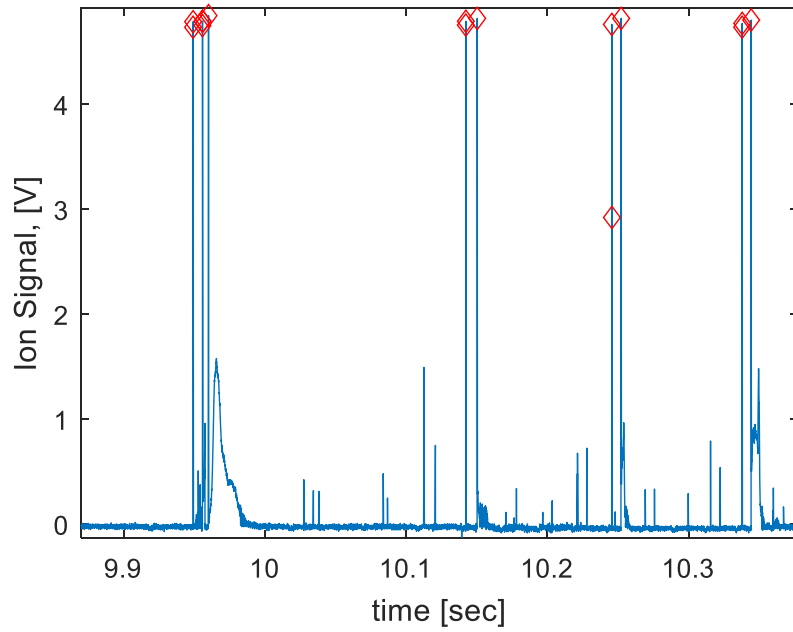
Figure 81: Sample ion signal with all spikes
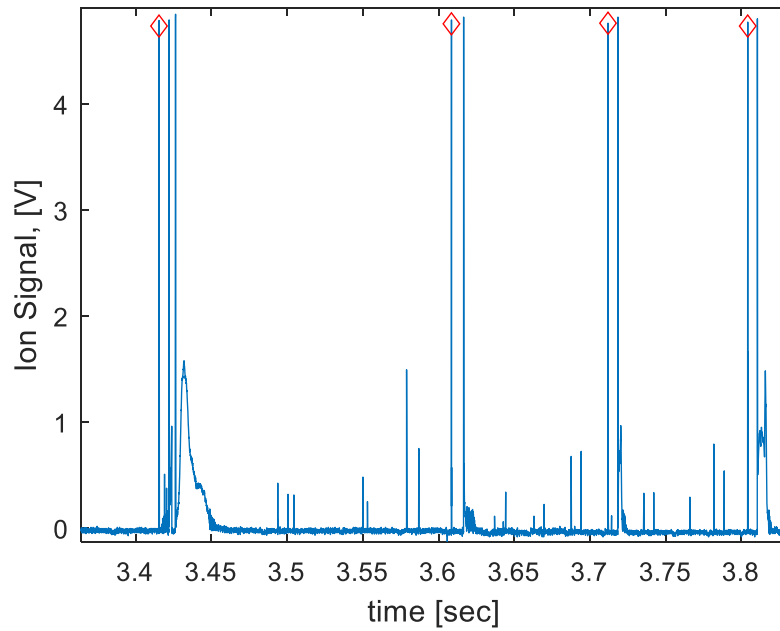
Figure 82: Sample ion signal with only start of dwell spikes separating out cycles after time alignment

116

9.5 Fouling Calculations

Spark plug fouling is measured by calculating shunt resistance over the entire conical surface of the ceramic insulator. A biased voltage of 180 volts is applied to the spark plug, as explained in Chapter 8. This shunt resistance is calculated based on the following equation.

$$R_{shunt} = R_{sen} \cdot (\frac{X_{scale} \cdot V_{bias}}{V_{offset}} - 1) \qquad (\ 60\ )$$

Where, R_{shunt} is the shunt resistance value of the spark plug, R_{sen} is sensitivity resistance value, Xscale is the scale factor, V_{bias} is bias voltage and V_{offest} is offset voltage.

V_{offest} is calculated using the ion signal from the engine. As explained in Chapter 8, the floor voltage should be ideally zero for no fouling condition. Once the spark plug starts to foul, the floor voltage starts to rise from zero. A portion of the ion curve is filtered for cross talks (noise). The values are rearranged in an increasing order and a mean value of first 90% of that portion is taken as shown in Figure 83.

The program plots shunt resistance values in different colors based on perceived risk of misfire. These limits can be changed in the software but as currently configured they are:

1. >800 *MΩ* - No Risk – Shown in green color
2. 1-800 *MΩ* - Minor Risk – Shown in orange color
3. <1 *MΩ* - High Risk – Shown in red color
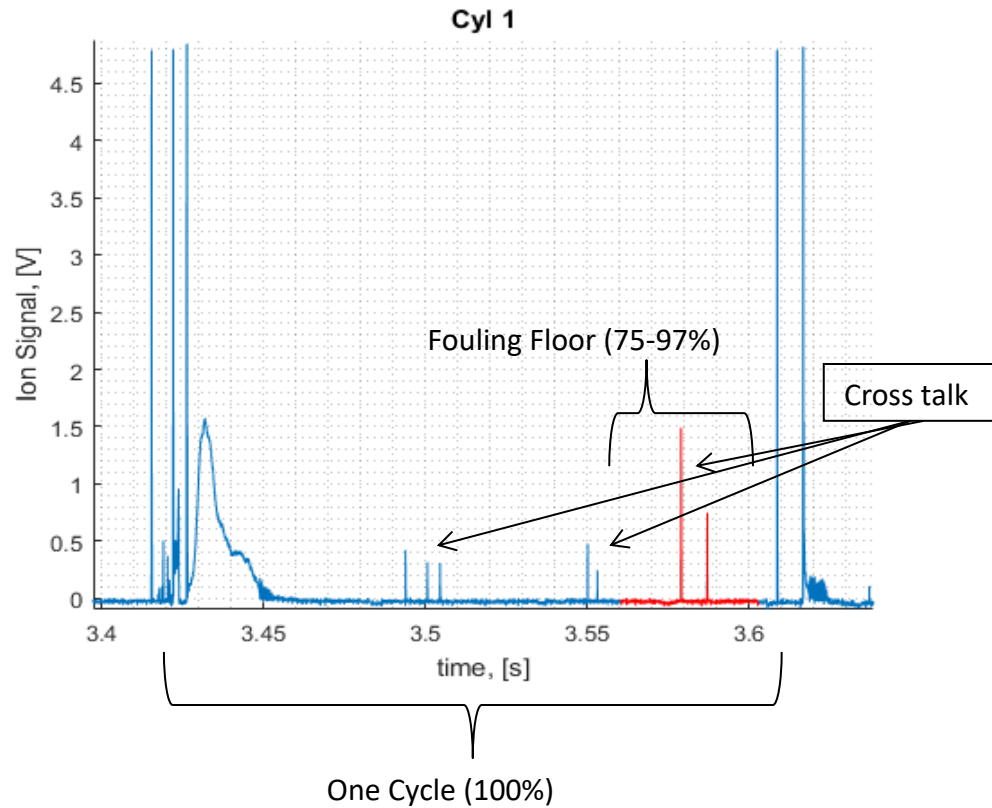
Figure 83: Ion signal showing interval for plug fouling computation

9.6 Diffusion Flame

Diffusion flame can be described as the burning of liquid fuel in the cylinder. Diffusion flame can also be studied using ion data from the combustion chamber. As discussed earlier ions are nothing but charges formed due to combustion and thermal effect. If a rise in ion signal is noticed late in the combustion cycle after the ion signal dips down to zero, it indicates that diffusion flame burning is occurring. The diffusion burning is also optically verified using an optical engine at APS labs Michigan Technological University.

118

Similar to fouling measurement, diffusion flame is quantified by selecting a portion of curve where diffusion flame is expected, and the ion values are integrated over that portion of the ion signal. The interval for selecting the portion of the ion signal is calibrated with engine speed. A look up table for start of the interval and end of the interval is made for various engine speeds.
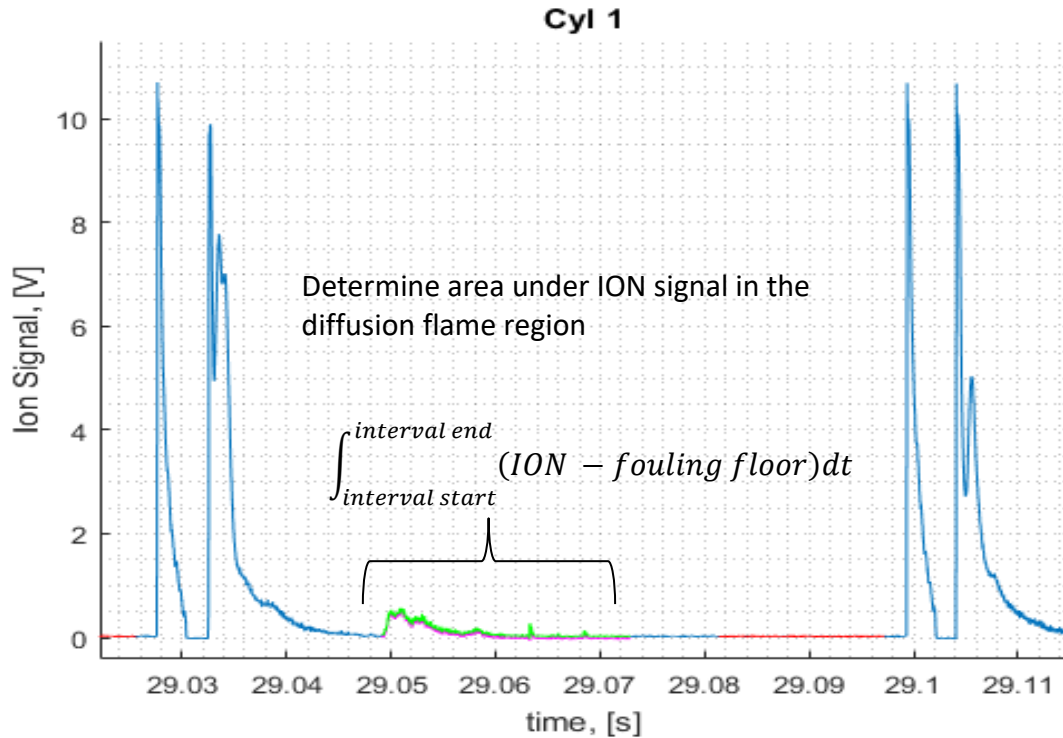
Figure 84: Diffusion flame calculations

Figure 84 shows the interval for diffusion flame calculation shown in the green color. If the spark plug is fouled, the area under the curve will tend to increase because of rise in floor voltage due to fouling. Thus, the floor voltage needs to be subtracted from the ion signal before computing the diffusion flame.

$$Diffusion\ Flame = \int_{interval\ start}^{interval\ end} (ION - fouling\ floor)dt$$

(61)

119

Chapter 10

Spark Plug Fouling Diagnostic Tool

10.1 GUI

A graphical user interface was developed for ease of usage of the diagnostic tool. User must enter the address of the folder where the PicoScope and ATI files are stored and the folder where he/she wants to store the result plots. Toggle switches for a few basic plots including for Diffusion Flame, SOI, EOI, SR and SA are added.
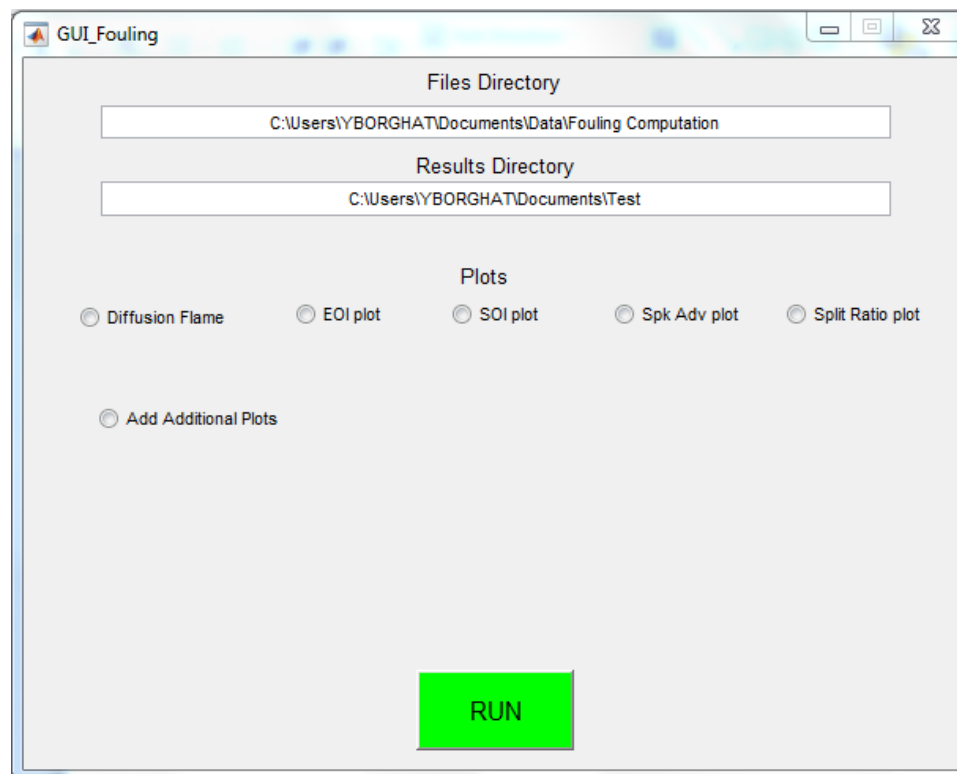
Figure 85: GUI for the plug fouling diagnostic tool

An option of additional plots is also given, where in after clicking for additional plots it'll ask you for the number of additional plots and the name of the ATI parameters for which fouling is to be plotted against.

Figure 86: GUI asking for ATI parameters to be added

Once everything is toggled and filled, hit run to display the results. Depending on the number of plots added, plots will be generated for each cylinder with fouling and against all the parameters added. Figure 87 shows a plot of ion curve with spark plug shunt resistance graph for cylinder number 2 of a 4-cylinder engine.
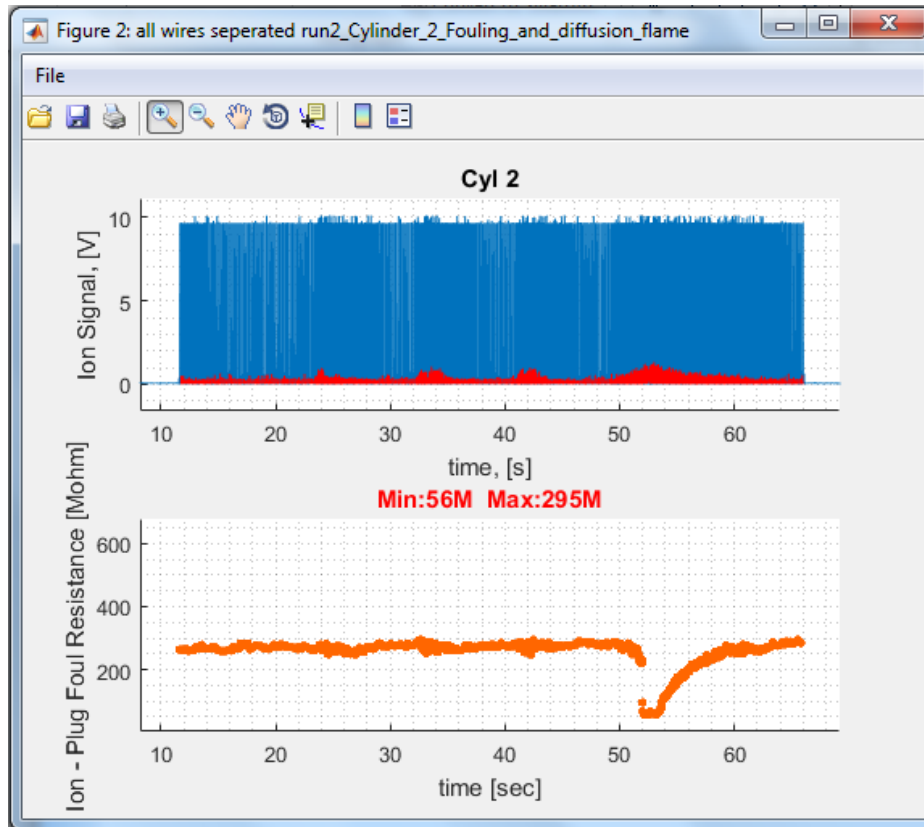
Figure 87: Shunt resistance curve with ion signal

If diffusion flame toggle is switched on, a diffusion plot will be added to the shunt resistance plot with the ion graph.

122
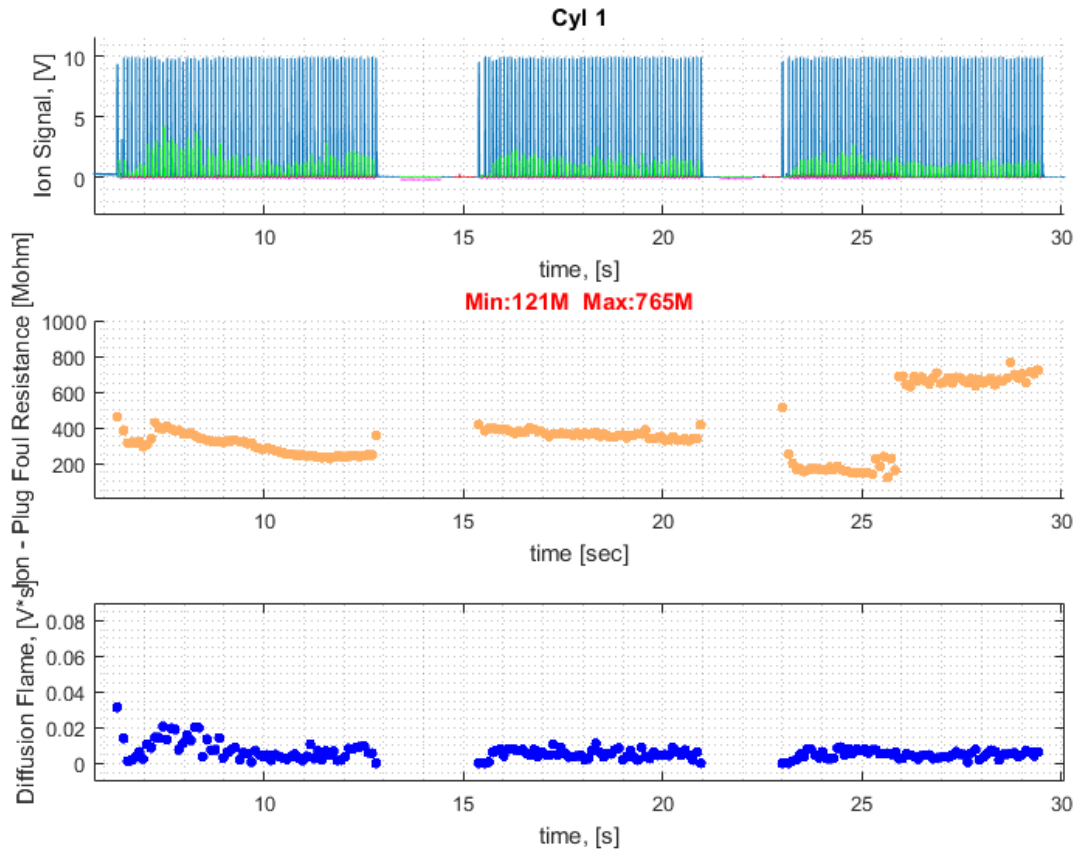
Figure 88: Shunt resistance plot with diffusion flame (in blue)

Figure 88 shows a typical graph for a three-consecutive start marshalling test. Figure 89 shows engine speed vs. spark plug shunt resistance for our cylinders for a three-start marshalling test.

123
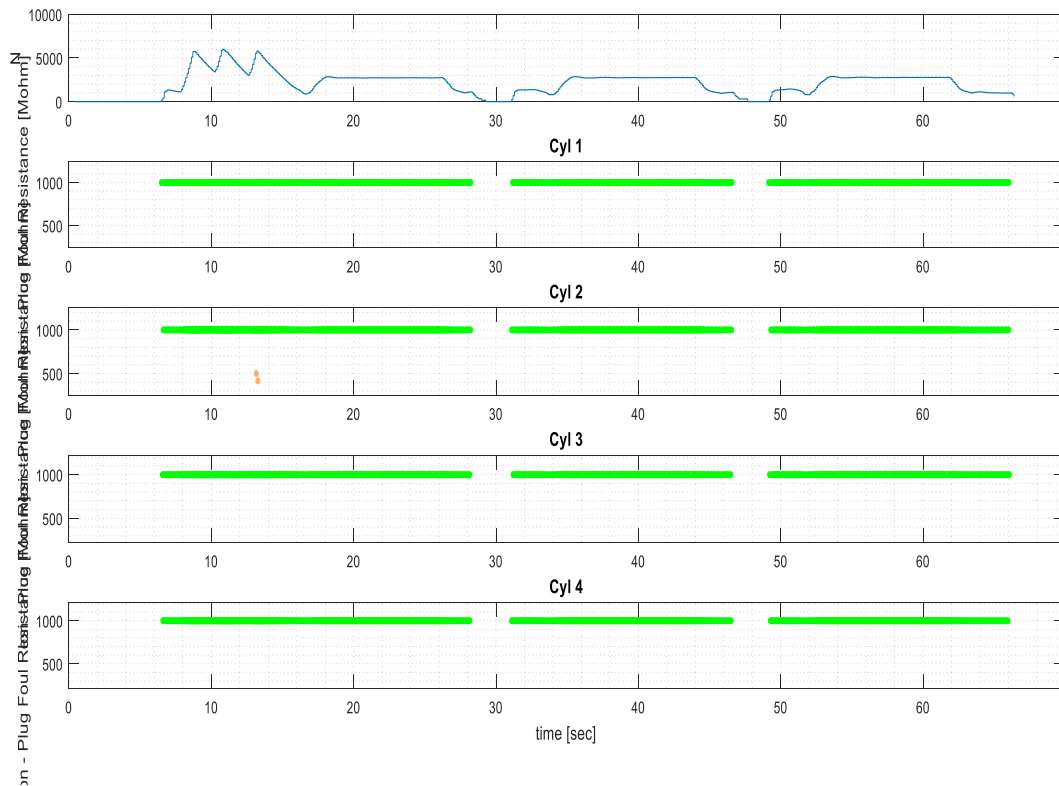
Figure 89: Engine speed from ATI with plug shunt resistance values of all 4 active cylinders

10.2 Fouling Cases

As the soot deposits on the ceramic insulator start to build up, the floor voltage of the ion signal starts to increase. This can be seen from Figure 90; Top left figure shows ion curve and shunt resistance values with no fouling (as shown in green markers) of the plug. Top right figure shows the ion curve behavior when soot deposition starts, and the shunt resistance starts to decrease but he plugs is at minor risk. Bottom left shows the ion signal with floor voltage rising high which puts the spark plug towards high risk condition. Finally, bottom right figure shows the worst-case condition. The floor voltage climbs up

and saturates at 10 volts. The inverted peaks are the time interval between the peak due to interference of start of dwell and coil ringing. Because the floor voltage being so high, the actual spikes due to start of dwell and coil ringing are not seen.
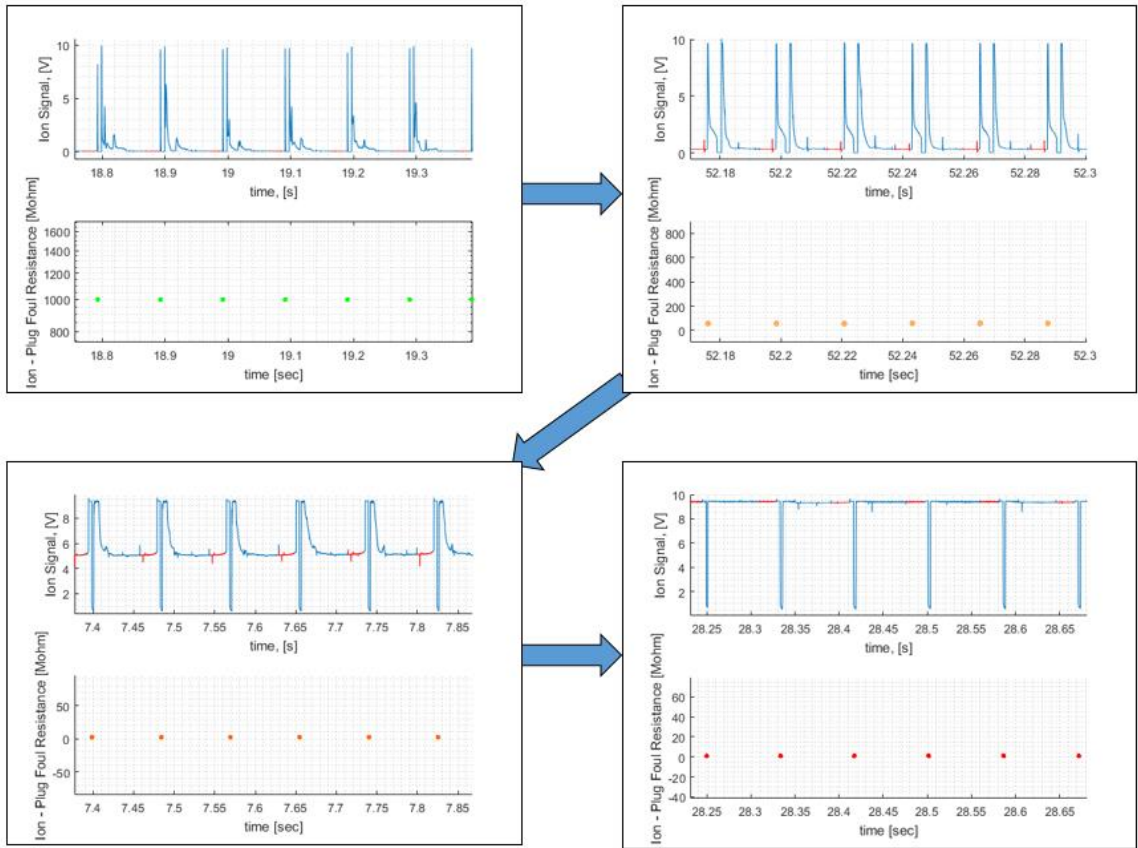
Figure 90: Various plug fouling cases

10.3 Adaptation to Worst Case Fouling

If the ion signal saturates if spark plug fouling is high enough then, it becomes difficult to separate out the cycles form each other.
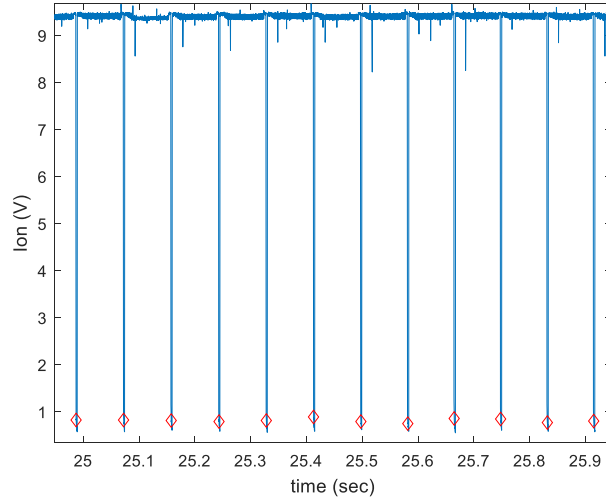
Figure 91: Worst Case Fouling

Hence, if the average of the ion signal is more than $6V$, the whole ion signal is subtracted from $11V$ to invert the signal. The inverted peaks are then used as a parameter to separate out the cycles.
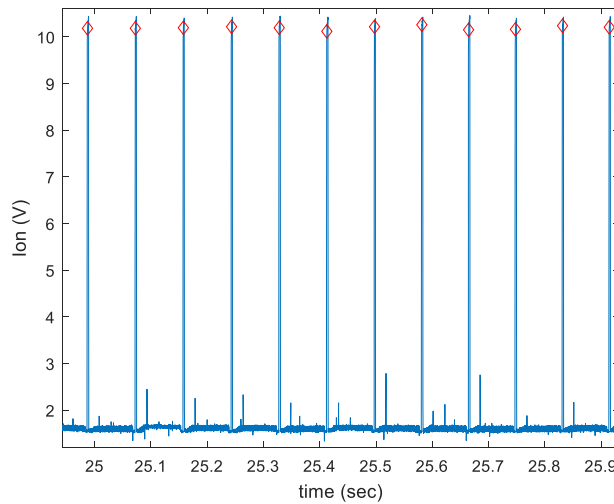
Figure 92: Inverted Signal

126

10.4 Uncertainty Analysis

Ion current is the only measurement done to estimate the shunt resistance of the spark plug. Any uncertainty in measuring the ion voltage would propagate to give uncertainty in the shunt resistance values. Therefore, it is important to know uncertainty in the measurement of the ion signal would cause how much deviation in the estimated shunt resistance value.

The uncertainty calculation is done by using Engineering Equation Solver (EES) software. Uncertainty is calculated by,

$$U_Y = \sqrt{\sum_i (\frac{dY}{dX_i})^2 U_{X_i}^2}$$

(62)

Where X_i are the measured parameters with uncertainty U_{Xi}.

Here, as only ion voltage is measured using an ion probe, assuming 10% uncertainty in measurement of ion voltage would result in 10% uncertainty of the estimated spark plug shunt resistance.

Chapter 11

11.1 Summary

A spark plug fouling tool using in-cylinder ion signal was developed. The tool outputs the ion plug fouling values against any parameter recorded in ATI. If ATI is not available and only PicoScope is used, engine speed is estimated from the ion signal. Engine speed is used to separate out cycles. Diffusion flame is also calculated using the ion curve by integrating the curve in a certain interval.

The tool can handle maximum of 8 cylinder. Ion signal from each cylinder is taken and the plug fouling for individual cylinder is measured. The tool can used as a standalone application without giving away the source code. This function of standalone analysis can be used by spark plug suppliers or anyone without access to Matlab. This tool is expected to be used by calibrators and personnel studying the parameters which affect plug fouling.

11.2 Suggestions for Future Work

Following suggestions can be taken into consideration to improve and study spark plug fouling.

- The tool can be extended to more than 8 cylinders if required. The PicoScope has 8 channels, so multiple PicoScopes can be used if required.
- To study the spark plug fouling, determine the injection timing and spark plug timing regimen for cold start and marshalling tests with least effect on spark plug fouling, best catalyst heating and least adverse drivability effects.

References

[1] "United States Environmental Protection Agency".

[2] A. Khalfan, H. Li, and G. Andrews, "Cold Start SI Passenger Car Emissions from Real World Urban Congested Traffic," 2015.

[3] Powertrain and Fluid Systems Conference and Exhibition, Ed., *Emissions measurement and testing, advanced catalysts and substrates, and diesel gaseous emissions: as part of Powertrain & Fluid Systems Conference & Exhibition, held October 25 - 28, 2004, in Tampa, Florida, USA*. Warrendale, Pa: Society of Automotive Engineers, 2004.

[4] J. D. Hawirko and M. D. Checkel, "Quantifying vehicle emission factors for various ambient conditions using an on-road, real-time emissions system," SAE Technical Paper, 2003.

[5] J. A. Eng, "The effect of spark retard on engine-out hydrocarbon emissions," SAE Technical Paper, 2005.

[6] J. F. Rodriguez and W. K. Cheng, "Reduction of Cold-Start Emissions through Valve Timing in a GDI Engine," *SAE Int. J. Engines*, vol. 9, no. 2, Apr. 2016.

[7] A. Gandhi, C. Weaver, E. Curtis, T. Alger, C. Anderson, and D. Abata, "Spary Characterization in a DISI Engine During Cold Start." SAE Technical Paper, 2006-01-1004.

[8] R. Hedinger, P. Elbert, and C. Onder, "Optimal Cold-Start Control of a Gasoline Engine," *Energies*, vol. 10, no. 10, p. 1548, Oct. 2017.

[9] "OBD II, Available Online 'http://www.obdii.com/articles/Understanding_Oxygen_Sensors.html.'" .

[10] B. T. Shaw, "Modelling and control of automotive coldstart hydrocarbon emissions," PhD Thesis, University of California, Berkeley, 2002.

[11] Kwanhee Choi, Hyungmin Lee, In Goo Hwang, Cha-Lee Myung and Simsoo Park "Effects of various intake valve timings and spark timings on combustion, cyclic THC and NOX emissions during cold start phase with idle operation in CVVT engine" Journal of Mechanical Science and Technology 22 (2008) 2254~2262.

[12] K. Cedrone and W. K. Cheng, "Using valve timing and exhaust back pressure to improve catalyst warm-up time," SAE Technical Paper, 2013.

[13] S. Lee, J. M. McGee, B. D. Quay, and D. A. Santavicca, "A comparison of fuel distribution and combustion during engine cold start for direct and port fuel injection systems," SAE Technical Paper, 1999.

[14] X. Chen, H. Fu, S. Smith, and M. Sandford, "Investigation of combustion robustness in catalyst heating operation on a spray guided DISI engine," SAE Technical Paper, 2009.

[15] Q. Fan, J. Bian, H. Lu, L. Li, and J. Deng, "Effect of the fuel injection strategy on first-cycle firing and combustion characteristics during cold start in a TSDI gasoline engine," *Int. J. Automot. Technol.*, vol. 13, no. 4, pp. 523–531, Jun. 2012.

[16] M. Costa, U. Sorge, S. Merola, A. Irimescu, M. La Villetta, and V. Rocco, "Split injection in a homogeneous stratified gasoline direct injection engine for high combustion efficiency and low pollutants emission," *Energy*, vol. 117, pp. 405–415, Dec. 2016.

[17] R. Daniel, C. Wang, H. Xu, and G. Tian, "Split-Injection Strategies under Full-Load Using DMF, A New Biofuel Candidate, Compared to Ethanol in a GDI Engine," 2012.

[18] K. Cedrone and W. K. Cheng, "SI Engine Control in the Cold-Fast-Idle Period for Low HC Emissions and Fast Catalyst Light Off," *SAE Int. J. Engines*, vol. 7, no. 2, pp. 968–976, Apr. 2014.

[19] D. I. Andrianov, F. Keynejad, R. Dingli, G. Voice, M. J. Brear, and C. Manzie, "A cold-start emissions model of an engine and aftertreatment system for optimisation studies," SAE Technical Paper, 2010.

[20] N. G. Gonzalez, R. Baar, J. Drueckhammer, and C. Kaeppner, "The Thermodynamics of Exhaust Gas Condensation," *SAE Int. J. Engines*, vol. 10, no. 2017-01–9281, pp. 1411–1421, 2017.

[21] *LabVIEW 2009 Service Pack 1, NATIONAL INSTRUMENTS.* .

[22] *"ATI Vision version 3.7.4, Accurate Technologies," 47199 Cartier Drive, Wixom, Michigan 48393, USA, Copyright 1997-2013.* .

[23] *"Combustion Analysis System", https://www.aanddtech.com/index.html.* .

[24] "J. B. Heywood, Internal Combustion Engine Fundamentals, 1988." .

130

[25] R. J. Greenshields, "Spark-Plug Fouling Studies," SAE Technical Paper, 1953.

[26] J. L. Lauer, P. J. Friel, and R. D. Miller, "Fundamental Studies Related to Spark Plug Deposits," SAE Technical Paper, 1958.

[27] B. A. Jawad and S. J. Sobolak, "Cold Temperature Effects on Spark Plug Performance," SAE Technical Paper, 1998.

[28] N. A. Henein, T. Badawy, N. Rai, and W. Bryzik, "Ion current, combustion and emission characteristics in an automotive common rail diesel engine," *J. Eng. Gas Turbines Power*, vol. 134, no. 4, p. 42801, 2012.

[29] T. Badawy, A. Shrestha, and N. Henein, "Detection of combustion resonance using an ion current sensor in diesel engines," *J. Eng. Gas Turbines Power*, vol. 134, no. 5, p. 52802, 2012.

[30] F. A. A. Estefanous, T. Badawy, and N. Henein, "Cycle Resolved In-Cylinder NOx and Ion Current Measurements in a Diesel Engine," 2013.

[31] N. A. Henein, W. Bryzik, A. Abdel-Rehim, and A. Gupta, "Characteristics of ion current signals in compression ignition and spark ignition engines," *SAE Int. J. Engines*, vol. 3, no. 2010-01–0567, pp. 260–281, 2010.

[32] Andre Saitzkoff, Raymond Reinmann, Thomas Berglind, and Magnus Glavmo, *An Ionization Equilibrium Analysis of the Spark Plug as an Ionization Sensor*. SAE Technical Paper, 1988.

[33] *"PicoScope", https://www.picotech.com/products/oscilloscope*. .

[34] "http://vigven.com/new-high-resolution-8-channel-oscilloscope-picoscope-4824/.".

[35] "https://www.accuratetechnologies.com/".

[36] Byron T. Shaw II, Gerald D. Fischer, J. Karl Hedrick, "A Simplified Coldstart Catalyst Thermal Model To Reduce Hydrocarbon Emissions" IFAC Proceedings Volumes Volume 35, Issue 1, 2002, Pages 307-312.

[37] James C. Peyton Jones, J. Brian Roberts, Pierre Bernard and Richard A. Jackson, "A Simplified Model for the Dynamics of a Three-Way Catalytic Converter," SAE Technical Paper, 2000.

[38] Vaibhav S. Kale, "Improved Startability And Reducing Emissions in Flexfuel Spark Ignition Direct Injection Variable Cam Timing Engine," PhD Dissertation, Michigan Technological University, 2014.

Appendix A. Experimental Data

A.1. E10 Fuel Properties

Workorder: 187593 MICH TECH-021413

Lab ID:	1875930001		Date Collected:	1/30/2013 00:00		Matrix: Gasoline
Sample ID:	87 PON TEST FUEL		Date Received:	1/31/2013 12:10		
Sample Desc:	FREEDOM FALL 2012		PO:			

Parameters	Qualifier	Result Units	Dilution Factor	Reporting Limit	Result Qualifier Min	Max	Analyzed	By
Vapor Pressure (VP)								
Analytical Method: ASTM D5191 [A]								
DVPE (ASTM Method)		9.62 psi	1	1.00			2/15/2013 10:43	JMP
DVPE (EPA Method)		9.73 psi	1	1.00			2/15/2013 10:43	JMP
RVPE (CARB Method)		9.53 psi	1	1.00			2/15/2013 10:43	JMP
Total VP (Ptot)		10.54 psi	1	1.00			2/15/2013 10:43	JMP
DVPE (ASTM Method)		66.3 kPa	1	1.0			2/15/2013 10:43	JMP
DVPE (EPA Method)		67.1 kPa	1	1.0			2/15/2013 10:43	JMP
RVPE (CARB Method)		65.7 kPa	1	1.0			2/15/2013 10:43	JMP
Total VP (Ptot)		72.7 kPa	1	1.0			2/15/2013 10:43	JMP
Container Size Used		1-L	1				2/15/2013 10:43	JMP
Oxygenates by GC								
Analytical Method: ASTM D4815 [A]								
tert-Amyl methyl ether (TAME)		<0.20 % m/m	1	0.20			2/15/2013 09:59	EEI
tert-Butanol (tBA)		<0.20 % m/m	1	0.20			2/15/2013 09:59	EEI
Ethanol (EtOH)		9.95 % m/m	1	0.20			2/15/2013 09:59	EEI
Methanol (MeOH)		<0.20 % m/m	1	0.20			2/15/2013 09:59	EEI
Methyl tert-butyl ether (MTBE)		<0.20 % m/m	1	0.20			2/15/2013 09:59	EEI
tert-Amyl methyl ether (TAME)		<0.20 % v/v	1	0.20			2/15/2013 09:59	EEI
tert-Butanol (tBA)		<0.20 % v/v	1	0.20			2/15/2013 09:59	EEI
Ethanol (EtOH)		9.31 % v/v	1	0.20			2/15/2013 09:59	EEI
Methanol (MeOH)		<0.20 % v/v	1	0.20			2/15/2013 09:59	EEI
Methyl tert-butyl ether (MTBE)		<0.20 % v/v	1	0.20			2/15/2013 09:59	EEI
Elemental Analysis								
Analytical Method: ASTM D5291 [A]								
Carbon (Wt%)		83.06 % m/m	1	0.05			2/15/2013 05:49	DHN
Hydrogen (Wt%)		13.48 % m/m	1	0.05			2/15/2013 05:49	DHN
Analytical Method: ASTM D4815 [A]								
Oxygen (from oxygenates)		3.46 % m/m	1	0.01			2/15/2013 15:12	AAA
Individual Parameters								
Analytical Method: ASTM D4052 [A]								
API Gravity at 15.56°C		59.0 °API	1	0.1			2/15/936 00:00	JMP

ال**نارة** للاستشارات

www.manaraa.com

Lab ID:	**1875930001**		Date Collected:	1/30/2013 00:00	Matrix: Gasoline		
Sample ID:	87 PON TEST FUEL		Date Received:	1/31/2013 12:10			
Sample Desc:	FREEDOM FALL 2012		PO:				

Parameters	Qualifier	Result Units	Dilution Factor	Reporting Limit	Result Qualifier Min	Max	Analyzed	By
Density at 15.56°C		0.7419 g/mL	1	0.0001			2/15/936 00:00	JMP
Spec. Grav. at 15.56°C/15.56°C		0.7426	1	0.0001			2/15/936 00:00	JMP
Analytical Method: ASTM D240 [A]								
Gross Heating Value (BTU/lb)		19168 BTU/lb	1	175			2/15/2013 09:45	KHR
Gross Heating Value (MJ/kg)		44.585 MJ/kg	1				2/15/2013 09:45	KHR
Net Heating Value (BTU/lb)		17938 BTU/lb	1	175			2/15/2013 09:45	KHR
Net Heating Value(MJ/kg)		41.725 MJ/kg	1				2/15/2013 09:45	KHR
Octanes								
Analytical Method: ASTM D2699 & D2700 [A]								
Research Octane Number		91.7	1	1.0			2/18/2013 12:48	AKL
Motor Octane Number		82.5	1	1.0			2/18/2013 12:48	AKL
AKI Calculation		87.1	1	1.0			2/18/2013 12:48	AKL
Sensitivity		9.2	1	1.0			2/18/2013 12:48	AKL

A.2. Split Injection Test Matrix

Table A. 1: Split Injection Test Matrix

Test#	EOI (CAD BTDC)	SOI (CAD BTDC)	SR (-)	SA (CAD ATDC)	IMEP (bar)	SD_IMEP (bar)	TurboIN (°C)	IVO	IVC	EVO	EVC
Test5	40	180	0.4	5	2.63	0.3	992.5	-349	-113	114	-352
Test6	70	180	0.4	5	2.53	0.5	1019.4	-349	-113	114	-352
Test7	20	180	0.4	15	2.66	0.4	1083.3	-349	-113	114	-352
Test8	40	180	0.4	15	2.65	0.3	1080.4	-349	-113	114	-352
Test9	70	180	0.4	15	2.59	0.4	1133.5	-349	-113	114	-352
Test10	20	180	0.7	5	2.40	0.5	966.5	-349	-113	114	-352
Test11	20	180	0.7	5	2.73	0.4	951.3	-349	-113	114	-352
Test12	40	180	0.7	5	2.44	0.5	961.8	-349	-113	114	-352
Test13	40	180	0.7	5	2.46	0.5	959.3	-349	-113	114	-352
Test14	70	180	0.7	5	2.59	0.4	964.7	-349	-113	114	-352
Test15	20	180	0.7	15	2.68	0.9	1131.9	-349	-113	114	-352
Test16	40	180	0.7	15	2.72	1.1	1158.8	-349	-113	114	-352
Test17	70	180	0.7	15	2.38	0.6	1151.6	-349	-113	114	-352
Test18	20	340	0.4	5	2.76	0.5	1005.3	-349	-113	114	-352
Test20	70	340	0.4	5	2.67	0.8	1024.6	-349	-113	114	-352
Test21	70	340	0.4	5	2.97	0.5	1017.9	-349	-113	114	-352
Test22	20	340	0.4	15	2.70	0.4	1095.4	-349	-113	114	-352
Test23	40	340	0.4	15	2.86	0.3	1093.5	-349	-113	114	-352
Test24	40	340	0.4	15	2.63	0.4	1091.3	-349	-113	114	-352
Test25	70	340	0.4	15	2.61	0.6	1141.3	-349	-113	114	-352
Test30	20	340	0.7	5	2.63	0.3	945.5	-349	-113	114	-352
Test31	40	340	0.7	5	2.66	0.2	948.1	-349	-113	114	-352
Test32	70	340	0.7	5	2.53	0.2	940.2	-349	-113	114	-352
Test33	20	340	0.7	15	2.59	0.6	1129.3	-349	-113	114	-352
Test34	40	340	0.7	15	2.49	0.5	1126.5	-349	-113	114	-352
Test35	70	340	0.7	15	2.61	0.7	1151.5	-349	-113	114	-352
Test36	20	340	0.7	5	2.66	0.3	940.2	-349	-113	114	-352
Test37	40	340	0.7	5	2.65	0.2	932.6	-349	-113	114	-352
Test39	70	340	0.7	5	2.61	0.2	933.2	-349	-113	114	-352
Test40	20	340	0.7	15	1.68	0.3	1015.3	-349	-113	114	-352
Test41	20	340	0.7	15	2.73	0.7	1154.8	-349	-113	114	-352
Test42	40	340	0.7	15	2.85	0.7	1134.4	-349	-113	114	-352

135

Test43	70	340	0.7	15	2.42	0.5	1157.3	-349	-113	114	-352

Appendix B. EES Script

The script used in EES to calculate the mixing ratio for E10 fuel for a certain lambda is given below.

```
"  Input fuel data for fuel with C, H and O"
m_C   =  83.06                    {percent kg/kg-total}
m_H   =  13.48
m_O   =  3.46

"HCR = 1.93"
"OCR = 0.03"


 lambda =1

MW_C = molarmass(C)               {kg/kgmol}
MW_H = molarmass(H)
MW_O = molarmass(O)
MW_N = molarmass(N)
MW_O2=molarmass(O2)
MW_N2 = molarmass(N2)
MW_CO=molarmass(CO)
MW_CO2=molarmass(CO2)
MW_NO=molarmass(NO)
MW_NO2=molarmass(NO2)
MW_H2=molarmass(H2)
MW_H2O=molarmass(H2O)

"  Molar Ratios for fuel "
HCR = (m_H/MW_H) / (m_C/MW_C)
OCR = (m_O/MW_O) / (m_C/MW_C)


" Reaction coefficient for C1 Fuel "
R    = 1 + HCR/4 - OCR/2

" Molecular weight of fuel of C1 Fuel "
MW_F = MW_C + MW_H*HCR + MW_O*OCR


" Chemical Equation "
" Particulate matter is not considered"
" NO is considered as its stable product N2"
```

136

www.manaraa.com

```
"! CH(HCR)O(OCR) + lambda*R*(O2 + 3.7738N2) = (a)CO2 + (b)H2O + (c)O2 + (d)N2  "


"! Equations "
" Carbon balance "

" C balance "
1 = a

" H balance "
HCR = 2*b

" O balance "
lambda*R*2 + OCR = 2*a + b  +2*c

" N balance "
lambda*R*2*3.7738 = d*2

Y_H2O = b/(a+b+d+c)

X_H2O = b*MW_H2O/(a*MW_CO2+c*MW_O2 + d*MW_N2)

"X_H2O = 0.1"

 M_H2O = b*MW_H2O

"AFR calculations "
AFR = lambda*(R*4.778*28.97) / MW_F

MF = MW_H2O*lambda*R/(0.965*28.9)
```

Appendix C. Calculated Data

C.1.   Combustion Parameter Matrix Calculated using Method 1

The combustion parameters calculated using Method A which is by using only PolyC values is given in the table below.

Table C. 1: Combustion Parameters Matrix calculated using Method A

Test#	CA50 (CAD BTDC)	CA10 (CAD BTDC)	CA90 (CAD BTDC)	CA1090 (CAD)	CA0010 (CAD)	SD CA0010 (CAD)	SD CA1090 (CAD)	SD CA10 (CAD)	SD CA50 (CAD)	SD CA90 (CAD)
Test5	57.4	33.3	94.3	61.0	28.4	3.8	3.8	3.8	6.2	6.3
Test6	72.0	40.3	115.8	76.5	35.3	6.4	7.3	6.4	11.2	6.7
Test7	71.3	47.0	109.8	63.0	32.0	5.1	6.6	5.1	7.4	6.4
Test8	75.0	47.8	114.1	66.4	32.9	3.6	6.2	3.6	5.5	5.9
Test9	84.7	53.8	122.5	69.1	38.9	4.3	6.5	4.3	6.6	4.7
Test10	70.1	41.9	109.9	68.8	37.0	6.7	6.4	6.7	11.4	6.9
Test11	63.8	38.7	109.5	71.1	33.8	5.5	7.8	5.5	9.7	9.1
Test12	73.3	43.3	112.7	70.9	38.4	8.7	6.9	8.7	13.5	6.9
Test13	71.8	42.1	111.9	70.9	37.2	7.4	7.0	7.4	12.6	7.1
Test14	74.0	42.9	120.6	78.1	37.9	5.5	5.7	5.5	9.5	4.3
Test15	85.0	58.4	111.8	58.3	43.5	13.6	5.9	13.6	16.5	5.4
Test16	90.8	63.7	119.1	62.2	48.7	15.4	8.6	15.3	16.9	5.1
Test17	94.4	60.3	123.4	65.3	45.4	8.3	6.3	8.3	11.8	3.7
Test18	58.1	35.2	93.8	59.7	30.3	9.0	3.6	9.0	11.5	7.8
Test20	76.7	46.5	118.6	76.6	41.6	16.6	8.2	16.6	17.2	5.4
Test21	65.6	38.1	118.1	80.6	33.2	6.7	6.9	6.7	10.0	5.5
Test22	72.8	48.0	108.0	60.2	33.1	6.0	5.0	6.0	7.8	5.5
Test23	73.1	46.8	113.2	66.5	31.9	3.4	6.7	3.4	5.4	6.3
Test24	77.7	49.9	113.9	64.0	35.0	4.3	6.3	4.3	6.6	6.0
Test25	87.4	57.4	124.6	69.1	42.5	7.5	6.7	7.5	11.1	3.9
Test30	62.1	38.1	101.3	63.3	33.1	4.7	8.5	4.7	6.3	10.9
Test31	60.7	36.5	101.1	64.5	31.6	3.0	8.3	3.0	4.8	10.1
Test32	62.3	36.9	111.7	74.7	32.0	2.9	7.1	2.9	4.8	7.8
Test33	80.7	53.3	117.2	65.6	38.4	9.7	7.6	9.7	11.5	5.7

138

Test34	83.0	54.4	119.7	66.2	39.4	6.7	7.3	6.7	9.4	5.0
Test35	87.9	58.6	121.3	65.5	43.6	9.6	7.4	9.6	12.3	5.1
Test36	61.5	36.7	105.1	68.4	31.8	3.6	9.3	3.6	6.0	11.0
Test37	62.4	36.0	106.1	70.1	31.0	2.8	9.2	2.8	5.1	10.6
Test39	63.9	36.9	114.8	77.9	31.9	2.8	5.6	2.8	4.8	6.6
Test40	89.2	56.9	118.6	62.1	41.9	4.3	4.6	4.4	7.0	3.7
Test41	84.8	57.5	113.8	58.9	42.6	10.6	6.8	10.6	13.0	5.4
Test42	85.5	56.7	116.9	62.6	41.8	9.9	7.9	9.9	12.7	5.0
Test43	92.9	60.6	123.6	63.8	45.6	5.6	6.4	5.6	8.5	3.7

C.2. Combustion Parameter Matrix Calculated using Method 2

The combustion parameters calculated using Method 2 which is by changing the crank angle interval for PolyE values calculation is given in the table below.

Table C. 2: Combustion Parameters Matrix calculated using Method A

Test#	CA50 (CAD BTDC)	CA10 (CAD BTDC)	CA90 (CAD BTDC)	CA1090 (CAD)	CA0010 (CAD)	SD CA0010 (CAD)	SD CA1090 (CAD)	SD CA10 (CAD)	SD CA50 (CAD)	SD CA90 (CAD)
Test5	57.4	33.3	94.9	61.7	28.4	3.7	4.4	3.7	6.4	6.1
Test6	72.1	40.1	113.1	74.3	35.1	6.6	7.2	6.6	12.0	6.6
Test7	71.3	47.0	109.2	62.5	32.1	5.2	6.6	5.2	7.6	6.1
Test8	75.0	47.9	113.8	66.2	32.9	3.6	6.2	3.6	5.6	5.8
Test9	84.6	53.7	120.9	67.8	38.7	4.4	6.3	4.4	6.8	4.7
Test10	70.3	41.7	108.7	67.9	36.8	6.7	6.0	6.7	11.8	6.6
Test11	63.7	38.6	108.4	70.2	33.7	5.5	7.7	5.6	9.6	8.4
Test12	73.5	43.2	111.9	70.5	38.3	8.7	6.9	8.7	14.1	6.5
Test13	71.9	42.1	111.2	70.6	37.2	7.6	7.1	7.6	13.0	6.7
Test14	74.0	42.6	119.2	77.1	37.7	5.5	6.2	5.5	9.9	4.8
Test15	85.1	58.4	111.4	58.2	43.5	13.6	5.6	13.6	16.6	5.3
Test16	90.9	63.7	118.8	62.0	48.8	15.5	8.4	15.5	17.4	5.0
Test17	94.4	60.1	122.6	65.0	45.1	8.3	6.0	8.3	12.1	3.7
Test18	58.3	35.3	93.5	59.6	30.4	9.3	3.9	9.3	12.5	7.3
Test20	76.5	45.9	115.7	74.5	41.0	16.5	8.3	16.5	17.4	6.3

139

Test21	65.7	37.9	116.2	79.2	33.0	6.9	7.7	6.9	10.8	6.3
Test22	72.8	47.9	107.5	60.0	33.0	6.1	4.8	6.1	8.0	5.2
Test23	73.1	46.7	113.3	66.6	31.8	3.4	6.8	3.4	5.4	6.3
Test24	77.7	49.8	113.6	63.9	34.8	4.3	6.3	4.3	6.7	6.0
Test25	87.4	57.1	123.3	68.2	42.2	7.5	6.7	7.5	11.4	4.2
Test30	62.0	38.0	100.5	62.6	33.0	4.5	8.0	4.5	6.2	9.3
Test31	60.7	36.6	103.3	66.7	31.6	2.9	8.5	2.9	4.7	9.1
Test32	62.3	36.9	111.8	74.9	31.9	2.8	7.4	2.8	4.8	7.5
Test33	80.8	53.3	116.6	65.4	38.4	9.9	7.5	9.9	12.0	5.6
Test34	83.1	54.4	119.4	66.1	39.4	6.7	7.3	6.7	9.7	5.0
Test35	87.9	58.4	120.7	65.1	43.5	9.7	7.2	9.7	12.5	5.1
Test36	61.5	36.7	104.1	67.5	31.7	3.5	9.2	3.5	6.0	10.2
Test37	62.4	36.0	107.1	71.1	31.0	2.7	9.1	2.7	5.1	9.9
Test39	63.8	36.8	113.6	76.9	31.8	2.7	6.4	2.7	4.8	7.0
Test40	89.2	56.6	117.8	61.7	41.6	4.4	4.2	4.4	7.2	3.5
Test41	84.9	57.4	113.2	58.6	42.4	10.7	6.4	10.7	13.4	5.3
Test42	85.8	56.8	116.5	62.6	41.8	10.1	7.8	10.1	13.3	5.1
Test43	92.8	60.2	122.8	63.4	45.3	5.6	6.1	5.6	8.7	3.7

Appendix D. Look-Up Tables

Table D. 1: Calibration Table for Exhaust Manifold Thermal Model

$T_{m\_manifold}$ [K]	270	290	307	500
$H_{gs\_manifold}.A_{i\_manifold}$ [W/(m.K)x(m^2)]	10.5	10.5	6.5	6.55

Table D. 2: Calibration Table for Turbocharger Thermal Model

T_{m_turbo} [K]	290	300	302	308	312	315
$H_{gs\_turbo}.A_{i\_manifold}$ [W/(m.K)x(m^2)]	10	5.4	4.8	3.6	2.5	2.5

Table D. 3: Calibration Table for Catalyst Thermal Model

T_{m_cat} [K]	200	350	700
$H_{gs\_cat}.A_{i\_cat}$ [W/(m.K)x(m^2)]	50	50	0

Appendix E. Letter of Permission

Letter of Permission

Yash Borghate <yvborgha@mtu.edu>   Wed, Apr 11, 2018 at 7:04 PM
To: jfrb@mit.edu, wkcheng@mit.edu

Hello Felipe and Dr. Cheng,

I'm a master's student at Michigan Tech doing my research in Cold start of a gasoline engine under the guidance of Dr. Naber. I would like to use a figure from your research paper for my thesis dissertation.

"Reduction of Cold-Start Emissions through Valve Timing in a GDI Engine," SAE Int. J. Engines, vol. 9, no. 2, Apr. 2016.

Figure 1. Cumulative tailpipe HC and PM/PN emissions over the FTP-75
cycle for GDI engines.

I would like to seek permission for the same.

Thank You,
Yash Borghate

Letter of Permission

Wai K Cheng <wkcheng@mit.edu>   Thu, Apr 12, 2018 at 1:20 PM
To: Yash Borghate <yvborgha@mtu.edu>, Felipe Rodriguez <jfrb@mit.edu>

Dear Yash,

You could go ahead and use the figure in your thesis. However, if you want to use it in a commercial publication such as a book, you have to clear with SAE because they own the copyright of the papers.

Wai

142